

Hybrid Simulation Theory Featuring Bars and Beams

by

Paul Luke Drazin

B.S. (University of California, Berkeley) 2012

A report submitted in partial satisfaction of the  
requirements for the degree of

Masters of Science, Plan II

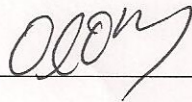
in

Mechanical Engineering

at the

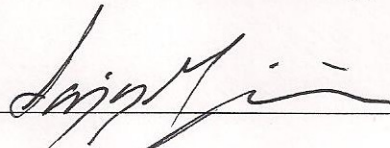
University of California at Berkeley

Committee in charge:



---

Professor Oliver O'Reilly, Co-chair

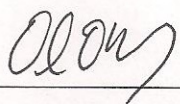
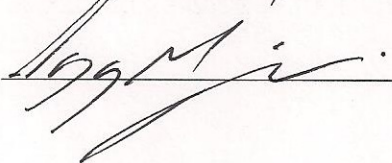


---

Professor Sanjay Govindjee, Co-chair

Fall 2013

The report of Paul Luke Drazin, titled Hybrid Simulation Theory Featuring Bars and Beams, is approved:

Co-chair  Date October 7, 2013  
Co-chair  Date Oct. 4, 2013

University of California, Berkeley

# Hybrid Simulation Theory Featuring Bars and Beams

Copyright © 2013  
by  
Paul Luke Drazin

## Abstract

Hybrid Simulation Theory Featuring Bars and Beams

by

Paul Luke Drazin

Masters of Science, Plan II in Mechanical Engineering

University of California, Berkeley

Professor Oliver O'Reilly, Co-chair

Professor Sanjay Govindjee, Co-chair

Hybrid Simulation is a simulation technique involving the integration of a physical system and a computational system with the use of actuators and sensors. This method has a strong background in the experimental community and has been used for many years. However, there is a noticeable lack of theoretical research on the performance of hybrid simulation. The hybrid simulation experiments are performed with the assumption of an accurate result as long as the main causes of error are reduced. However, the theoretical background on hybrid testing needs to be developed in order to validate these experimental findings.

In this report, four systems are independently studied for a theoretical analysis of the performance of hybrid simulation: an elastic bar, an elastic beam, a viscoelastic bar, and a viscoelastic beam. Each of these systems has a well-known analytical solution, making each an ideal candidate to compare with a theoretical hybrid simulation experiment. Each model is separated into two substructures: a computational substructure and a physical substructure. At the new imposed interface, errors are introduced, simulating errors that would naturally occur in an experimental setup. A parametric study of these imposed errors is performed, where  $L_2$  norms are used for determining the error between the actual system and the hybrid system. It is found that resonant frequencies of the system have a large effect on the error in all cases, except near regions of damping in the viscoelastic systems. Thus, if the exciting loads act at a resonant frequency, the results obtained from hybrid simulation may vary greatly from those of the real system. However, there are other sources of error that come from how the hybrid system was constructed because each of the substructures can be excited in ways different than that of the whole system. Finally, it is noted that error in the system grows quickly with increasing interface matching error but the system error becomes insensitive to further increases in mismatch error.

This report is dedicated to my parents, family, and friends who always encouraged me to do my best and chase my dreams.

# Contents

<b>Contents</b>	<b>ii</b>
<b>List of Figures</b>	<b>iv</b>
<b>List of Notations</b>	<b>viii</b>
<b>List of Tables</b>	<b>x</b>
<b>1 Introduction</b>	<b>1</b>
1.1 Background on Hybrid Simulation . . . . .	1
1.2 General Theory of Hybrid Simulation . . . . .	2
1.2.1 The Reference System . . . . .	2
1.2.2 The Hybrid System . . . . .	3
1.3 Hybrid Simulation Error . . . . .	4
1.4 Organization of this Report . . . . .	5
<b>2 Hybrid Simulation Theory Applied to the Elastic Bar and Beam</b>	<b>6</b>
2.1 Application to the Elastic Bar . . . . .	6
2.1.1 Reference System . . . . .	6
2.1.2 Hybrid System . . . . .	7
2.1.3 Non-Dimensionalization and Determination of $g_k$ . . . . .	9
2.2 Application to the Elastic Beam . . . . .	10
2.2.1 Reference System . . . . .	10
2.2.2 Hybrid System . . . . .	12
2.2.3 Non-Dimensionalization and Determination of $g_k$ . . . . .	14
<b>3 Hybrid Simulation Theory Applied to the Viscoelastic Bar and Beam</b>	<b>17</b>
3.1 Application to the Viscoelastic Bar . . . . .	17
3.2 Application to the Viscoelastic Beam . . . . .	19
<b>4 Analysis of Hybrid Simulation Theory for the Elastic and Viscoelastic Models</b>	<b>22</b>
4.1 Analysis of the Elastic Model . . . . .	22

4.1.1	Elastic Bar . . . . .	22
4.1.2	Elastic Beam . . . . .	31
4.2	Analysis of the Viscoelastic Model . . . . .	40
4.2.1	Viscoelastic Bar . . . . .	40
4.2.2	Viscoelastic Beam . . . . .	48
<b>5</b>	<b>Conclusion</b>	<b>58</b>
5.1	Summary of Results . . . . .	58
5.2	Potential Future Research in the Field of Hybrid Simulation Theory . . . . .	59
	<b>Bibliography</b>	<b>60</b>
<b>A</b>	<b>Analytical Bar Error Equation Derivation</b>	<b>62</b>
<b>B</b>	<b>Analytical Solutions vs. Computational Solutions</b>	<b>65</b>
<b>C</b>	<b>Material Constants</b>	<b>69</b>
C.1	Fixed-Free Bar . . . . .	69
C.2	Pinned-Pinned Beam . . . . .	69

# List of Figures

1.1	A general system with domain $\mathcal{D}$ and displacement $\mathbf{u}(\mathbf{x}, t)$ . . . . .	2
1.2	A general system with imposed separation into two substructures for comparison to the hybrid system. $\mathcal{P} \cup \mathcal{C} = \mathcal{D}$ and $\mathcal{P} \cap \mathcal{C} = \emptyset$ . . . . .	3
1.3	The hybrid system separated into the physical, $\mathcal{P}$ , and computational, $\mathcal{C}$ , substructures with gap function $g_k$ . . . . .	4
2.1	The system of an elastic fixed-free bar with applied forcing, $f(t)$ . . . . .	6
2.2	The system of an elastic fixed-free bar with applied forcing, $f(t)$ , with hybrid separation and gap functions $g_1(t)$ and $g_2(t)$ , $l_1 + l_2 = l$ . . . . .	8
2.3	The system of an elastic pinned-pinned beam with applied moment, $M(t)$ . . . . .	11
2.4	The system of an elastic pinned-pinned beam with applied moment, $M(t)$ , with hybrid separation and gap functions $g_1(t)$ , $g_2(t)$ , $g_3(t)$ , and $g_4(t)$ , $l_1 + l_2 = l$ . . . . .	12
4.1	Comparison of the reference elastic fixed-free bar to the hybrid elastic fixed-free bar with no imposed error. . . . .	23
4.2	Comparison of the reference elastic fixed-free bar to the hybrid elastic fixed-free bar with $\epsilon_1 = 0.1$ . . . . .	24
4.3	(a) A frequency sweep of the elastic fixed-free bar with $\epsilon_1 = 0.1$ on a log-log plot. (b) A zoomed in plot showing the mini peak . . . . .	26
4.4	A frequency sweep of the elastic fixed-free bar with $\epsilon_2 = 0.1$ on a log-log plot. . . . .	26
4.5	A frequency sweep of the elastic fixed-free bar with $d_1 = 0.1$ on a log-log plot. . . . .	27
4.6	A frequency sweep of the elastic fixed-free bar with $d_2 = 0.1$ on a log-log plot. . . . .	27
4.7	(a) A frequency sweep of the elastic fixed-free bar with $\epsilon_1 = 0.1$ and $\epsilon_2 = 0.1$ on a log-log plot. (b) A zoomed in plot missing the mini peak . . . . .	28
4.8	A frequency sweep of the elastic fixed-free bar with $\epsilon_1 = 0.1$ and $d_1 = 0.1$ on a log-log plot. . . . .	28
4.9	A frequency sweep of the elastic fixed-free bar with $\epsilon_1 = 0.1$ and $d_2 = 0.1$ on a log-log plot. . . . .	29
4.10	A frequency sweep of the elastic fixed-free bar with $d_1 = 0.1$ and $d_2 = 0.1$ on a log-log plot. . . . .	29
4.11	The error in the $\epsilon_1$ domain of the elastic fixed-free bar with no other imposed error for multiple frequencies on a linear-log plot. . . . .	30

4.12	The error in the $d_1$ domain of the elastic fixed-free bar with no other imposed error for multiple frequencies on a log-log plot. . . . .	31
4.13	Comparison of the reference elastic pinned-pinned beam to the hybrid elastic pinned-pinned beam with no imposed error. . . . .	32
4.14	Comparison of the reference elastic pinned-pinned beam to the hybrid elastic pinned-pinned beam with $\epsilon_1 = 0.1$ . . . . .	32
4.15	(a) A frequency sweep of the elastic pinned-pinned beam with $\epsilon_1 = 0.1$ on a log-log plot. (b) A zoomed in plot showing the mini peak. . . . .	34
4.16	A frequency sweep of the elastic pinned-pinned beam with $\epsilon_3 = 0.1$ on a log-log plot. . . . .	35
4.17	A frequency sweep of the elastic pinned-pinned beam with $d_1 = 0.1$ on a log-log plot. . . . .	35
4.18	A frequency sweep of the elastic pinned-pinned beam with $d_3 = 0.1$ on a log-log plot. . . . .	36
4.19	(a) A frequency sweep of the elastic pinned-pinned beam with $\epsilon_1 = 0.1$ and $\epsilon_3 = 0.1$ on a log-log plot. (b) A zoomed in plot missing the mini peak. . . . .	36
4.20	A frequency sweep of the elastic pinned-pinned beam with $\epsilon_1 = 0.1$ and $d_1 = 0.1$ on a log-log plot. . . . .	37
4.21	A frequency sweep of the elastic pinned-pinned beam with $\epsilon_1 = 0.1$ and $d_3 = 0.1$ on a log-log plot. . . . .	37
4.22	A frequency sweep of the elastic pinned-pinned beam with $d_1 = 0.1$ and $d_3 = 0.1$ on a log-log plot. . . . .	38
4.23	The error in the $\epsilon_1$ domain of the elastic pinned-pinned beam with no other imposed error for multiple frequencies on a linear-log plot. . . . .	38
4.24	The error in the $d_1$ domain of the elastic pinned-pinned beam with no other imposed error for multiple frequencies on a log-log plot. . . . .	39
4.25	Comparison of the reference viscoelastic fixed-free bar to the hybrid viscoelastic fixed-free bar with no imposed error. . . . .	40
4.26	Comparison of the reference viscoelastic fixed-free bar to the hybrid viscoelastic fixed-free bar with $\epsilon_1 = 0.1$ . . . . .	41
4.27	(a) A frequency sweep of the viscoelastic fixed-free bar with $\epsilon_1 = 0.1$ on a log-log plot. (b) A zoomed in plot . . . . .	42
4.28	A frequency sweep of the viscoelastic fixed-free bar with $\epsilon_2 = 0.1$ on a log-log plot.	43
4.29	A frequency sweep of the viscoelastic fixed-free bar with $d_1 = 0.1$ on a log-log plot.	43
4.30	A frequency sweep of the viscoelastic fixed-free bar with $d_2 = 0.1$ on a log-log plot.	44
4.31	(a) A frequency sweep of the viscoelastic fixed-free bar with $\epsilon_1 = 0.1$ and $\epsilon_2 = 0.1$ on a log-log plot. (b) A zoomed in plot . . . . .	44
4.32	A frequency sweep of the viscoelastic fixed-free bar with $\epsilon_1 = 0.1$ and $d_1 = 0.1$ on a log-log plot. . . . .	45
4.33	A frequency sweep of the viscoelastic fixed-free bar with $\epsilon_1 = 0.1$ and $d_2 = 0.1$ on a log-log plot. . . . .	45

4.34	A frequency sweep of the viscoelastic fixed-free bar with $d_1 = 0.1$ and $d_2 = 0.1$ on a log-log plot. . . . .	46
4.35	The error in the $\epsilon_1$ domain of the viscoelastic fixed-free bar with $\Omega = 74.1$ on a linear-log plot for multiple $\zeta$ values. . . . .	47
4.36	The error in the $d_1$ domain of the viscoelastic fixed-free bar with $\Omega = 74.1$ on a log-log plot for multiple $\zeta$ values. . . . .	48
4.37	Comparison of the reference viscoelastic pinned-pinned beam to the hybrid viscoelastic pinned-pinned beam with no imposed error. . . . .	49
4.38	Comparison of the reference viscoelastic pinned-pinned beam to the hybrid viscoelastic pinned-pinned beam with $\epsilon_1 = 0.1$ . . . . .	49
4.39	(a) A frequency sweep of the viscoelastic pinned-pinned beam with $\epsilon_1 = 0.1$ on a log-log plot for multiple $\zeta$ values. (b) A zoomed in plot showing the mini peak. . . . .	51
4.40	A frequency sweep of the viscoelastic pinned-pinned beam with $\epsilon_3 = 0.1$ on a log-log plot for multiple $\zeta$ values. . . . .	52
4.41	A frequency sweep of the viscoelastic pinned-pinned beam with $d_1 = 0.1$ on a log-log plot for multiple $\zeta$ values. . . . .	52
4.42	A frequency sweep of the viscoelastic pinned-pinned beam with $d_3 = 0.1$ on a log-log plot for multiple $\zeta$ values. . . . .	53
4.43	(a) A frequency sweep of the viscoelastic pinned-pinned beam with $\epsilon_1 = 0.1$ and $\epsilon_3 = 0.1$ on a log-log plot for multiple $\zeta$ values. (b) A zoomed in plot showing the mini peak. . . . .	53
4.44	A frequency sweep of the viscoelastic pinned-pinned beam with $\epsilon_1 = 0.1$ and $d_1 = 0.1$ on a log-log plot for multiple $\zeta$ values. . . . .	54
4.45	A frequency sweep of the viscoelastic pinned-pinned beam with $\epsilon_1 = 0.1$ and $d_3 = 0.1$ on a log-log plot for multiple $\zeta$ values. . . . .	54
4.46	A frequency sweep of the viscoelastic pinned-pinned beam with $d_1 = 0.1$ and $d_3 = 0.1$ on a log-log plot for multiple $\zeta$ values. . . . .	55
4.47	The error in the $\epsilon_1$ domain of the viscoelastic pinned-pinned beam with $\Omega = 79.1$ on a linear-log plot for multiple $\zeta$ values. . . . .	56
4.48	The error in the $d_1$ domain of the viscoelastic pinned-pinned beam with $\Omega = 79.1$ on a log-log plot for multiple $\zeta$ values. . . . .	57
B.1	A comparison of the analytical and numerical solutions to the elastic fixed-free bar with $\epsilon_1 = 0.1$ on a log-log plot. . . . .	66
B.2	A comparison of the analytical and numerical solutions to the elastic fixed-free bar with $d_1 = 0.1$ on a log-log plot. . . . .	66
B.3	A comparison of the analytical and numerical solutions to the elastic fixed-free bar with $\epsilon_1 = 0.1$ and $d_1 = 0.1$ on a log-log plot. . . . .	67
B.4	The absolute value of the difference between the analytical and numerical solutions to the elastic fixed-free bar with $\epsilon_1 = 0.1$ on a log-log plot. . . . .	67
B.5	The absolute value of the difference between the analytical and numerical solutions to the elastic fixed-free bar with $d_1 = 0.1$ on a log-log plot. . . . .	68

B.6	The absolute value of the difference between the analytical and numerical solutions to the elastic fixed-free bar with $\epsilon_1 = 0.1$ and $d_1 = 0.1$ on a log-log plot. . .	68
-----	--	----

# List of Notations

$\bar{\omega}$	Lowest resonant frequency of the elastic system
$\bar{f}$	Magnitude of the applied harmonic force in the bar system
$\bar{M}$	Magnitude of applied harmonic bending moment in the beam system
$\beta$	Wavenumber of the solution
$\epsilon_k$	Magnitude error for the $k^{th}$ gap function (Error Parameter)
$\eta$	Non-dimensional vertical displacement ( $w$ )
$\hat{\square}$	Quantity for the hybrid system
$\kappa$	Non-Dimensional Wavenumber of the solution
$\mathbf{u}$	Displacement vector of system
$\mathbf{x}$	Position vector of system
$\mathcal{C}$	Domain of the computational substructure of the system
$\mathcal{D}$	Complete domain of the system
$\mathcal{P}$	Domain of the physical substructure of the system
$\mu$	Non-dimensional applied bending moment
$\Omega$	Non-dimensional applied frequency
$\omega$	Applied frequency of harmonic excitation
$\ e\ $	$L_2$ Norm of the difference in displacement
$\rho$	Linear mass density of the system
$\square_c$	Quantity in the $\mathcal{C}$ domain (Computational substructure)
$\square_p$	Quantity in the $\mathcal{P}$ domain (Physical substructure)

$\square_{,x}$	Represents the partial derivative with respect to $x$ ( $\frac{\partial \square}{\partial x}$ )
$\tau$	Non-dimensional time
$\xi$	Non-dimensional horizontal displacement ( $u$ )
$\zeta$	Non-Dimensional damping frequency for the viscoelastic systems
$A$	Area of the bar
$d_k$	Time delay (phase error) for the $k^{th}$ gap function (Error Parameter)
$E$	Elastic (Young's) modulus
$E'$	Storage modulus
$E''$	Loss modulus
$E^*$	Complex elastic modulus
$F$	Non-dimensional applied force
$G_k$	Non-dimensional gap function
$g_k$	Gap function
$I$	Second moment of area of the beam
$i$	Imaginary unit ( $\sqrt{-1}$ )
$l$	Length of the bar or beam
$L_1$	Non-Dimensional length of the physical substructure
$l_1$	Length of the physical substructure
$L_2$	Non-Dimensional length of the computational substructure
$l_2$	Length of the computational substructure
$t$	Time
$u$	Horizontal Displacement
$w$	Vertical Displacement
$x$	Coordinate along bar and beam
$y$	Non-dimensional coordinate along the system ( $x$ )

# List of Tables

C.1	Material constants and dimensions used for fixed-free bar systems . . . . .	69
C.2	Material constants and dimensions used for fixed-free bar systems . . . . .	69

## Acknowledgments

The project is made possible by the financial support of the National Science Foundation for the project “EAGER: Next Generation Hybrid Simulation - Evaluation and Theory” (Award Number: CMMI-1153665).

I would like to thank my co-advisors Professor Oliver O’Reilly and Professor Sanjay Govindjee for giving me the opportunity to work on this project, all the while guiding me with their invaluable support and insight, which was necessary for the completion of this report. Thanks to Professor Khalid Mosalam who lead the research team when I was first starting on this project. Thanks to Ahmed Bakhaty, who’s work kept me going and helped develop and refine the information in this report. I would like to recognize Alex Fung and Robert Tang-Kong for taking the time to read and critique this report. And thanks to the Govindjee group, all of the UC Berkeley faculty and staff, and my friends and classmates who have made my years at UC Berkeley some of the best years of my life.

# Chapter 1

## Introduction

### 1.1 Background on Hybrid Simulation

Hybrid Simulation is the method in which part of a system is modeled physically and the part of the system is modeled computationally [15]. The two parts are then connected with the use of actuators and sensors. This allows for only part of the system to be built in order for the whole system to be simulated. This is useful for systems that are typically too large or expensive to be tested. Hybrid Simulation may be categorized into two main types: real-time hybrid simulation and pseudodynamic hybrid simulation [16]. The former uses laboratory setups to drive the experiment in a real-time setting, typically with the use of a shake table and other actuators, which provides dynamic response. The latter uses a step-by-step numerical solution where the system is quasi-static and the mass characteristics of the system are modeled numerically. Hybrid simulation has mainly been used as a testing method in structural mechanics, especially for earthquake response testing [15, 19]. However, other types of experiments have also been done [3], which shows that hybrid simulation also has some possible use in fields other than structural mechanics, such as the automotive industry, ship building industry, and other fields where it is impractical to build a complete physical system to do testing.

Real-time hybrid simulation requires the equations of motion of the system, either of discrete objects or a continua, to be determined [16]. Once the equations of motion have been determined, the system is separated into multiple substructures, some of which are physical substructures and the rest are computational substructures [7]. The physical substructure will be placed in a lab and connected to sensors and actuators. The computational substructures can be solved using different numerical methods, including Newmark methods and finite elements [4, 16]. However, the physical and computational substructures are interacting with each other via the sensors and actuators. The sensors provide information to the computational substructures regarding the current state of the physical substructures and the actuators manipulate the physical substructures based on the current state of the computational substructure. This process is run in real-time to simulate the desired system.

However, most of the work with hybrid simulation so far has been purely experimental, which means that there is very little theoretical background to verify the results that these experiments produce. There has been some study of the errors associated with hybrid simulation, but in many of those situations, the errors studied were due to the entire experimental setup and numerical integration, rather than the errors associated with a hybrid system [17, 18]. This report focuses solely on the theoretical performance of real-time hybrid simulation as an experimental method. This approach avoids the errors associated with solving the system using numerical methods and focuses on the errors that are created by splitting the system into a hybrid system. In order to test hybrid simulation theoretically, the use of the following theoretical models are employed: a harmonic axial load on a bar and a harmonic flexing moment on a beam. Both of these models have been chosen for their relative simplicity and the ability to analyze the solutions to these systems in analytical forms. This leads to the best possible performance specification for hybrid simulation on simple models that can then be extended to more complex systems. For completeness, elastic and viscoelastic material models are studied for both the bar and beam.

## 1.2 General Theory of Hybrid Simulation

### 1.2.1 The Reference System

First, the complete theoretical system is determined, with domain  $\mathcal{D}$  as seen in Fig. 1.1. In this section, the system in question is kept as general as possible to allow for possible

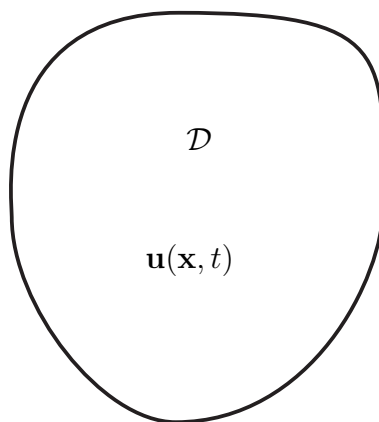


Figure 1.1: A general system with domain  $\mathcal{D}$  and displacement  $\mathbf{u}(\mathbf{x}, t)$ .

expansion to other systems other than bars and beams, which are the focus of this report. In most cases, the displacement and its spatial derivatives are the most useful and easiest quantities to measure since they all have physical meaning, such as rotation, force, moment, and shear [11]. Therefore, the displacement of the system is the physical quantity that is

studied in this report. The displacement of the system is defined by

$$\mathbf{u}(\mathbf{x}, t) \text{ for } \mathbf{x} \in \mathcal{D}. \quad (1.1)$$

The system is then separated into two or more substructures to emulate the hybrid simulation procedure. This report focuses only on two substructures for the hybrid system, a “physical” substructure ( $\mathcal{P}$ -side) and a “computational” substructure ( $\mathcal{C}$ -side) as shown in Fig. 1.2, where  $\mathcal{P} \cup \mathcal{C} = \mathcal{D}$  and  $\mathcal{P} \cap \mathcal{C} = \emptyset$ . This allows for the displacement to also be separated into two

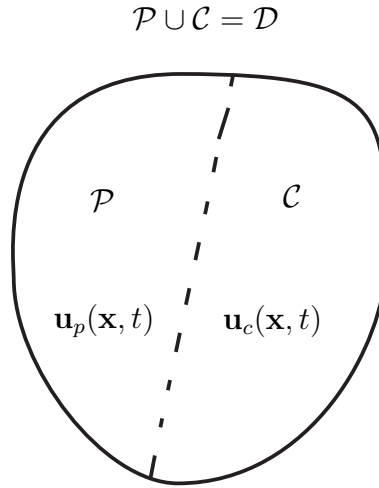


Figure 1.2: A general system with imposed separation into two substructures for comparison to the hybrid system.  $\mathcal{P} \cup \mathcal{C} = \mathcal{D}$  and  $\mathcal{P} \cap \mathcal{C} = \emptyset$ .

pieces, as indicated by

$$\mathbf{u}(\mathbf{x}, t) = \begin{cases} \mathbf{u}_p(\mathbf{x}, t) & \text{if } \mathbf{x} \in \mathcal{P} \\ \mathbf{u}_c(\mathbf{x}, t) & \text{if } \mathbf{x} \in \mathcal{C}. \end{cases} \quad (1.2)$$

This system represents the real solution, against which the hybrid systems are compared.

## 1.2.2 The Hybrid System

Now that the reference system has been defined, the hybrid system needs to be defined. Using the same boundary defined in Fig. 1.2, the hybrid system is separated into two substructures. In order to differentiate the reference system from the hybrid system a hat ( $\hat{\cdot}$ ) is used to indicate a quantity in the hybrid system. Thus, the displacement for the hybrid system is given by

$$\hat{\mathbf{u}}(\mathbf{x}, t) = \begin{cases} \hat{\mathbf{u}}_p(\mathbf{x}, t) & \text{if } \mathbf{x} \in \mathcal{P} \\ \hat{\mathbf{u}}_c(\mathbf{x}, t) & \text{if } \mathbf{x} \in \mathcal{C}. \end{cases} \quad (1.3)$$

However, since the system is now physically separated into two pieces, functions are created in order for the two substructures to interact, emulating the use of sensors and actuators in a lab. For this, gap functions, designated as  $g_k$ , are defined as shown in Fig. 1.3. The gap

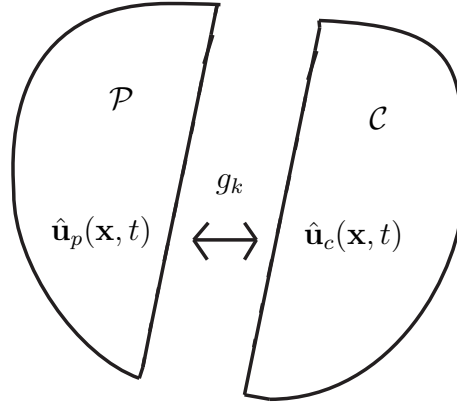


Figure 1.3: The hybrid system separated into the physical,  $\mathcal{P}$ , and computational,  $\mathcal{C}$ , substructures with gap function  $g_k$ .

functions act as boundary conditions for the newly created boundary between the  $\mathcal{P}$ -side and the  $\mathcal{C}$ -side of the system. The number of gap functions needed is determined by the hybrid system so that the system is mathematically determinate. Since these gap functions take on the role of boundary conditions, for every gap function on the  $\mathcal{P}$ -side, there is a corresponding gap function on the  $\mathcal{C}$ -side. To create a convention with regards to  $g_k$ , when  $k$  is an odd number, the gap function relates to the  $\mathcal{P}$ -side, and the following even  $k$  is the corresponding  $\mathcal{C}$ -side gap function. Thus, the pairs of gap functions are  $k = 1, 2$ ,  $k = 3, 4$ , and so forth. The gap functions take into consideration the imperfection of the dynamics of the hybrid system, such as time-delay between the two sides, as well as magnitude tracking errors in the displacement, rotation, force, moment, and shear as needed by the system at hand. This allows us to see the effects of these imperfections on the solution that the hybrid simulation produces. These types of errors are chosen due to their direct correlation to experimental systems [1, 18].

### 1.3 Hybrid Simulation Error

Now that both the reference system and the hybrid system have both been defined, an error analysis of the solutions is implemented to assess the theoretical effectiveness of hybrid simulation. In order to perform the error analysis an  $L_2$  Norm is employed, given by [12]

$$\|e\| = \left( \int_0^T \int_{\mathcal{D}} (\mathbf{u}(\mathbf{x}, t) - \hat{\mathbf{u}}(\mathbf{x}, t))^2 dxdt \right)^{1/2}, \quad (1.4)$$

where  $T$  is the period of the harmonic loading on the system and  $\mathcal{D}$  is the complete domain of the system. This allows for a measurement of the absolute error between the reference system and the hybrid system over the domain of the mechanical system and over the period of harmonic loading. An analysis of these errors can be done by varying multiple parameters including the forcing frequency, the location of the gap, and the dynamical imperfections.

## 1.4 Organization of this Report

Chapter 2 focuses solely on the elastic case, for both the bar and beam systems. Chapter 2 also includes the derivation of the equations of motion for the reference and hybrid systems. Chapter 3 follows the same pattern as Chapter 2, but for a viscoelastic material model. An analysis of the errors in all of the cases is conducted in Chapter 4 with the use of a parametric study of the imposed errors. Finally, Chapter 5 provides a comprehensive review of the results in Chapter 4, while comparing and discussing the results from all of the cases.

## Chapter 2

# Hybrid Simulation Theory Applied to the Elastic Bar and Beam

## 2.1 Application to the Elastic Bar

### 2.1.1 Reference System

The first case that is studied is the elastic, homogeneous bar with axial, harmonic loading on one end and a fixed boundary condition on the other, i.e. an elastic fixed-free elastic bar with axial loading. A diagram of the mechanical system is shown in Fig. 2.1. In this case

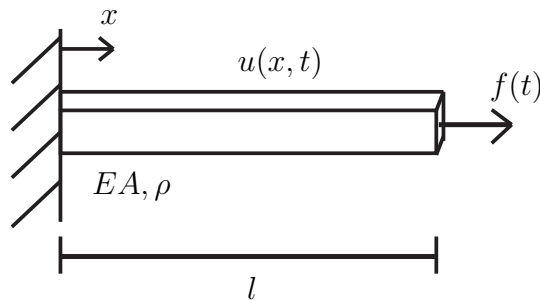


Figure 2.1: The system of an elastic fixed-free bar with applied forcing,  $f(t)$ .

the displacement is given by

$$\mathbf{u} = u(x, t)\mathbf{e}_1, \quad (2.1)$$

where  $\mathbf{e}_1$  represents the  $x$ -coordinate direction, as indicated in Fig. 2.1. For simplicity, only  $u(x, t)$  is dealt with, and the vector form is ignored. The partial differential equation governing the displacement of the bar is given by [20]

$$\rho\ddot{u} = EAu_{,xx}, \quad (2.2)$$

where  $\rho$  is the linear density,  $E$  is the elastic modulus, and  $A$  is the cross-sectional area of the bar. The forcing function,  $f(t)$ , is given by

$$f(t) = \bar{f} \exp(i\omega t), \quad (2.3)$$

where  $\bar{f}$  is the known magnitude of the applied force, and  $\omega$  is the frequency of the applied force. To solve this system, the method of separation of variables is used [6], which gives

$$u(x, t) = X(x)T(t), \quad (2.4a)$$

$$X(x) = b_1 \cos(\beta x) + b_2 \sin(\beta x), \quad (2.4b)$$

$$T(t) = \exp(i\omega t), \quad (2.4c)$$

where  $b_1$  and  $b_2$  are constants. The boundary conditions for this system are

$$u(0, t) = 0, \quad (2.5a)$$

$$EAu_{,x}(l, t) = \bar{f} \exp(i\omega t). \quad (2.5b)$$

Applying the boundary conditions to (2.4) gives

$$b_1 = 0, \quad (2.6a)$$

$$b_2 = \frac{\bar{f}}{EA\beta \cos(\beta l)}. \quad (2.6b)$$

Thus, the solution to (2.2) is given by

$$u(x, t) = \frac{\bar{f}}{EA\beta \cos(\beta l)} \sin(\beta x) \exp(i\omega t), \quad (2.7)$$

with

$$\omega^2 = \frac{EA}{\rho} \beta^2 \quad (2.8)$$

for the determination of  $\beta$ , the wavenumber.

### 2.1.2 Hybrid System

The fixed-free bar with axial loading is subjected to a hybrid system separation. The hybrid system is shown in Fig. 2.2, with the  $\mathcal{P}$ -side as the fixed side and the  $\mathcal{C}$ -side as the free side. The separation of the hybrid system is at  $x = l_1$ ; thus, in this system the displacement is given by

$$\hat{u}(x, t) = \begin{cases} \hat{u}_p(x, t) & \text{if } 0 \leq x < l_1 \\ \hat{u}_c(x, t) & \text{if } l_1 < x \leq l. \end{cases} \quad (2.9)$$

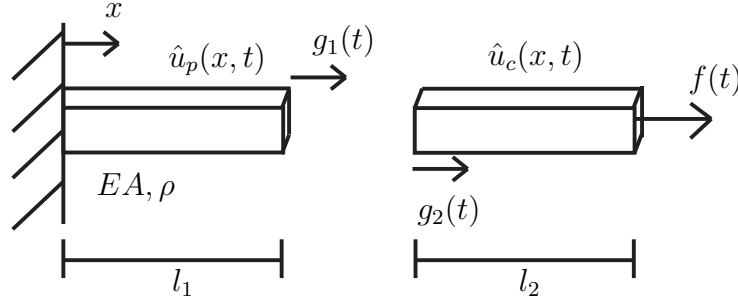


Figure 2.2: The system of an elastic fixed-free bar with applied forcing,  $f(t)$ , with hybrid separation and gap functions  $g_1(t)$  and  $g_2(t)$ ,  $l_1 + l_2 = l$ .

Again, separation of variables is applied to the system. The displacement for the hybrid system,  $\hat{u}(x, t)$ , must also satisfy (2.2), thus both  $\hat{u}_p(x, t)$  and  $\hat{u}_c(x, t)$  must independently satisfy (2.2). Assuming that the solution form for  $\hat{u}_p(x, t) = \hat{X}_p(x)\hat{T}_p(t)$  and  $\hat{u}_c(x, t) = \hat{X}_c(x)\hat{T}_c(t)$  is the same as that for  $u(x, t)$ , the following equations are produced:

$$\hat{X}_p(x) = \hat{b}_1 \cos(\hat{\beta}_p x) + \hat{b}_2 \sin(\hat{\beta}_p x), \quad (2.10a)$$

$$\hat{X}_c(x) = \hat{b}_3 \cos(\hat{\beta}_c x) + \hat{b}_4 \sin(\hat{\beta}_c x), \quad (2.10b)$$

$$\hat{T}_p(t) = \hat{T}_c(t) = \exp(i\omega t), \quad (2.10c)$$

where  $\hat{b}_1$ - $\hat{b}_4$  are constants. Since both  $\hat{u}_p(x, t)$  and  $\hat{u}_c(x, t)$  have to independently solve (2.2), when (2.10) are used, the following relation is determined:

$$\omega^2 = \frac{EA}{\rho} \hat{\beta}_p^2 = \frac{EA}{\rho} \hat{\beta}_c^2. \quad (2.11)$$

Using (2.11) along with (2.8), it is noted that  $\hat{\beta}_p = \hat{\beta}_c = \beta$ . Since (2.2) is a second order system in  $x$ , two boundary conditions are required to solve the system, one on each boundary [5]. Thus, only two gap functions are needed for this case, one for the  $\mathcal{P}$ -side and one for the  $\mathcal{C}$ -side. Following the same convention defined in Section 1.2.2,  $g_1$  is the gap function on the  $\mathcal{P}$ -side and  $g_2$  is the gap function on the  $\mathcal{C}$ -side, as indicated in Fig. 2.2. The boundary conditions for the hybrid system are

$$\hat{u}_p(0, t) = 0, \quad (2.12a)$$

$$EA\hat{u}_{c,x}(l, t) = \bar{f} \exp(i\omega t), \quad (2.12b)$$

$$\hat{u}_p(l_1, t) = g_1(t) = \bar{g}_1 \exp(i\omega t), \quad (2.12c)$$

$$\hat{u}_c(l_1, t) = g_2(t) = \bar{g}_2 \exp(i\omega t). \quad (2.12d)$$

Note, in this particular case, it is assumed that both  $g_1$  and  $g_2$  are displacements for either side of the gap. Applying the boundary conditions to (2.10) leads to the following relations:

$$\hat{b}_1 = 0, \quad (2.13a)$$

$$\bar{g}_1 = \hat{b}_2 \sin(\beta l_1), \quad (2.13b)$$

$$\bar{g}_2 = \hat{b}_3 \cos(\beta l_1) + \hat{b}_4 \sin(\beta l_1), \quad (2.13c)$$

$$\bar{f} = \beta EA(\hat{b}_4 \cos(\beta l) - \hat{b}_3 \sin(\beta l)). \quad (2.13d)$$

Using (2.13), the solutions for  $\hat{u}_p(x, t)$  and  $\hat{u}_c(c, t)$  become

$$\hat{u}_p(x, t) = \frac{\bar{g}_1}{\sin(\beta l_1)} \sin(\beta x) \exp(i\omega t) \quad (2.14)$$

and

$$\hat{u}_c(x, t) = \left( \bar{g}_2 \cos(\beta(x - l)) + \frac{\bar{f}}{EA\beta} \sin(\beta(x - l_1)) \right) \frac{\exp(i\omega t)}{\cos(\beta l_2)}. \quad (2.15)$$

### 2.1.3 Non-Dimensionalization and Determination of $g_k$

Now that (2.7), (2.14), and (2.15) have been determined, both the reference and the hybrid systems have been completely solved in terms of displacement. At this point, it is beneficial to non-dimensionalize these equations. Thus, the following relations are used:

$$\xi = \frac{u}{l}, \quad y = \frac{x}{l}, \quad (2.16a)$$

$$F = \frac{\bar{f}}{EA}, \quad (2.16b)$$

$$c = \sqrt{\frac{EA}{\rho}}, \quad \bar{\omega} = \frac{c\pi}{l2}, \quad \Omega = \frac{\omega}{\bar{\omega}}, \quad \tau = \bar{\omega}t, \quad (2.16c)$$

$$\kappa = \beta l = \frac{\pi}{2}\Omega, \quad (2.16d)$$

$$G_1 = \frac{\bar{g}_1}{l}, \quad G_2 = \frac{\bar{g}_2}{l}, \quad (2.16e)$$

$$L_1 = \frac{l_1}{l}, \quad L_2 = 1 - L_1, \quad (2.16f)$$

where  $\bar{\omega}$  is the lowest resonant frequency of the elastic fixed-free bar [20]. Thus (2.7), (2.14), and (2.15) become

$$\xi(y, \tau) = \frac{F}{\kappa \cos(\kappa)} \sin(\kappa y) \exp(i\Omega\tau), \quad (2.17)$$

$$\hat{\xi}_p(y, \tau) = \frac{G_1}{\sin(\kappa L_1)} \sin(\kappa y) \exp(i\Omega\tau), \quad (2.18)$$

$$\hat{\xi}_c(y, \tau) = \left( G_2 \cos(\kappa(y - 1)) + \frac{F}{\kappa} \sin(\kappa(y - L_1)) \right) \frac{\exp(i\Omega\tau)}{\cos(\kappa L_2)}. \quad (2.19)$$

For the rest of this section, unless stated otherwise, all new variables or quantities are assumed to be dimensionless.

Currently,  $G_1$  and  $G_2$  are just concepts and need to be determined in order for the equations to be analyzed. In order to determine the equations for  $G_1$  and  $G_2$ , the following conditions are created to relate the displacements and forces, modulo some constants, on either side of the gap:

$$\hat{\xi}_c(L_1, \tau) = \hat{\xi}_p(L_1, \tau)(1 + \epsilon_1) \exp(i\Omega d_1), \quad (2.20a)$$

$$\hat{\xi}_{c,y}(L_1, \tau) = \hat{\xi}_{p,y}(L_1, \tau)(1 + \epsilon_2) \exp(i\Omega d_2), \quad (2.20b)$$

where  $\epsilon_1$  is the magnitude error in the displacement that occurs at the gap in the hybrid system and  $\epsilon_2$  is the magnitude error in the force that occurs at the gap. Also,  $d_1$  is the dimensionless time-delay error of the displacement that occurs at the gap in the hybrid system and  $d_2$  is the dimensionless time-delay error of the force that occurs at the gap.  $\epsilon_k$  and  $d_k$  are the error parameters for the system. Solving for  $G_1$  and  $G_2$  gives

$$G_1 = \frac{F}{\kappa \cos(\kappa L_2) G_d}, \quad (2.21a)$$

$$G_2 = (1 + \epsilon_1) \exp(i\Omega d_1) G_1, \quad (2.21b)$$

where

$$G_d = (1 + \epsilon_2) \exp(i\Omega d_2) \cot(\kappa L_1) - (1 + \epsilon_1) \exp(i\Omega d_1) \tan(\kappa L_2). \quad (2.21c)$$

## 2.2 Application to the Elastic Beam

### 2.2.1 Reference System

The second case that is studied is that of the elastic, homogeneous beam pinned on both ends with harmonic moment applied to one end, i.e. an elastic pinned-pinned beam with harmonic moment. A diagram of the mechanical system is shown in Fig. 2.3. In this case the displacement is given by (2.22):

$$\mathbf{w} = w(x, t) \mathbf{e}_3. \quad (2.22)$$

Where  $\mathbf{e}_3$  represents the  $z$ -coordinate direction as indicated in Fig. 2.3. Again, the vector form is ignored, and only  $w(x, t)$  is considered. The known partial differential equation that governs the motion of the mechanical system is given by [10]

$$\rho \ddot{w} = -EI w_{,xxxx}, \quad (2.23)$$

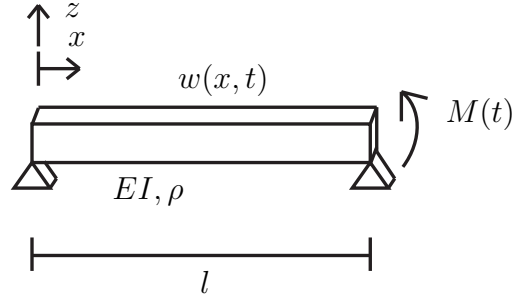


Figure 2.3: The system of an elastic pinned-pinned beam with applied moment,  $M(t)$ .

where  $\rho$  is the linear mass density,  $E$  is the elastic modulus, and  $I$  is the second moment of area of the beam. The applied moment,  $M$ , is described by

$$M(t) = \bar{M} \exp(i\omega t), \quad (2.24)$$

where  $\bar{M}$  is the magnitude of the applied moment and  $\omega$  is the frequency of the applied moment. Similar to the bar case, separation of variables is used to solve this system, which gives

$$w(x, t) = X(x)T(t), \quad (2.25a)$$

$$X(x) = b_1 \cos(\beta x) + b_2 \sin(\beta x) + b_3 \cosh(\beta x) + b_4 \sinh(\beta x), \quad (2.25b)$$

$$T(t) = \exp(i\omega t), \quad (2.25c)$$

where  $b_1$ - $b_4$  are constants. The boundary conditions for this system are

$$w(0, t) = 0, \quad (2.26a)$$

$$w(l, t) = 0, \quad (2.26b)$$

$$w_{,xx}(0, t) = 0, \quad (2.26c)$$

$$EIw_{,xx}(l, t) = \bar{M} \exp(i\omega t). \quad (2.26d)$$

Applying these boundary conditions to (2.25) gives

$$b_1 = 0, \quad (2.27a)$$

$$b_2 = \frac{-\bar{M}}{2EI\beta^2 \sin(\beta l)}, \quad (2.27b)$$

$$b_3 = 0, \quad (2.27c)$$

$$b_4 = \frac{\bar{M}}{2EI\beta^2 \sinh(\beta l)}. \quad (2.27d)$$

Thus, the solution to (2.23) is given by

$$w(x, t) = \left( \frac{-\bar{M} \sin(\beta x)}{2EI\beta^2 \sin(\beta l)} + \frac{\bar{M} \sinh(\beta x)}{2EI\beta^2 \sinh(\beta l)} \right) \exp(i\omega t), \quad (2.28)$$

with

$$\omega^2 = \frac{EI}{\rho} \beta^4 \quad (2.29)$$

for the determination of  $\beta$ , the wavenumber.

### 2.2.2 Hybrid System

The pinned-pinned beam is now subjected to a hybrid system separation. The hybrid system is shown in Fig. 2.4, where the  $\mathcal{P}$ -side is the left side, without the applied moment, and the  $\mathcal{C}$ -side is the right side, with the applied moment. The separation of the hybrid

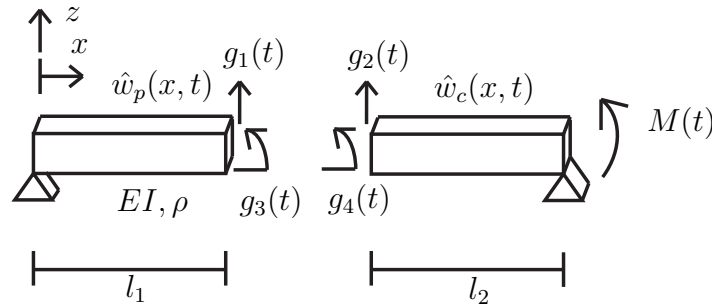


Figure 2.4: The system of an elastic pinned-pinned beam with applied moment,  $M(t)$ , with hybrid separation and gap functions  $g_1(t)$ ,  $g_2(t)$ ,  $g_3(t)$ , and  $g_4(t)$ ,  $l_1 + l_2 = l$ .

system occurs at  $x = l_1$ , thus, in this system, the displacement is given by

$$\hat{w}(x, t) = \begin{cases} \hat{w}_p(x, t) & \text{if } 0 \leq x < l_1 \\ \hat{w}_c(x, t) & \text{if } l_1 < x \leq l. \end{cases} \quad (2.30)$$

Separation of variables is applied to the system, giving  $\hat{w}_p(x, t) = \hat{X}_p(x)\hat{T}_p(t)$  and  $\hat{w}_c(x, t) = \hat{X}_c(x)\hat{T}_c(t)$ , which both must independently satisfy (2.23). This leads to the following equations:

$$\hat{X}_p(x) = \hat{b}_1 \cos(\beta_p x) + \hat{b}_2 \sin(\beta_p x) + \hat{b}_3 \cosh(\beta_p x) + \hat{b}_4 \sinh(\beta_p x), \quad (2.31a)$$

$$\hat{X}_c(x) = \hat{b}_5 \cos(\beta_c x) + \hat{b}_6 \sin(\beta_c x) + \hat{b}_7 \cosh(\beta_c x) + \hat{b}_8 \sinh(\beta_c x), \quad (2.31b)$$

$$\hat{T}_p(t) = \hat{T}_c(t) = \exp(i\omega t), \quad (2.31c)$$

where  $\hat{b}_1$ - $\hat{b}_8$  are constants. Since  $\hat{w}_p$  and  $\hat{w}_c$  must both independently satisfy (2.23), the following results are reached:

$$\omega^2 = \frac{EI}{\rho} \hat{\beta}_p^4 = \frac{EI}{\rho} \hat{\beta}_c^4. \quad (2.32)$$

Using (2.32) in conjunction with (2.29), it is noted that  $\beta = \hat{\beta}_p = \hat{\beta}_c$ , similar to the elastic fixed-free bar case. Since (2.23) is a fourth order system in  $x$ , four boundary conditions are required to solve this system, two on each boundary [5]. Thus, four gap functions are required to solve this system, two for the  $\mathcal{P}$ -side and two for the  $\mathcal{C}$ -side. Following the same convention defined in Section 1.2.2,  $g_1$  and  $g_3$  are the gap functions for the  $\mathcal{P}$ -side, and  $g_2$  and  $g_4$  are the gap functions for the  $\mathcal{C}$ -side, as indicated in Fig. 2.4. Thus, the boundary conditions for the hybrid system become

$$\hat{w}_p(0, t) = 0, \quad (2.33a)$$

$$\hat{w}_{p,xx}(0, t) = 0, \quad (2.33b)$$

$$\hat{w}_c(l, t) = 0, \quad (2.33c)$$

$$EI\hat{w}_{c,xx}(l, t) = \bar{M} \exp(i\omega t), \quad (2.33d)$$

$$\hat{w}_p(l_1, t) = g_1(t) = \bar{g}_1 \exp(i\omega t), \quad (2.33e)$$

$$\hat{w}_c(l_1, t) = g_2(t) = \bar{g}_2 \exp(i\omega t), \quad (2.33f)$$

$$\hat{w}_{p,x}(l_1, t) = g_3(t) = \bar{g}_3 \exp(i\omega t), \quad (2.33g)$$

$$\hat{w}_{c,x}(l_1, t) = g_4(t) = \bar{g}_4 \exp(i\omega t). \quad (2.33h)$$

Note that in this particular case,  $g_1$  and  $g_2$  are displacements and  $g_3$  and  $g_4$  are rotations at the interface. Using these boundary conditions leads to the following relations:

$$\hat{b}_1 = 0, \quad (2.34a)$$

$$\hat{b}_3 = 0, \quad (2.34b)$$

$$\hat{b}_2 = \frac{-\left(\cosh(\beta l_1)\bar{g}_1 - \sinh(\beta l_1)\frac{\bar{g}_3}{\beta}\right)}{\cos(\beta l_1)\sinh(\beta l_1) - \sin(\beta l_1)\cosh(\beta l_1)}, \quad (2.34c)$$

$$\hat{b}_4 = \frac{\cos(\beta l_1)\bar{g}_1 - \sin(\beta l_1)\frac{\bar{g}_3}{\beta}}{\cos(\beta l_1)\sinh(\beta l_1) - \sin(\beta l_1)\cosh(\beta l_1)}, \quad (2.34d)$$

$$\hat{b}_5 \cos(\beta l) + \hat{b}_6 \sin(\beta l) + \hat{b}_7 \cosh(\beta l) + \hat{b}_8 \sinh(\beta l) = 0, \quad (2.34e)$$

$$\hat{b}_5 \cos(\beta l_1) + \hat{b}_6 \sin(\beta l_1) + \hat{b}_7 \cosh(\beta l_1) + \hat{b}_8 \sinh(\beta l_1) = \bar{g}_2, \quad (2.34f)$$

$$\beta^2 \left(-\hat{b}_5 \cos(\beta l) - \hat{b}_6 \sin(\beta l) + \hat{b}_7 \cosh(\beta l) + \hat{b}_8 \sinh(\beta l)\right) = \frac{\bar{M}}{EI}, \quad (2.34g)$$

$$\beta \left(-\hat{b}_5 \sin(\beta l_1) + \hat{b}_6 \cos(\beta l_1) + \hat{b}_7 \sinh(\beta l_1) + \hat{b}_8 \cosh(\beta l_1)\right) = \bar{g}_4. \quad (2.34h)$$

Due to the complexity of the solutions to  $\hat{w}_p$  and  $\hat{w}_c$ , the following functions are defined for convenience:

$$A_1(x) = \sin(x) - \sinh(x), \quad (2.35a)$$

$$A_2(x) = \sin(x) + \sinh(x), \quad (2.35b)$$

$$B_1(x) = \cosh(x) - \cos(x), \quad (2.35c)$$

$$B_2(x) = \cosh(x) + \cos(x), \quad (2.35d)$$

$$P_1(x) = \sin(x) \sinh(x), \quad (2.35e)$$

$$P_2(x) = \cos(x) \cosh(x), \quad (2.35f)$$

$$D_1(x, y) = \cosh(x) \sin(y) + \cos(x) \sinh(y), \quad (2.35g)$$

$$D_2(x, y) = \cosh(x) \sin(y) - \cos(x) \sinh(y), \quad (2.35h)$$

$$D_3(x, y) = \sinh(x) \sin(y) - \sin(x) \sinh(y). \quad (2.35i)$$

Using (2.34) and (2.35), the solutions to  $\hat{w}_p(x, t)$  and  $\hat{w}_c(x, t)$  become

$$\hat{w}_p(x, t) = \frac{\bar{g}_1 D_2(\beta l_1, \beta x) - \frac{\bar{g}_3}{\beta} D_3(\beta l_1, \beta x)}{D_2(\beta l_1, \beta l_1)} \exp(i\omega t), \quad (2.36)$$

$$\begin{aligned} \hat{w}_c(x, t) = & \left( \frac{\bar{M}}{2EI\beta^2} \left( A_1(\beta l_2) B_1(\beta(x - l_1)) - B_1(\beta l_2) A_1(\beta(x - l_1)) \right) \right. \\ & \left. - \bar{g}_2 D_2(\beta l_2, \beta(x - l)) + \frac{\bar{g}_4}{\beta} D_3(\beta(x - l), \beta l_2) \right) \frac{\exp(i\omega t)}{D_2(\beta l_2, \beta l_2)}. \end{aligned} \quad (2.37)$$

### 2.2.3 Non-Dimensionalization and Determination of $g_k$

First, (2.35) are applied to (2.28) to get the solution for the reference system in the same format as (2.36) and (2.37), which produces

$$w(x, t) = \frac{\bar{M} D_3(\beta x, \beta l)}{2EI\beta^2 P_1(\beta l)} \exp(i\omega t). \quad (2.38)$$

Similar to the bar case, it is now beneficial to non-dimensionalize these equations. Thus, the following relations are used:

$$\eta = \frac{w}{l}, \quad y = \frac{x}{l}, \quad (2.39a)$$

$$\mu = \frac{\bar{M}l}{EI}, \quad (2.39b)$$

$$\bar{\omega} = \sqrt{\frac{EI}{\rho}} \frac{\pi^2}{l^2}, \quad \Omega = \frac{\omega}{\bar{\omega}}, \quad \tau = \bar{\omega}t, \quad (2.39c)$$

$$\kappa = \beta l = \pi\sqrt{\Omega}, \quad (2.39d)$$

$$G_1 = \frac{\bar{g}_1}{l}, \quad G_2 = \frac{\bar{g}_2}{l}, \quad G_3 = \bar{g}_3, \quad G_4 = \bar{g}_4, \quad (2.39e)$$

$$L_1 = \frac{l_1}{l}, \quad L_2 = 1 - L_1, \quad (2.39f)$$

where  $\bar{\omega}$  is the lowest resonant frequency of the elastic pinned-pinned beam [10]. Thus (2.36), (2.37), and (2.38) become

$$\eta(y, \tau) = \frac{\mu D_3(\kappa y, \kappa)}{2\kappa^2 P_1(\kappa)} \exp(i\Omega\tau), \quad (2.40)$$

$$\hat{\eta}_p(y, \tau) = \frac{G_1 D_2(\kappa L_1, \kappa y) - \frac{G_3}{\kappa} D_3(\kappa L_1, \kappa y)}{D_2(\kappa L_1, \kappa L_1)} \exp(i\Omega\tau), \quad (2.41)$$

$$\begin{aligned} \hat{\eta}_c(y, \tau) = & \left( \frac{\mu}{2\kappa^2} \left( A_1(\kappa L_2) B_1(\kappa(y - L_1)) - B_1(\kappa L_2) A_1(\kappa(y - L_1)) \right) \right. \\ & \left. - G_2 D_2(\kappa L_2, \kappa(y - 1)) + \frac{G_4}{\kappa} D_3(\kappa(y - 1), \kappa L_2) \right) \frac{\exp(i\Omega\tau)}{D_2(\kappa L_2, \kappa L_2)}. \end{aligned} \quad (2.42)$$

For the rest of this section, unless stated otherwise, all new variables or quantities are assumed to be dimensionless.

Now,  $G_1$ ,  $G_2$ ,  $G_3$ , and  $G_4$  need to be determined in order to perform an analysis of the above equations. In order to determine the equations for  $G_1$ ,  $G_2$ ,  $G_3$ , and  $G_4$ , the following conditions are imposed to relate the displacements, rotations, moments, and shears, modulo some constants, on either side of the gap:

$$\hat{\eta}_c(L_1, \tau) = \hat{\eta}_p(L_1, \tau)(1 + \epsilon_1) \exp(i\Omega d_1), \quad (2.43a)$$

$$\hat{\eta}_{c,y}(L_1, \tau) = \hat{\eta}_{p,y}(L_1, \tau)(1 + \epsilon_3) \exp(i\Omega d_3), \quad (2.43b)$$

$$\hat{\eta}_{c,yy}(L_1, \tau) = \hat{\eta}_{p,yy}(L_1, \tau)(1 + \epsilon_2) \exp(i\Omega d_2), \quad (2.43c)$$

$$\hat{\eta}_{c,yyy}(L_1, \tau) = \hat{\eta}_{p,yyy}(L_1, \tau)(1 + \epsilon_4) \exp(i\Omega d_4), \quad (2.43d)$$

where  $\epsilon_k$  for  $k = 1, 2, 3, 4$  are the magnitude errors for the displacement, moment, rotation, and shear, respectively, at the gap and  $d_k$  are the time delays of the displacement, moment, rotation, and shear at the gap.  $\epsilon_k$  and  $d_k$  are the error parameters for the system. Solving for  $G_1$ ,  $G_2$ ,  $G_3$ , and  $G_4$  gives

$$\begin{aligned} G_1 = & \frac{\mu}{D_2(\kappa L_2, \kappa L_2) G_d} \left( A_2(\kappa L_2)(1 + \epsilon_3) \exp(i\Omega d_3) - \frac{A_1(\kappa L_2) D_1(\kappa L_1, \kappa L_1)}{D_2(\kappa L_1, \kappa L_1)} (1 + \epsilon_4) \exp(i\Omega d_4) \right. \\ & \left. + \frac{2B_1(\kappa L_2) P_1(\kappa L_1)}{D_2(\kappa L_1, \kappa L_1)} (1 + \epsilon_2) \exp(i\Omega d_2) \right), \end{aligned} \quad (2.44a)$$

$$\begin{aligned} G_3 = & \frac{\mu\kappa}{D_2(\kappa L_2, \kappa L_2) G_d} \left( -B_2(\kappa L_2)(1 + \epsilon_1) \exp(i\Omega d_1) - \frac{2A_1(\kappa L_2) P_2(\kappa L_1)}{D_2(\kappa L_1, \kappa L_1)} (1 + \epsilon_4) \exp(i\Omega d_4) \right. \\ & \left. + \frac{B_1(\kappa L_2) D_1(\kappa L_1, \kappa L_1)}{D_2(\kappa L_1, \kappa L_1)} (1 + \epsilon_2) \exp(i\Omega d_2) \right), \end{aligned} \quad (2.44b)$$

$$G_2 = G_1(1 + \epsilon_1) \exp(i\Omega d_1), \quad (2.44c)$$

$$G_4 = G_3(1 + \epsilon_3) \exp(i\Omega d_3), \quad (2.44d)$$

where

$$\begin{aligned} G_d = & \kappa^2 \left( (1 + \epsilon_1)(1 + \epsilon_3) \exp(i\Omega(d_1 + d_3)) + (1 + \epsilon_2)(1 + \epsilon_4) \exp(i\Omega(d_2 + d_4)) \right) \\ & - \frac{\kappa^2 D_1(\kappa L_1, \kappa L_1) D_1(\kappa L_2, \kappa L_2)}{D_2(\kappa L_1, \kappa L_1) D_2(\kappa L_2, \kappa L_2)} \left( (1 + \epsilon_1)(1 + \epsilon_4) \exp(i\Omega(d_1 + d_4)) \right. \\ & \left. + (1 + \epsilon_2)(1 + \epsilon_3) \exp(i\Omega(d_2 + d_3)) \right) \\ & - \frac{\kappa^2}{D_2(\kappa L_1, \kappa L_1) D_2(\kappa L_2, \kappa L_2)} \left( 4P_1(\kappa L_1) P_2(\kappa L_2) (1 + \epsilon_1)(1 + \epsilon_2) \exp(i\Omega(d_1 + d_2)) \right. \\ & \left. + 4P_1(\kappa L_2) P_2(\kappa L_1) (1 + \epsilon_3)(1 + \epsilon_4) \exp(i\Omega(d_3 + d_4)) \right). \end{aligned} \quad (2.44e)$$

## Chapter 3

# Hybrid Simulation Theory Applied to the Viscoelastic Bar and Beam

### 3.1 Application to the Viscoelastic Bar

The same fixed-free bar model that was used in Section 2.1 is used in this section. However, instead of assuming pure elasticity, viscoelastic material effects are now considered. In order to do this, the complex elastic modulus is used,

$$E^* = E' + iE'', \quad (3.1)$$

where  $E'$  is the storage modulus and  $E''$  is the loss modulus [9]. The standard 3-parameter Maxwell model for a linear viscoelastic solid is used in this report, which gives the following result [21]:

$$E' = E_\infty + \frac{\omega^2 t_r^2}{1 + \omega^2 t_r^2} (E_0 - E_\infty), \quad (3.2a)$$

$$E'' = \frac{\omega t_r}{1 + \omega^2 t_r^2} (E_0 - E_\infty), \quad (3.2b)$$

where  $E_0$  is the instantaneous modulus,  $E_\infty$  is the equilibrium modulus, which are different than the elastic modulus,  $E$ , that was used in Section 2.1. The relaxation time,  $t_r$ , is given by

$$t_r = \frac{1}{\bar{\omega}\zeta}. \quad (3.3)$$

The parameter  $\zeta$  is the non-dimensional damping frequency, which determines where the majority of the damping is applied in the frequency domain. Since  $E^*$  is complex, it can be expressed in polar form by

$$E^* = |E^*| \exp(i\delta), \quad (3.4a)$$

$$|E^*| = \sqrt{E'^2 + E''^2}, \quad (3.4b)$$

$$\delta = \tan^{-1} \left( \frac{E''}{E'} \right). \quad (3.4c)$$

Using the same solution form as in (2.4), (2.8) now becomes

$$\omega^2 = \frac{|E^*|A}{\rho} \beta^2 \exp(i\delta). \quad (3.5)$$

Since  $\omega$ ,  $|E^*|$ ,  $A$ , and  $\rho$  are all real values,  $\beta$  must now be complex. Thus, the following result is reached for  $\beta$ :

$$\beta = \sqrt{\frac{\rho}{|E^*|A}} \omega \exp\left(\frac{-i\delta}{2}\right). \quad (3.6)$$

By applying the boundary conditions from (2.5), the following results are reached:

$$b_1 = 0, \quad (3.7a)$$

$$b_2 = \frac{\bar{f} \exp(-i\delta)}{|E^*|A\beta \cos(\beta l)}. \quad (3.7b)$$

Note that  $b_2$  has also become complex. Thus the solution now becomes

$$u(x, t) = \frac{\bar{f} \exp(-i\delta)}{|E^*|A\beta \cos(\beta l)} \sin(\beta x) \exp(i\omega t). \quad (3.8)$$

Non-dimensionalizing (3.8) leads to

$$\xi(y, \tau) = \frac{F \sin(\kappa y)}{\kappa \cos(\kappa)} \exp(i\Omega\tau). \quad (3.9)$$

Where all values have the same definition as in Section 2.1, except

$$F = \frac{\bar{f} \exp(-i\delta)}{|E^*|A}, \quad (3.10a)$$

$$c = \sqrt{\frac{|E^*|A}{\rho}}, \quad (3.10b)$$

$$\kappa = \beta l = \frac{\pi}{2} \Omega \exp\left(\frac{-i\delta}{2}\right). \quad (3.10c)$$

Note that (3.9) is exactly identical to (2.17), with the new definitions for  $F$  and  $\kappa$ . This result will hold true for the hybrid system as well. Thus, the following equations all hold for the viscoelastic fixed-free hybrid bar case, for the new definitions of  $F$  and  $\kappa$ :

$$\hat{\xi}_p(y, \tau) = \frac{G_1}{\sin(\kappa L_1)} \sin(\kappa y) \exp(i\Omega\tau), \quad (3.11)$$

$$\hat{\xi}_c(y, \tau) = \left( G_2 \cos(\kappa(y-1)) + \frac{F}{\kappa} \sin(\kappa(y-L_1)) \right) \frac{\exp(i\Omega\tau)}{\cos(\kappa L_2)}, \quad (3.12)$$

$$G_1 = \frac{F}{\kappa \cos(\kappa L_2) G_d}, \quad (3.13a)$$

$$G_2 = (1 + \epsilon_1) \exp(i\Omega d_1) G_1, \quad (3.13b)$$

$$G_d = (1 + \epsilon_2) \exp(i\Omega d_2) \cot(\kappa L_1) - (1 + \epsilon_1) \exp(i\Omega d_1) \tan(\kappa L_2). \quad (3.13c)$$

## 3.2 Application to the Viscoelastic Beam

The same pinned-pinned beam model that was used in Section 2.2 is used for the viscoelastic case. For the viscoelastic pinned-pinned beam, the complex elastic modulus is the same as that defined by (3.2). Using this form of the complex elastic modulus and the same general solution as defined by (2.25), (2.29) becomes

$$\rho\omega^2 = |E^*|I \exp(i\delta)\beta^4. \quad (3.14)$$

Again note that  $\beta$  must now be complex. Solving for  $\beta$  gives

$$\beta = \sqrt[4]{\frac{\rho}{|E^*|I}} \sqrt{\omega} \exp\left(\frac{-i\delta}{4}\right). \quad (3.15)$$

Applying the boundary conditions (2.26), the following results are reached:

$$b_1 = 0, \quad (3.16a)$$

$$b_2 = \frac{-\bar{M} \exp(-i\delta)}{2|E^*|I\beta^2 \sin(\beta l)}, \quad (3.16b)$$

$$b_3 = 0, \quad (3.16c)$$

$$b_4 = \frac{\bar{M} \exp(-i\delta)}{2|E^*|I\beta^2 \sinh(\beta l)}. \quad (3.16d)$$

Also note that  $b_2$  and  $b_4$  have become complex. The solution now becomes

$$w(x, t) = \left( \frac{-\bar{M} \exp(-i\delta) \sin(\beta x)}{2|E^*|I\beta^2 \sin(\beta l)} + \frac{\bar{M} \exp(-i\delta) \sinh(\beta x)}{2|E^*|I\beta^2 \sinh(\beta l)} \right) \exp(i\omega t). \quad (3.17)$$

Non-dimensionalizing (3.17) and applying the functions defined by (2.35) leads to

$$\eta(y, \tau) = \frac{\mu D_3(\kappa y, \kappa)}{2\kappa^2 P_1(\kappa)} \exp(i\Omega\tau), \quad (3.18)$$

where all values have the same definitions as in Section 2.2, except

$$\kappa = \beta l = \pi \sqrt{\Omega} \exp\left(\frac{-i\delta}{4}\right), \quad (3.19a)$$

$$\mu = \frac{\bar{M}l \exp(-i\delta)}{|E^*|I}. \quad (3.19b)$$

Note that the solution to the viscoelastic case, (3.18), is identical to (2.40), with the new definitions of  $\kappa$  and  $\mu$ . Therefore, the following equations all hold for the viscoelastic pinned-pinned hybrid beam case, using the new definitions of  $\kappa$  and  $\mu$ :

$$\hat{\eta}_p(y, \tau) = \frac{G_1 D_2(\kappa L_1, \kappa y) - \frac{G_3}{\kappa} D_3(\kappa L_1, \kappa y)}{D_2(\kappa L_1, \kappa L_1)} \exp(i\Omega\tau), \quad (3.20)$$

$$\begin{aligned} \hat{\eta}_c(y, \tau) = & \left( \frac{\mu}{2\kappa^2} \left( A_1(\kappa L_2) B_1(\kappa(y - L_1)) - B_1(\kappa L_2) A_1(\kappa(y - L_1)) \right) \right. \\ & \left. - G_2 D_2(\kappa L_2, \kappa(y - 1)) + \frac{G_4}{\kappa} D_3(\kappa(y - 1), \kappa L_2) \right) \frac{\exp(i\Omega\tau)}{D_2(\kappa L_2, \kappa L_2)}, \end{aligned} \quad (3.21)$$

$$\begin{aligned} G_1 = & \frac{\mu}{D_2(\kappa L_2, \kappa L_2) G_d} \left( A_2(\kappa L_2) (1 + \epsilon_3) \exp(i\Omega d_3) - \frac{A_1(\kappa L_2) D_1(\kappa L_1, \kappa L_1)}{D_2(\kappa L_1, \kappa L_1)} (1 + \epsilon_4) \exp(i\Omega d_4) \right. \\ & \left. + \frac{2B_1(\kappa L_2) P_1(\kappa L_1)}{D_2(\kappa L_1, \kappa L_1)} (1 + \epsilon_2) \exp(i\Omega d_2) \right), \end{aligned} \quad (3.22a)$$

$$\begin{aligned} G_3 = & \frac{\mu\kappa}{D_2(\kappa L_2, \kappa L_2) G_d} \left( -B_2(\kappa L_2) (1 + \epsilon_1) \exp(i\Omega d_1) - \frac{2A_1(\kappa L_2) P_2(\kappa L_1)}{D_2(\kappa L_1, \kappa L_1)} (1 + \epsilon_4) \exp(i\Omega d_4) \right. \\ & \left. + \frac{B_1(\kappa L_2) D_1(\kappa L_1, \kappa L_1)}{D_2(\kappa L_1, \kappa L_1)} (1 + \epsilon_2) \exp(i\Omega d_2) \right), \end{aligned} \quad (3.22b)$$

$$G_2 = G_1 (1 + \epsilon_1) \exp(i\Omega d_1), \quad (3.22c)$$

$$G_4 = G_3 (1 + \epsilon_3) \exp(i\Omega d_3), \quad (3.22d)$$

where

$$\begin{aligned}
 G_d = & \kappa^2 \left( (1 + \epsilon_1)(1 + \epsilon_3) \exp(i\Omega(d_1 + d_3)) + (1 + \epsilon_2)(1 + \epsilon_4) \exp(i\Omega(d_2 + d_4)) \right) \\
 & - \frac{\kappa^2 D_1(\kappa L_1, \kappa L_1) D_1(\kappa L_2, \kappa L_2)}{D_2(\kappa L_1, \kappa L_1) D_2(\kappa L_2, \kappa L_2)} \left( (1 + \epsilon_1)(1 + \epsilon_4) \exp(i\Omega(d_1 + d_4)) \right. \\
 & \left. + (1 + \epsilon_2)(1 + \epsilon_3) \exp(i\Omega(d_2 + d_3)) \right) \\
 & - \frac{\kappa^2}{D_2(\kappa L_1, \kappa L_1) D_2(\kappa L_2, \kappa L_2)} \left( 4P_1(\kappa L_1) P_2(\kappa L_2) (1 + \epsilon_1)(1 + \epsilon_2) \exp(i\Omega(d_1 + d_2)) \right. \\
 & \left. + 4P_1(\kappa L_2) P_2(\kappa L_1) (1 + \epsilon_3)(1 + \epsilon_4) \exp(i\Omega(d_3 + d_4)) \right). \tag{3.22e}
 \end{aligned}$$

## Chapter 4

# Analysis of Hybrid Simulation Theory for the Elastic and Viscoelastic Models

In the previous section, equations were established for the displacement of the reference and hybrid systems for both the bar and beam. However, in order to verify that the hybrid system equations, they need to be compared to the reference system equations with no imposed errors at the gap. If there are no imposed errors at the gap, the two sets of equations for the displacement should be identical. Thus, the first part of each of the following sections will involve a verification of the displacement equations. After the verification of the displacement equations, the effects of the error parameters on the system error will then be systematically studied.

### 4.1 Analysis of the Elastic Model

#### 4.1.1 Elastic Bar

First, (2.18) and (2.19) need to be compared with (2.17), to verify that those equations do in fact describe the correct system. Note that if all  $\epsilon_k = 0$  and  $d_k = 0$  for  $k = 1, 2$ , then the hybrid system should reduce to the reference system. Thus, in order to test the accuracy of (2.18) and (2.19),  $\epsilon_k = 0$  and  $d_k = 0$  for  $k = 1, 2$ , and then compared to (2.17), as seen in Fig. 4.1. The Matlab<sup>®</sup> programming language software package is used to make all of the graphs in this report [13]. For all of the following figures, all error parameters are assumed to be 0 unless noted otherwise in the figure. Note that in all cases the real part of the solution is used for the plotting of figures. See Appendix C for a table of all material constants and dimensions used for all of the following tests. As seen in Fig. 4.1, the two solutions, the reference system and the hybrid system, are nearly identical and the only error is due to numerical inaccuracies in the computation. Now a 10% error in the magnitude of the

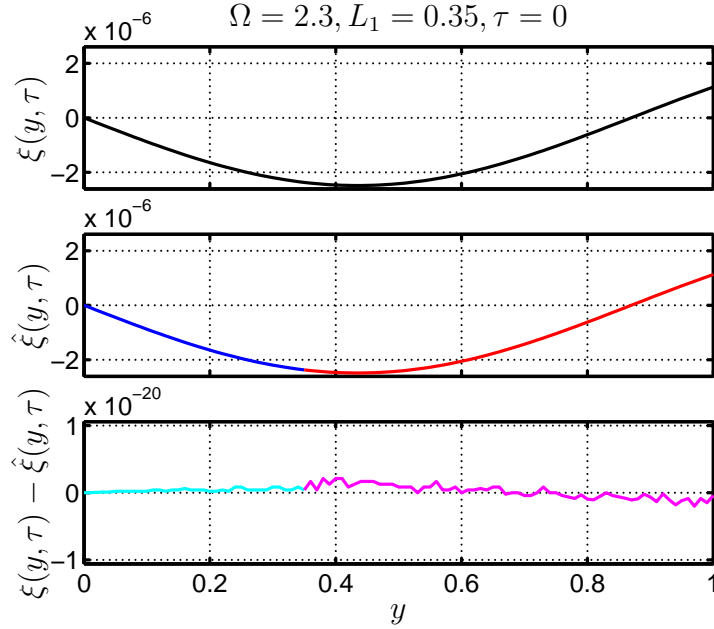


Figure 4.1: Comparison of the reference elastic fixed-free bar to the hybrid elastic fixed-free bar with no imposed error.

displacement is introduced,  $\epsilon_1 = 0.1$ , to demonstrate that the hybrid system is performing in the proper manner with introduced error. Fig. 4.2 shows a discontinuity between the two sides of the gap and that a noticeable amount of error is now present in the hybrid system based only on a displacement inaccuracy, which is to be expected. Thus, the hybrid system is performing properly with introduced error. In order for the error analysis to be conducted on this system, (1.4) is applied to this specific system, giving

$$\|e_p\|^2 = \int_0^T \int_0^{L_1} \left( \text{Re}(\xi(y, \tau) - \hat{\xi}_p(y, \tau)) \right)^2 dy d\tau, \quad (4.1a)$$

$$\|e_c\|^2 = \int_0^T \int_{L_1}^1 \left( \text{Re}(\xi(y, \tau) - \hat{\xi}_c(y, \tau)) \right)^2 dy d\tau, \quad (4.1b)$$

$$\|e\| = \sqrt{\|e_p\|^2 + \|e_c\|^2}. \quad (4.1c)$$

Where  $T$  is the period of the applied force, meaning that it changes with  $\Omega$ .  $\text{Re}(\bullet)$  is the real part of  $\bullet$ .  $\xi(y, \tau)$ ,  $\hat{\xi}_p(y, \tau)$ , and  $\hat{\xi}_c(y, \tau)$  come from (2.17), (2.18), and (2.19) respectively. Appendix A has a complete derivation of an analytical solution for (4.1a) and (4.1b), which will be used for all of the error analysis of the elastic fixed-free bar. The error produced by (4.1c) is analyzed in a parametric study by varying the multiple parameters that affect the error, including  $\Omega$ ,  $\epsilon_1$ , and  $d_1$ .

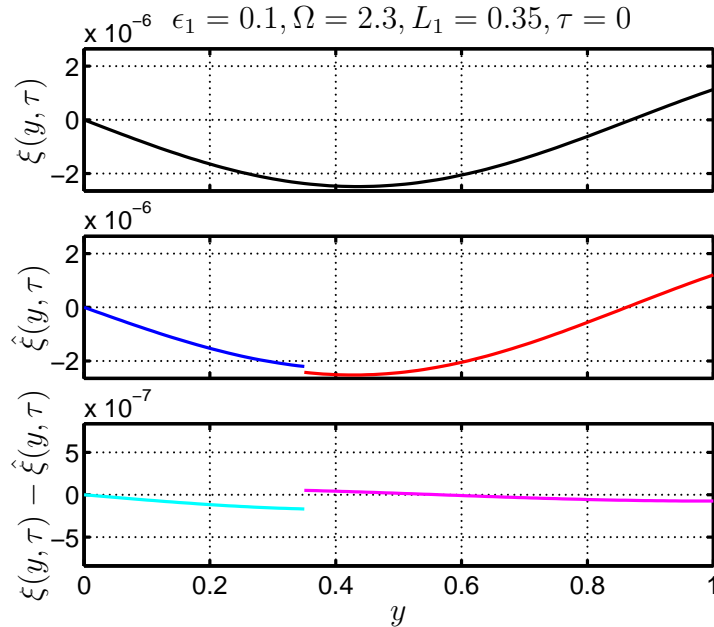


Figure 4.2: Comparison of the reference elastic fixed-free bar to the hybrid elastic fixed-free bar with  $\epsilon_1 = 0.1$ .

### Frequency Sweeps

The first parameter that is studied is the applied frequency,  $\Omega$ . For specified choices of the other parameters,  $\Omega$  is swept from  $10^{-1}$  to  $10^2$  to give a comprehensive look at the effects of frequency on the error of the hybrid system. Figs. 4.3-4.6 show the error of the system with only one error parameter used at a time. This allows for a study of the effect of each of those parameters individually. In all case, the error grows extremely large at the resonant frequencies of the reference system, i.e.  $\Omega = 1, 3, 5, \dots$ , which is to be expected, as displacement of the reference system becomes unbounded. Also note that in each case there are specific values of  $\Omega$  where the error drops to relatively small values. For  $\epsilon_1$  and  $d_1$ , these drops occur when  $\sin(\kappa L_1) = 0$ , and for  $\epsilon_2$  and  $d_2$  these drops occur when  $\cos(\kappa L_1) = 0$ . Recall that  $\kappa = \frac{\pi}{2}\Omega$ . Thus, the location of the gap is very important on the error that the hybrid system encounters. After careful inspection of Figs. 4.5 and 4.6 there are more drops in error than those caused by the above mentioned effects. These extra drops in error are caused by  $d_k = \frac{2\pi n}{\Omega}$  for  $n = 1, 2, 3, \dots$ , or when  $d_k$  is an integer multiple of the period. Physically this makes sense because it means that the time-delay in the system causes the displacement or force to be behind or ahead by a complete period, meaning that the hybrid system, by accident, is behaving exactly the same as the reference system. After careful inspection of Figs. 4.3 and 4.4 there are “mini” peaks that occur near the resonant frequency peaks. The location of these mini peaks are determined by

$$\Omega = n + .21(-1)^k \text{sgn}(\epsilon_k) \sqrt{|\epsilon_k|} \sin(n\pi L_1) \text{ for } n = 1, 3, 5, \dots \text{ and } k = 1, 2. \quad (4.2)$$

Note, (4.2) is only valid for  $|\epsilon_k| < 0.5$ . Thus, for different values of  $\epsilon_k$  or  $L_1$ , these mini peaks will move to different locations in the frequency space. Next, multiple error parameters are placed into a single system, as shown in Figs. 4.7-4.10. Fig. 4.7 has  $\epsilon_1 = 0.1$  and  $\epsilon_2 = 0.1$ , and note that there are no longer any drops in error or any mini peaks, which were associated with  $\epsilon_k$  for either  $k = 1$  or  $k = 2$ . This indicates that equivalent values of  $\epsilon_1$  and  $\epsilon_2$  result in a cancellation of both drops and extra peaks of error. However, it is noted that as either  $\epsilon_1$  or  $\epsilon_2$  begins to outweigh the other, the effects seen in the individual error figures begin to reappear. Fig. 4.8 has  $\epsilon_1 = 0.1$  and  $d_1 = 0.1$  which again has the drops in error associated with the individual error parameters. This makes sense as these drops in error occurred at the same frequency for the individual error parameters, and thus should be present for the combined errors. However, the mini peaks associated with  $\epsilon_1$  are no longer present in the error curve. Also, the error drops from the time-delay being an integer multiple of the frequency are also gone, which makes sense because the error caused by  $\epsilon_1$  will outweigh the error drop due to  $d_1$ . Fig. 4.9 has  $\epsilon_1 = 0.1$  and  $d_2 = 0.1$ , which, similar to Fig. 4.7, no longer has the error drops associated with the individual error parameters. This leads to the conclusion that whenever there is an error parameter with  $k = 1$  and another error parameter with  $k = 2$  present in a system, then the error drops disappear from the curves. Also, similar to Figs. 4.7 and 4.8, the mini peaks associated with  $\epsilon_1$  are gone. This indicates that the mini peaks are highly sensitive to the error parameters that are present in the system. Again, the error drop due  $d_2$  equaling an integer multiple of the period also disappears, for the same reason mentioned above for Fig. 4.8. Fig. 4.10 has  $d_1 = 0.1$  and  $d_2 = 0.1$ , which also does not have the error drops associated with the individual error parameters alone. However, the error drop due to  $d_i$  equaling an integer multiple is still present for  $d_1 = d_2 = 0.1$ . However, this only happens when  $d_1 = nd_2$  for  $n = 1, 2, 3, \dots$ , if this does not hold, then that error drop will also no longer be present.

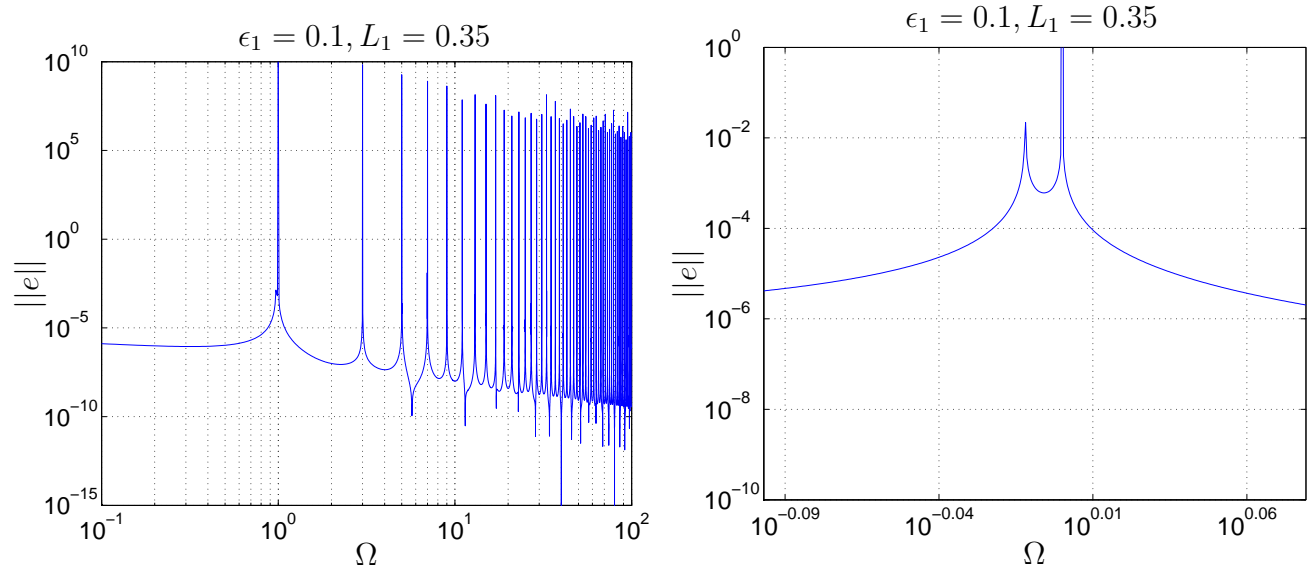


Figure 4.3: (a) A frequency sweep of the elastic fixed-free bar with  $\epsilon_1 = 0.1$  on a log-log plot. (b) A zoomed in plot showing the mini peak

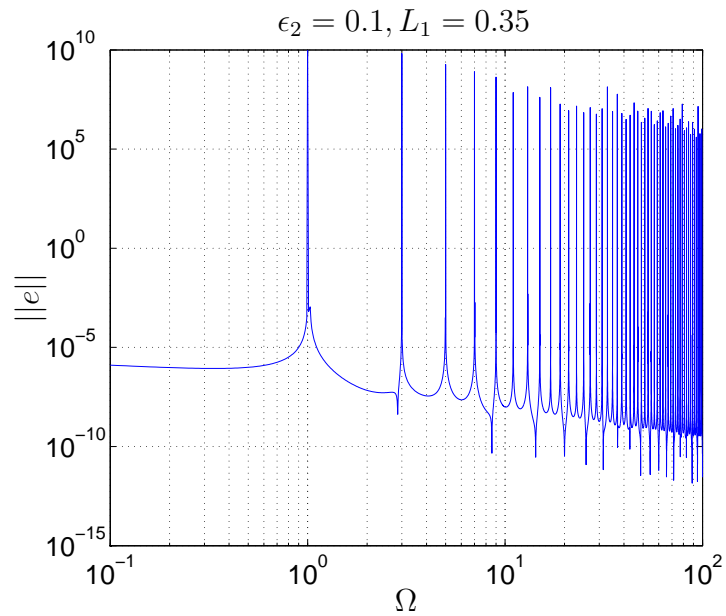


Figure 4.4: A frequency sweep of the elastic fixed-free bar with  $\epsilon_2 = 0.1$  on a log-log plot.

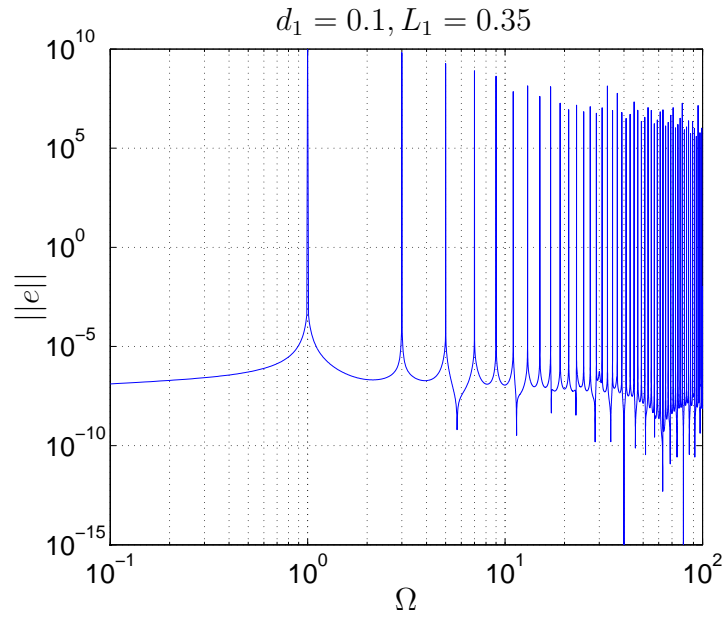


Figure 4.5: A frequency sweep of the elastic fixed-free bar with  $d_1 = 0.1$  on a log-log plot.

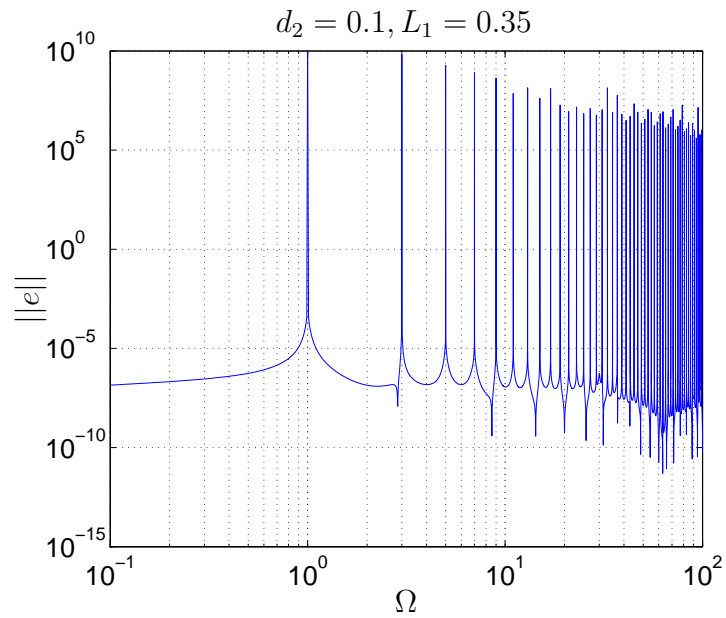


Figure 4.6: A frequency sweep of the elastic fixed-free bar with  $d_2 = 0.1$  on a log-log plot.

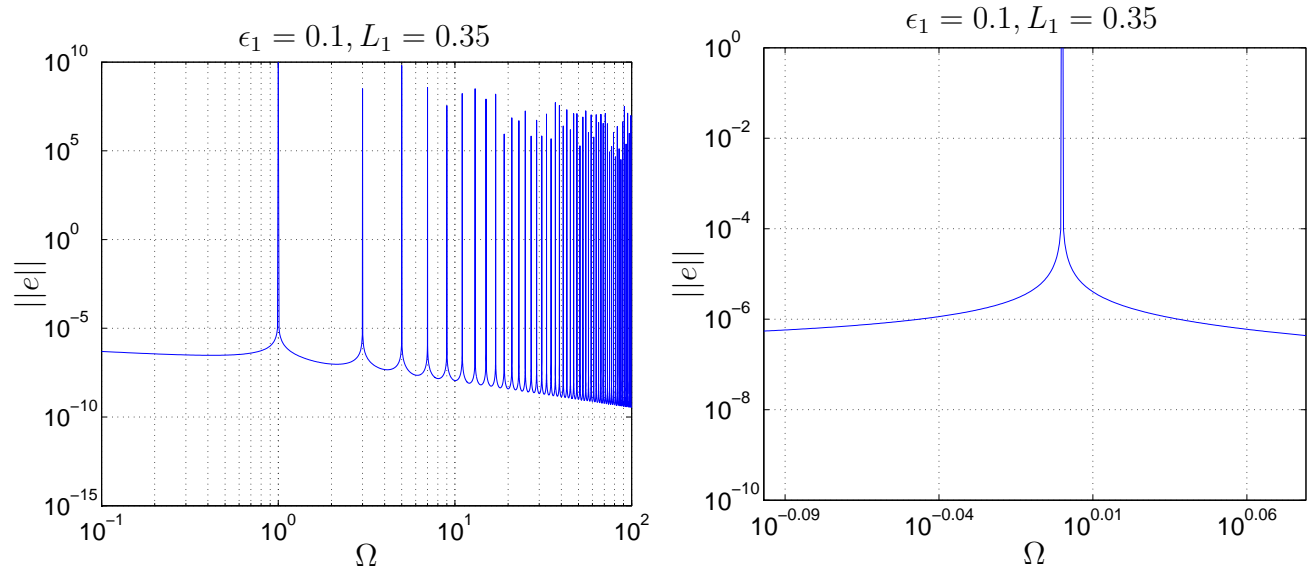


Figure 4.7: (a) A frequency sweep of the elastic fixed-free bar with  $\epsilon_1 = 0.1$  and  $\epsilon_2 = 0.1$  on a log-log plot. (b) A zoomed in plot missing the mini peak

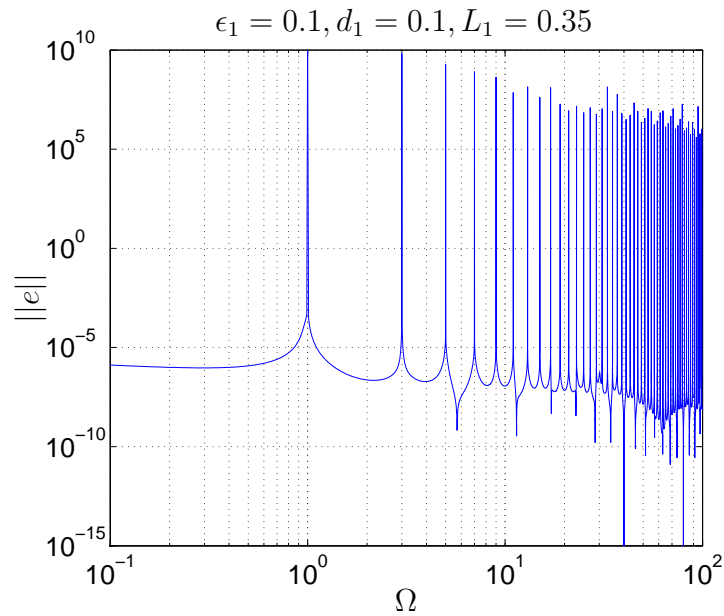


Figure 4.8: A frequency sweep of the elastic fixed-free bar with  $\epsilon_1 = 0.1$  and  $d_1 = 0.1$  on a log-log plot.

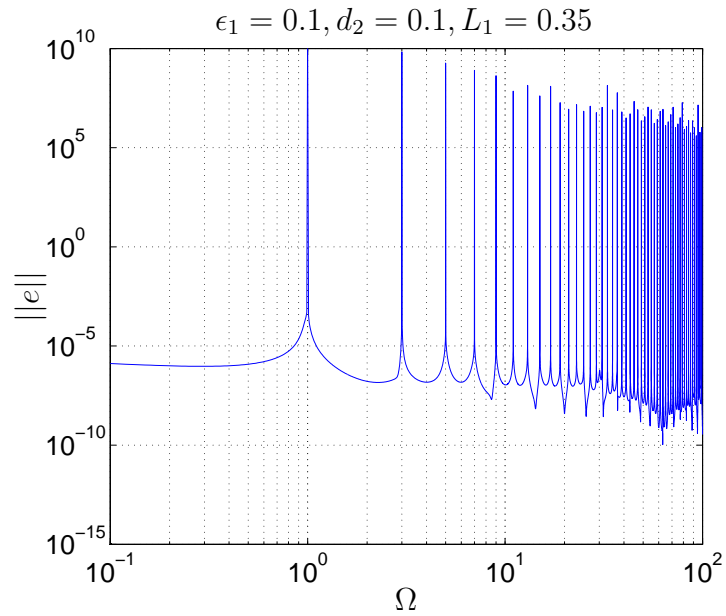


Figure 4.9: A frequency sweep of the elastic fixed-free bar with  $\epsilon_1 = 0.1$  and  $d_2 = 0.1$  on a log-log plot.

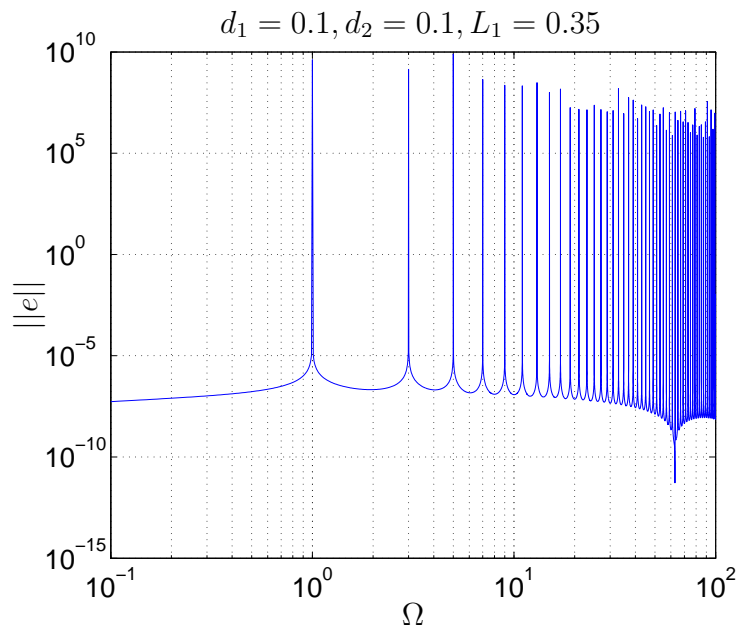


Figure 4.10: A frequency sweep of the elastic fixed-free bar with  $d_1 = 0.1$  and  $d_2 = 0.1$  on a log-log plot.

### $\epsilon_1$ Domain

Next, the error in the  $\epsilon_1$  domain is studied at specified frequencies. The frequencies were chosen to provide a comprehensive spectrum. Fig. 4.11 shows the error in the  $\epsilon_1$  domain for multiple frequencies. As seen in Fig. 4.11, there is always one error peak for each frequency, somewhere in the  $\epsilon_1$  domain. These error peaks in the  $\epsilon_1$  domain are the cause of the mini peaks in the frequency domain. Also, note that as  $\epsilon_1$  becomes large in both the positive and negative directions, the error of the curves tend to level off and the only areas of large error change are near the peaks and near  $\epsilon_1 = 0$ . And, as expected, the error approaches zero as  $\epsilon_1$  approaches zero in all cases. All of the general results for the  $\epsilon_1$  domain are similar for the  $\epsilon_2$  domain, and thus are not shown in this report.

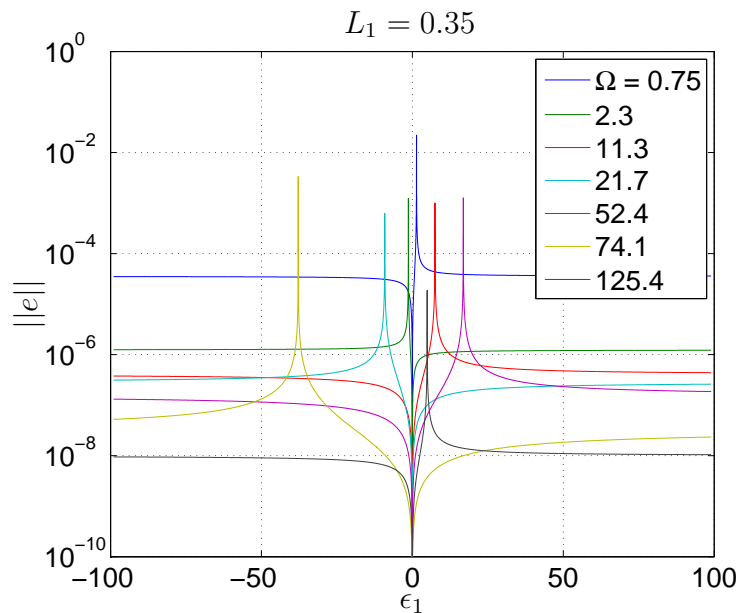


Figure 4.11: The error in the  $\epsilon_1$  domain of the elastic fixed-free bar with no other imposed error for multiple frequencies on a linear-log plot.

### $d_1$ Domain

Next, the error in the  $d_1$  domain is studied at specified frequencies. The frequencies were chosen to match those in the previous section. Fig. 4.12 shows the  $d_1$  domain. The error was only computed for each frequency from  $d_1 = 0$  to  $d_1 = \frac{2\pi}{\Omega}$  because the error is periodic with a period of  $\frac{2\pi}{\Omega}$ . Fig. 4.12 shows that whenever  $d_1$  is equal to an integer multiple of the period, the error tends to zero. This result is consistent with the results obtained from the frequency sweeps as well. The general results for the  $d_1$  domain are repeated for the  $d_2$  domain, and thus are not shown in this report. Also note, that in all of the above situations,

there is a general trend of decreasing error with increasing frequency, excluding near the resonant frequencies and the mini peaks described earlier.

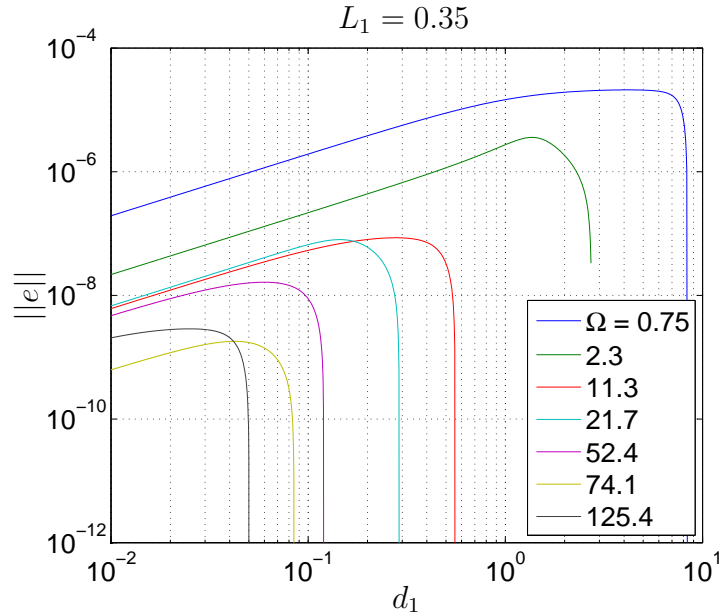


Figure 4.12: The error in the  $d_1$  domain of the elastic fixed-free bar with no other imposed error for multiple frequencies on a log-log plot.

### 4.1.2 Elastic Beam

Similar to the elastic fixed-free bar case, (2.41) and (2.42) need to be compared with (2.40), to determine that the system is behaving properly. Note, only the real part of each solution will be used for all of the following tests. See Appendix C for a table of all material constants and dimensions used for all of the following tests. Fig 4.13 shows both the reference system and the hybrid system, along with the difference between the two solutions for a hybrid system without error. As seen in Fig. 4.13, when there is no introduced error then the two systems are identical, which is to be expected. Now a 10% error is introduced into the displacement,  $\epsilon_1 = 0.1$ , to verify that the hybrid system is performing properly with an introduced error. Fig. 4.14 shows a discontinuity between the two sides of the gap and that a considerable amount of error has been introduced into the hybrid system due to the 10% displacement error, which is to be expected. Thus, the hybrid system is performing properly with introduced error. Similar equations defined for the bar case are used for the error analysis of the pinned-pinned beam case.

$$\|e_p\|^2 = \int_0^T \int_0^{L_1} \left( \text{Re}(\eta(y, \tau) - \hat{\eta}_p(y, \tau)) \right)^2 dy d\tau \quad (4.3a)$$

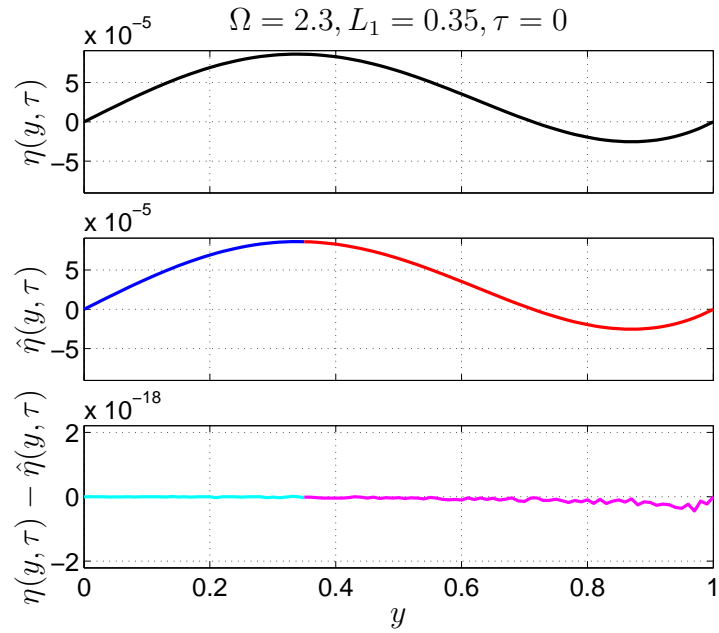


Figure 4.13: Comparison of the reference elastic pinned-pinned beam to the hybrid elastic pinned-pinned beam with no imposed error.

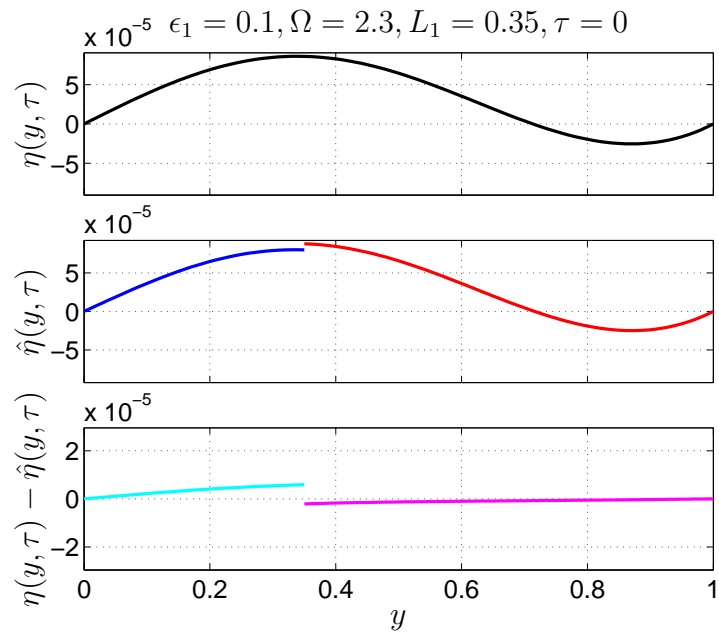


Figure 4.14: Comparison of the reference elastic pinned-pinned beam to the hybrid elastic pinned-pinned beam with  $\epsilon_1 = 0.1$ .

$$\|e_c\|^2 = \int_0^T \int_{L_1}^1 \left( \text{Re}(\eta(y, \tau) - \hat{\eta}_c(y, \tau)) \right)^2 dy d\tau \quad (4.3b)$$

$$\|e\| = \sqrt{\|e_p\|^2 + \|e_c\|^2} \quad (4.3c)$$

Where  $\eta(y, \tau)$ ,  $\hat{\eta}_p(y, \tau)$ , and  $\hat{\eta}_c(y, \tau)$  come from (2.40), (2.41), and (2.42) respectively. However, due to the complexity of solutions for the pinned-pinned beam case, an analytical solution for  $\|e\|$  is not determined, but rather the error is computed numerically. See Appendix B for the justification of using a numerical solution.

### Frequency Sweeps

The first parameter that is studied is the frequency,  $\Omega$ . For specific choices of the other parameters,  $\Omega$  is swept from  $10^{-1}$  to  $10^2$  to give a comprehensive look at the effect of the frequency of the hybrid system. Figures 4.15-4.18 show the error of the elastic pinned-pinned beam system with only one error parameter at a time. Note, that  $\epsilon_1$  and  $\epsilon_2$  have similar affects on the error, and thus only  $\epsilon_1$  are discussed, with all results applying to  $\epsilon_2$  as well. This is the same for  $\epsilon_3$  and  $\epsilon_4$ ,  $d_1$  and  $d_2$ , and  $d_3$  and  $d_4$ . Thus, only the parameters with  $k = 1, 3$  are used for analysis in this report. For every instance, the error grows extremely large at the resonant frequencies of the system, i.e.  $\Omega = 1, 4, 9, \dots$ , which is to be expected as the displacement becomes unbounded at those frequencies. In all cases, there are drops in the errors, similar to those of the elastic fixed-free bar. For parameters with  $k = 1, 2$ , these drops occur when  $\sin(\kappa L_1) = 0$ , and for parameters with  $k = 3, 4$ , these drops occur when  $\cos(\kappa L_1) = 0$ . Recall that  $\kappa = \pi\sqrt{\Omega}$ . These drops do not account for all of the drops in the curves with a  $d_k$  error. The extra drops in those curves are caused by  $d_k = \frac{2\pi n}{\Omega}$  for  $n = 1, 2, 3, \dots$ , or when  $d_k$  is an integer multiple of the period of the system. The physical reason for these drops is explained in the elastic fixed-free bar section. In Figs. 4.15 and 4.16, there are mini peaks that occur around the resonant frequencies. These mini peaks oscillate around the resonant frequencies as  $L_1$  changes. Also, the distance, in the frequency domain, of the mini peaks from the main peaks is directly related to the value of  $\epsilon_k$  for  $k = 1, 2, 3, 4$ . Next, a frequency sweep is performed with two error parameters to see how the errors add to one another, as shown in Figs. 4.19-4.22. Similar to the elastic fixed-free bar case, when  $\epsilon_1 = 0.1$  and  $\epsilon_3 = 0.1$ , the error drops and the mini peaks cancel out, as seen in Fig. 4.19. Fig. 4.20 has  $\epsilon_1 = 0.1$  and  $d_1 = 0.1$ . In this instance, the error drops associated with  $\sin(\kappa L_1) = 0$  are still present because both parameters individually had these drops. Also, the mini peaks associated with an  $\epsilon_1$  error are now gone, as well as the error drops from  $d_1$  equaling a integer multiple of the period. In Fig. 4.21,  $\epsilon_1 = 0.1$  and  $d_3 = 0.1$ , which also no longer has the error drops associated with the individual error parameters. However, remnants of the error drops associated with the  $d_3$  error at  $\cos(\kappa L_1) = 0$  are present. This indicates for equivalent values of the  $\epsilon_k$  and  $d_k$  in a system,  $d_k$  has a larger effect on the error. Finally, Fig. 4.22 shows the error with  $d_1 = 0.1$  and  $d_3 = 0.1$ . Again, the error drops due to  $\sin(\kappa L_1) = 0$  and  $\cos(\kappa L_1) = 0$  are no longer present. However, the error drop due

to  $d_k$  being equal to an integer multiple of the period is still present, only because  $d_1 = nd_3$  for  $n = 1, 2, 3, \dots$ . If that relation does not hold, then there will not be an error drop coming from  $d_k$  equaling an integer multiple of the period.

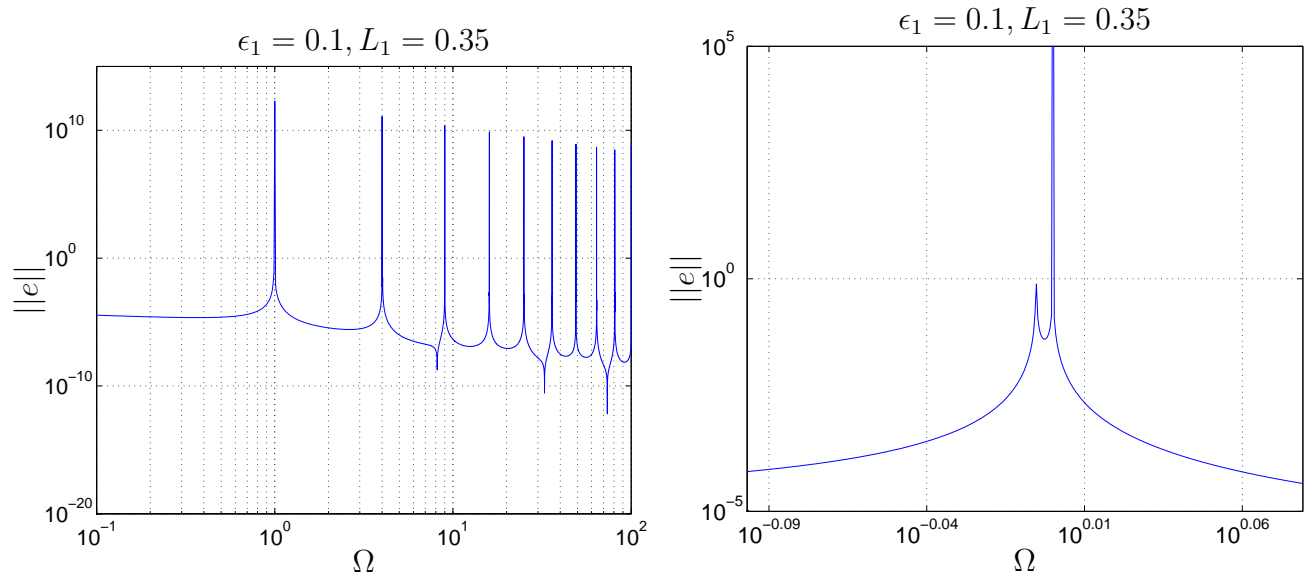


Figure 4.15: (a) A frequency sweep of the elastic pinned-pinned beam with  $\epsilon_1 = 0.1$  on a log-log plot. (b) A zoomed in plot showing the mini peak.

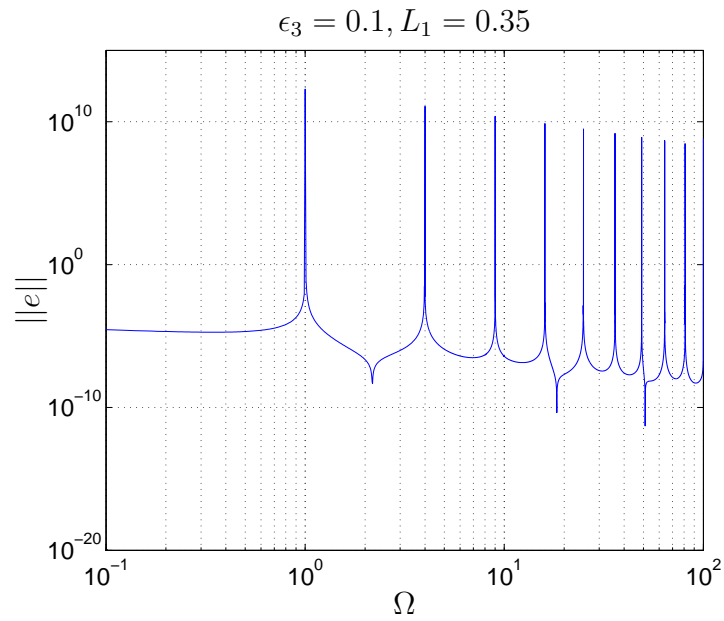


Figure 4.16: A frequency sweep of the elastic pinned-pinned beam with  $\epsilon_3 = 0.1$  on a log-log plot.

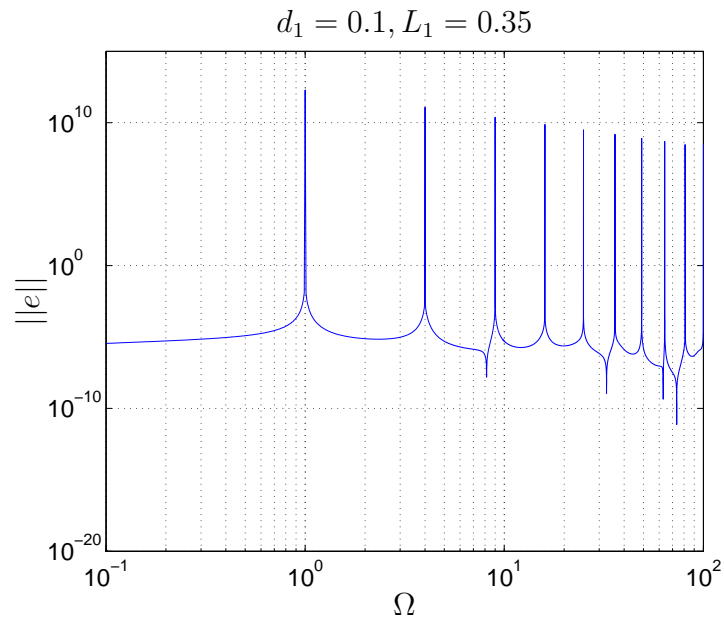


Figure 4.17: A frequency sweep of the elastic pinned-pinned beam with  $d_1 = 0.1$  on a log-log plot.

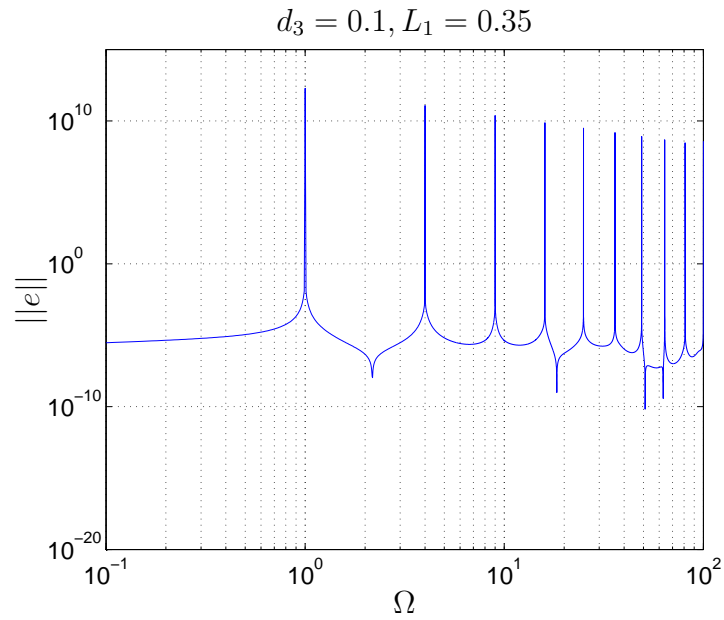


Figure 4.18: A frequency sweep of the elastic pinned-pinned beam with  $d_3 = 0.1$  on a log-log plot.

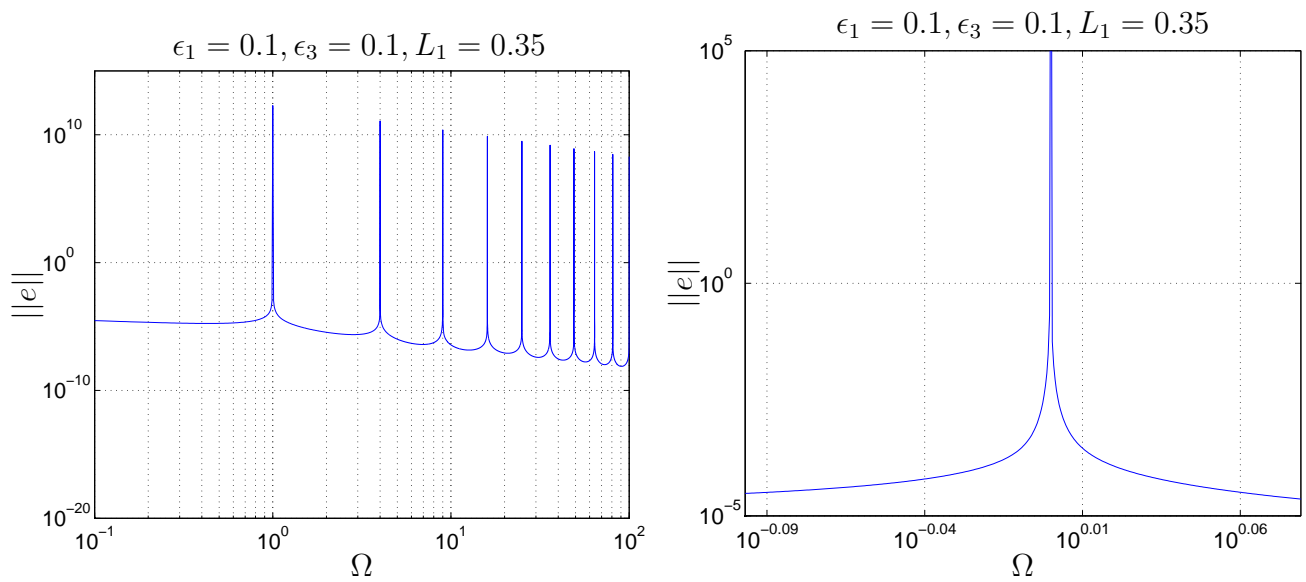


Figure 4.19: (a) A frequency sweep of the elastic pinned-pinned beam with  $\epsilon_1 = 0.1$  and  $\epsilon_3 = 0.1$  on a log-log plot. (b) A zoomed in plot missing the mini peak.

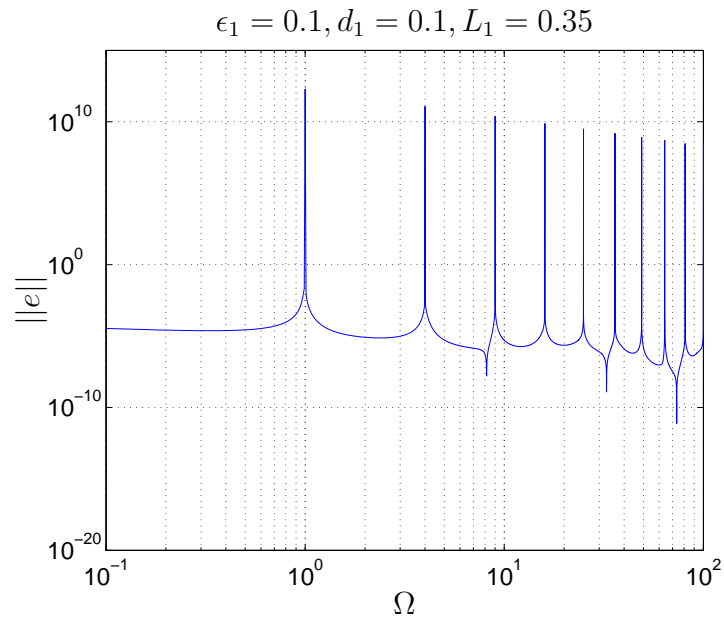


Figure 4.20: A frequency sweep of the elastic pinned-pinned beam with  $\epsilon_1 = 0.1$  and  $d_1 = 0.1$  on a log-log plot.

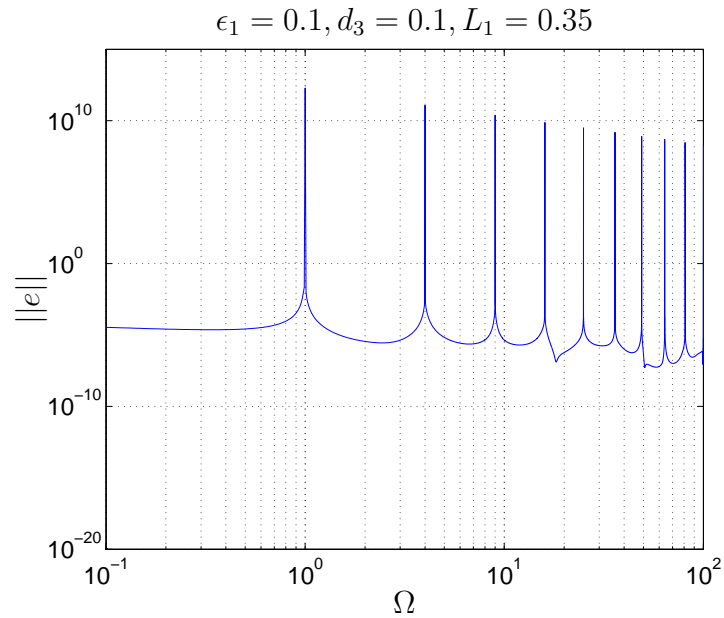


Figure 4.21: A frequency sweep of the elastic pinned-pinned beam with  $\epsilon_1 = 0.1$  and  $d_3 = 0.1$  on a log-log plot.

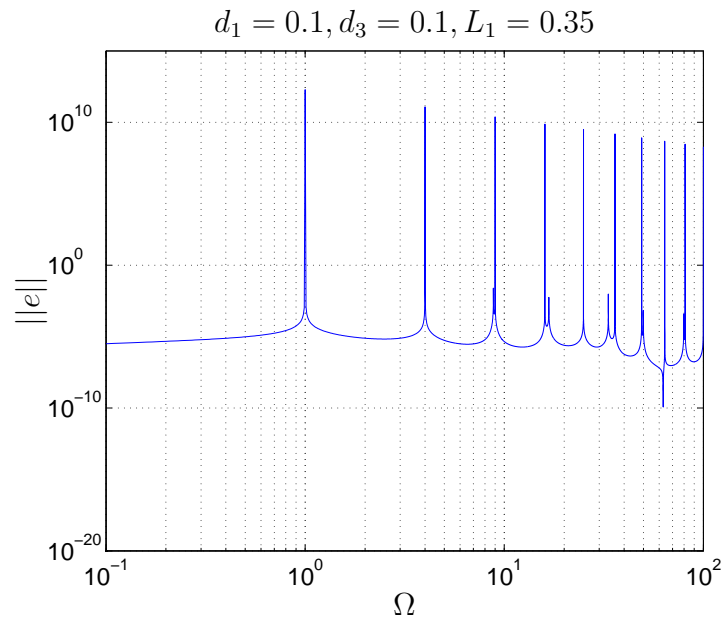


Figure 4.22: A frequency sweep of the elastic pinned-pinned beam with  $d_1 = 0.1$  and  $d_3 = 0.1$  on a log-log plot.

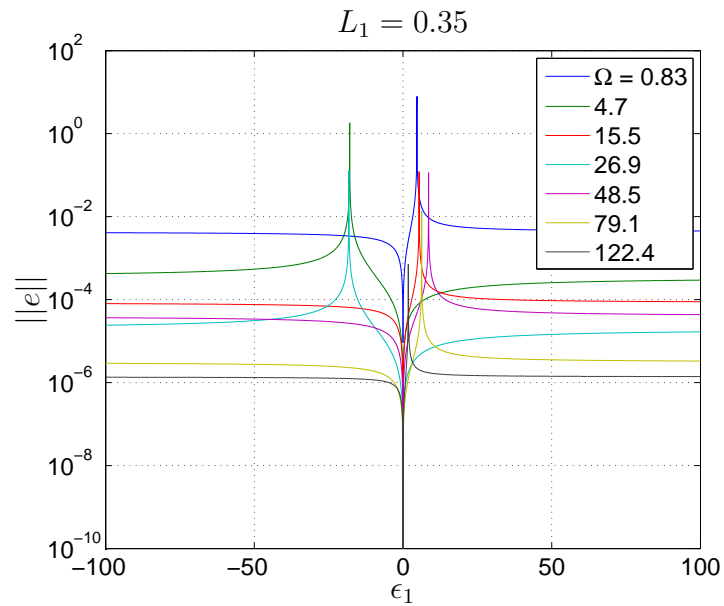


Figure 4.23: The error in the  $\epsilon_1$  domain of the elastic pinned-pinned beam with no other imposed error for multiple frequencies on a linear-log plot.

### $\epsilon_1$ Domain

Now, the error in the  $\epsilon_1$  domain is studied to see the effects of  $\epsilon_1$  on the error. The error is shown at multiple frequencies, which were chosen to give a comprehensive spectrum of frequencies. Figure 4.23 shows this  $\epsilon_1$  domain for multiple frequencies. As seen in Fig. 4.23, for every frequency, as  $\epsilon_1$  becomes large in magnitude, the error approaches a constant value. Thus the only areas of large change in the error come from locations near  $\epsilon_1 = 0$  or near the error peak in each curve. The error peak in each curve in the  $\epsilon_1$  domain is the cause of the mini peaks in the frequency domain. Finally, there is an error peak in every curve, thus no matter what the frequency is, there will be an error peak somewhere in the  $\epsilon_1$  domain, except when the frequency is a resonant frequency of the system. Note that in the  $\epsilon_2$ ,  $\epsilon_3$ , and  $\epsilon_4$  domains, all of the results are similar to those in Fig. 4.23, thus are not shown in this report.

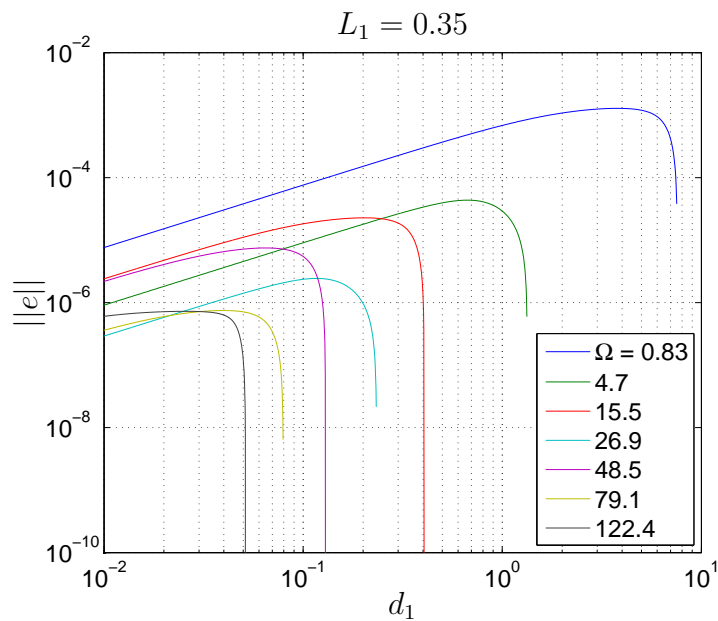


Figure 4.24: The error in the  $d_1$  domain of the elastic pinned-pinned beam with no other imposed error for multiple frequencies on a log-log plot.

### $d_1$ Domain

Finally, the error in the  $d_1$  domain is analyzed to see the effects of  $d_1$  on the error of the system. Since the effects of  $d_1$  are periodic, for each frequency  $d_1$  will only go from 0 to  $\frac{2\pi}{\Omega}$ . The frequencies chosen for the  $d_1$  domain were the same as those for the  $\epsilon_1$  domain. Fig. 4.24 shows the  $d_1$  domain for multiple frequencies. In all instances, the error grows from zero, peaks when  $d_1$  is half of the period, and then falls when  $d_1$  is equal to a period. Note that the  $d_2$ ,  $d_3$ , and  $d_4$  domains all produce similar results as those in Fig. 4.24, thus

are not shown in this report. Finally, in all of the above instances, there is a general trend of decreasing error with increasing frequency, except near the resonant frequencies and the mini peaks mentioned earlier. All of the results from the elastic pinned-pinned beam system are consistent with the results obtained for the elastic fixed-free bar system.

## 4.2 Analysis of the Viscoelastic Model

### 4.2.1 Viscoelastic Bar

In order for the viscoelastic fixed-free bar to be analyzed, the equations derived in Section 3.1 are verified for accuracy in the viscoelastic case. In order to do this, (3.9) is compared against (3.11) and (3.12) with no applied error, as shown in Fig. 4.25. It can be seen that

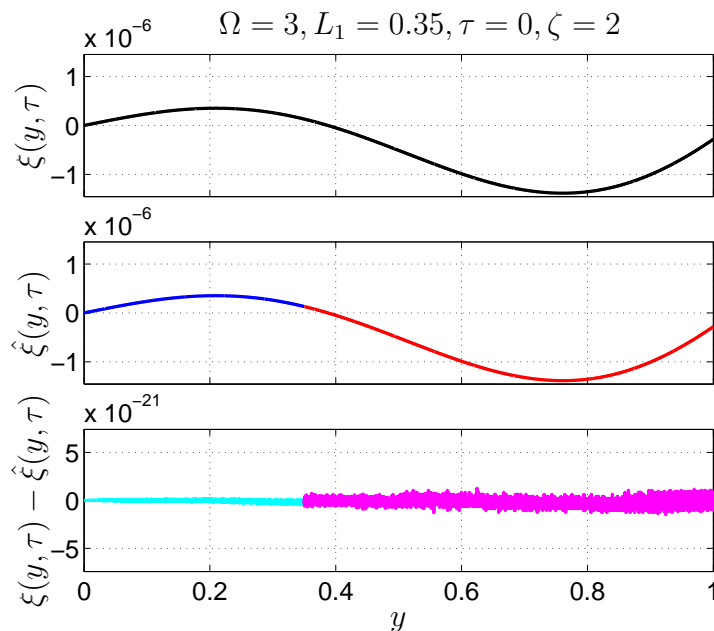


Figure 4.25: Comparison of the reference viscoelastic fixed-free bar to the hybrid viscoelastic fixed-free bar with no imposed error.

both solutions are nearly identical, the difference between them is a negligible computational error. Also, note that  $\Omega = 3$ , which is a resonant frequency of the elastic fixed-free bar system, thus the displacement should, in principle, become unbounded. However, in this instance, the displacement is bounded because  $\zeta = 2$ , which is near the value of  $\Omega$ , thus the system is damped, indicating that the equations are performing properly for no error. Now, an  $\epsilon_1 = 0.1$  error is applied, to check that the equations are performing properly with an applied error, as shown in Fig. 4.26. It can be seen that there is now a considerable amount of error between the two systems, which is the desired result. Also, note that there

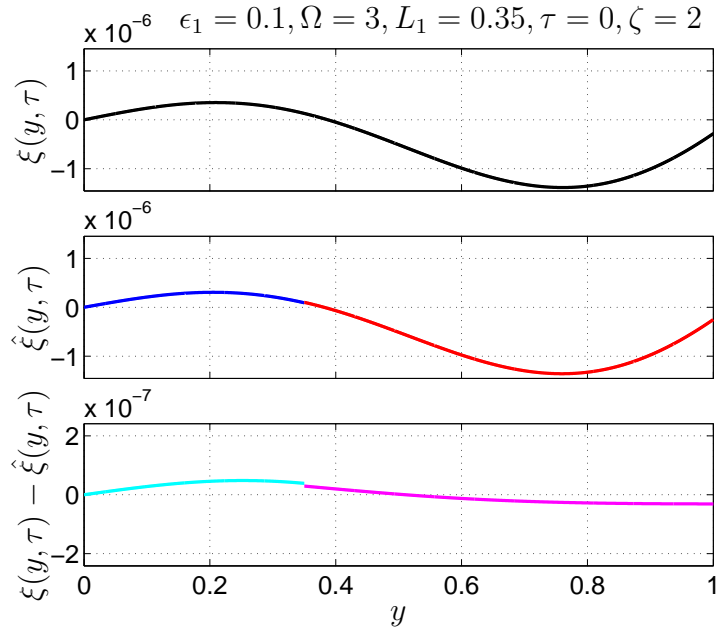


Figure 4.26: Comparison of the reference viscoelastic fixed-free bar to the hybrid viscoelastic fixed-free bar with  $\epsilon_1 = 0.1$ .

is no a discontinuity at the gap caused by  $\epsilon_1 = 0.1$ . Thus, the hybrid system equations are performing properly in the presence of applied error. In order to perform the error analysis, (4.1a), (4.1b), and (4.1c) are used, where  $\xi$ ,  $\hat{\xi}_p$ , and  $\hat{\xi}_c$  come from (3.9), (3.11), and (3.12) respectively. Unlike in the elastic fixed-free bar case, an analytical solution is not determined due to the complexity of the equations, but rather a numerical solution is used for the error. For a justification of using a numerical solution see Appendix B.

### Frequency Sweeps

First, a sweep of the frequency is performed from  $\Omega = 10^{-1}$  to  $\Omega = 10^2$ . This range gives a comprehensive look at the effect of the error parameters in the frequency domain. Figs. 4.27-4.30 show the frequency sweeps when only one error parameter is applied at a time for multiple values of  $\zeta$ . In all of of these instances, similar to the elastic case, there are drops in the error, which correspond to  $\sin(\kappa L_1) = 0$  for  $\epsilon_1$  and  $d_1$  and  $\cos(\kappa L_1) = 0$  for  $\epsilon_2$  and  $d_2$ . Again, in the figures with  $d_1$  and  $d_2$ , there are extra drops in error, corresponding to  $d_i$  equaling an integer multiple of the period. Unlike the elastic case, when the resonant frequencies are near the damping frequency,  $\zeta$ , the error does not become unbounded, but rather becomes finite. Also, when the damping frequency gets larger and the applied frequency gets larger, the error drops considerably, to almost negligible levels. Fig. 4.27 shows the frequency sweep for  $\epsilon_1 = 0.1$ . The mini peaks described in the elastic case are still present in this case, but is reduced due to the damping in the system. This result is the same for the

frequency sweep with  $\epsilon_2 = 0.1$ , as seen in Fig. 4.28. Figures 4.31-4.34 show frequency sweeps when two error parameters are applied. The results resemble those from the elastic case. The error drops or mini peaks that are present in both of the error parameters separately are also present when the error parameters are applied together, otherwise they are no longer present. Also, for equivalent values of  $\epsilon_k$  and  $d_k$ ,  $d_k$  has a larger effect on the shape of the error of the system. As can be seen in Figs. 4.27-4.34, when the applied frequency is near the damping frequency, the effects of all error parameters are canceled out by the damping, except for the effect of  $d_k$  equaling an integer multiple of the period.

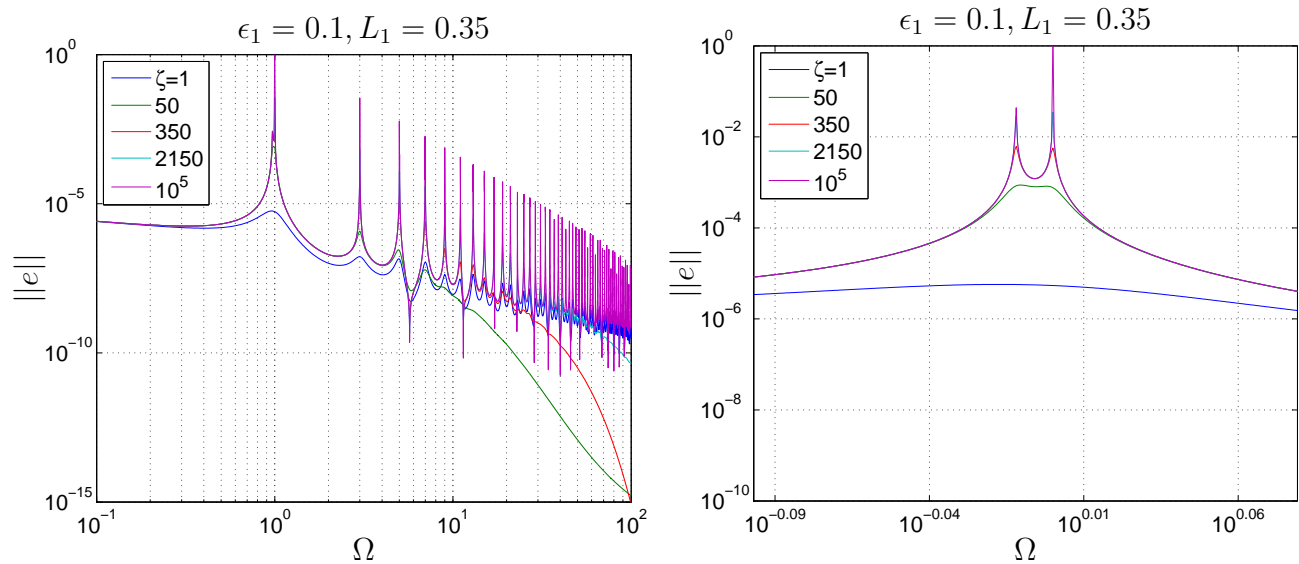


Figure 4.27: (a) A frequency sweep of the viscoelastic fixed-free bar with  $\epsilon_1 = 0.1$  on a log-log plot. (b) A zoomed in plot

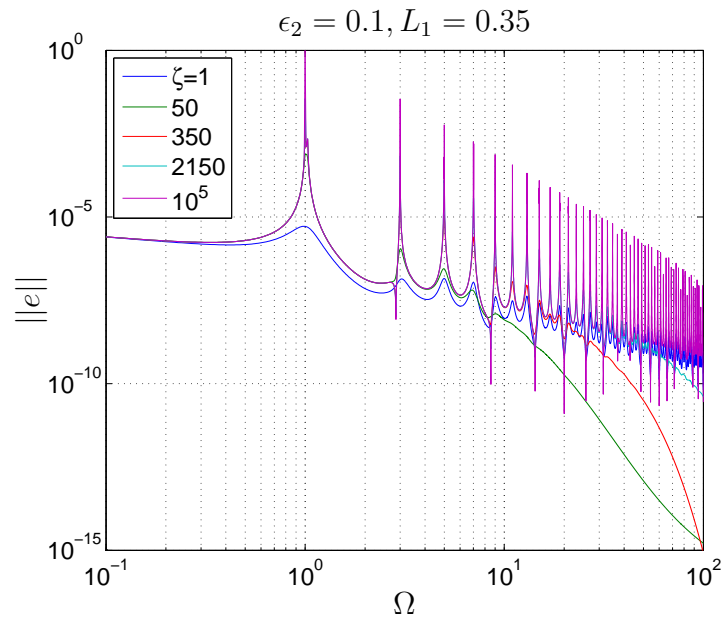


Figure 4.28: A frequency sweep of the viscoelastic fixed-free bar with  $\epsilon_2 = 0.1$  on a log-log plot.

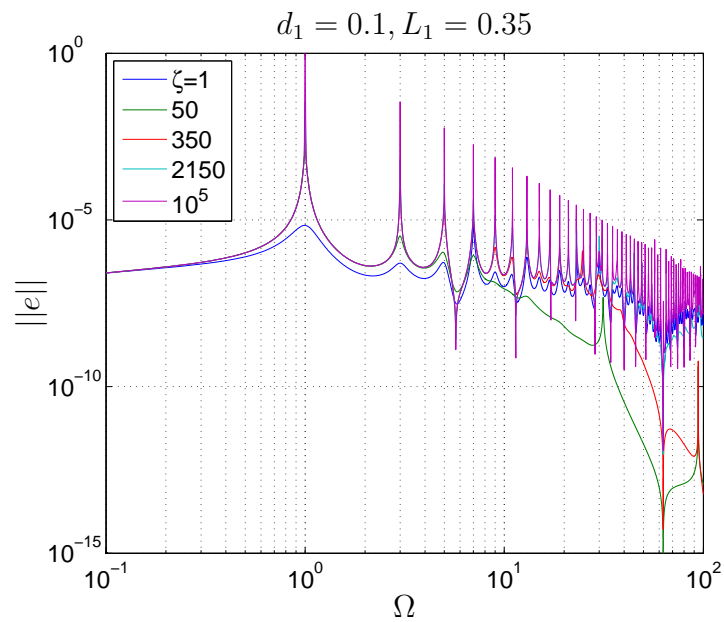


Figure 4.29: A frequency sweep of the viscoelastic fixed-free bar with  $d_1 = 0.1$  on a log-log plot.

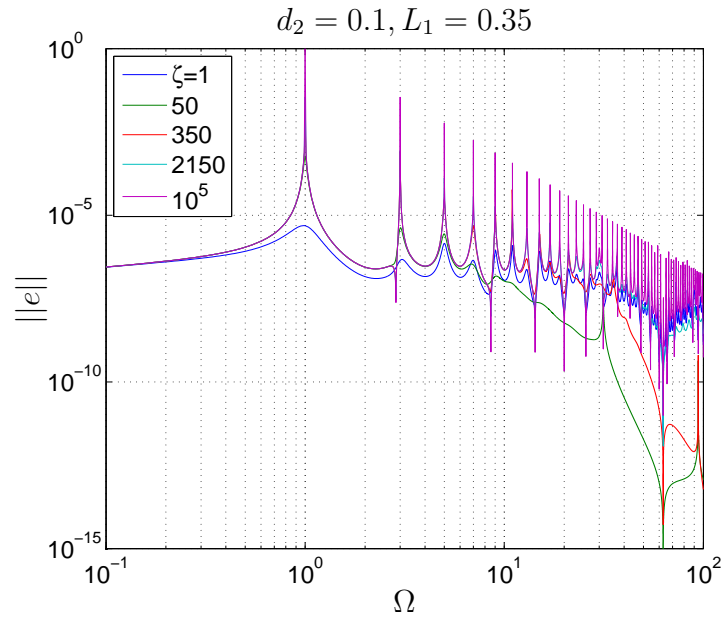


Figure 4.30: A frequency sweep of the viscoelastic fixed-free bar with  $d_2 = 0.1$  on a log-log plot.

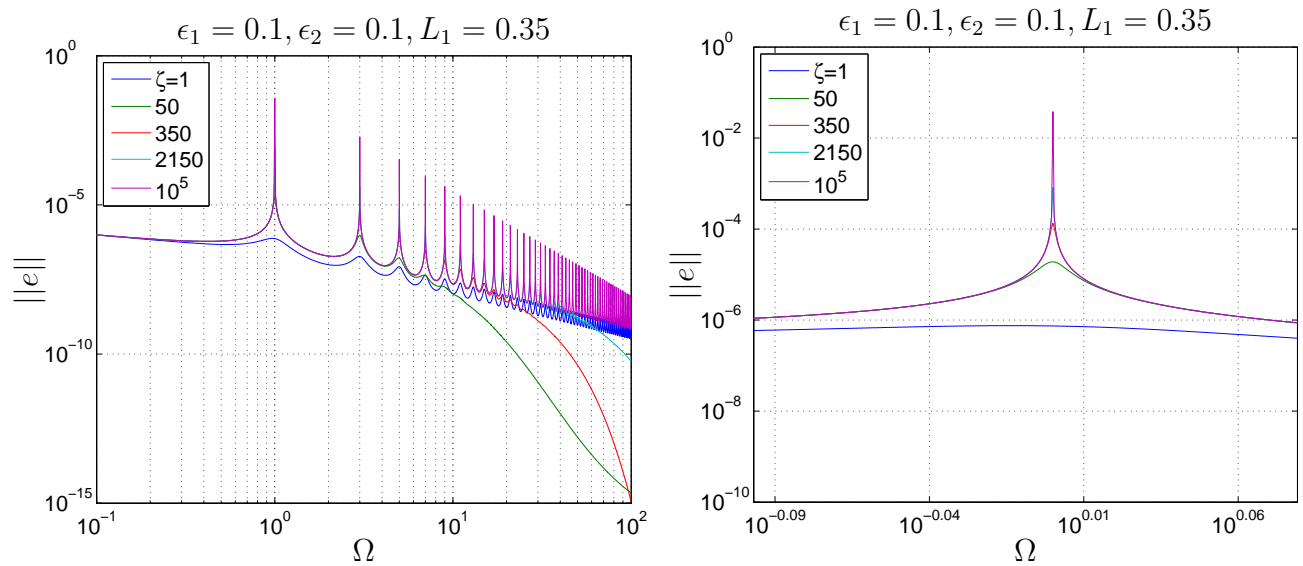


Figure 4.31: (a) A frequency sweep of the viscoelastic fixed-free bar with  $\epsilon_1 = 0.1$  and  $\epsilon_2 = 0.1$  on a log-log plot. (b) A zoomed in plot

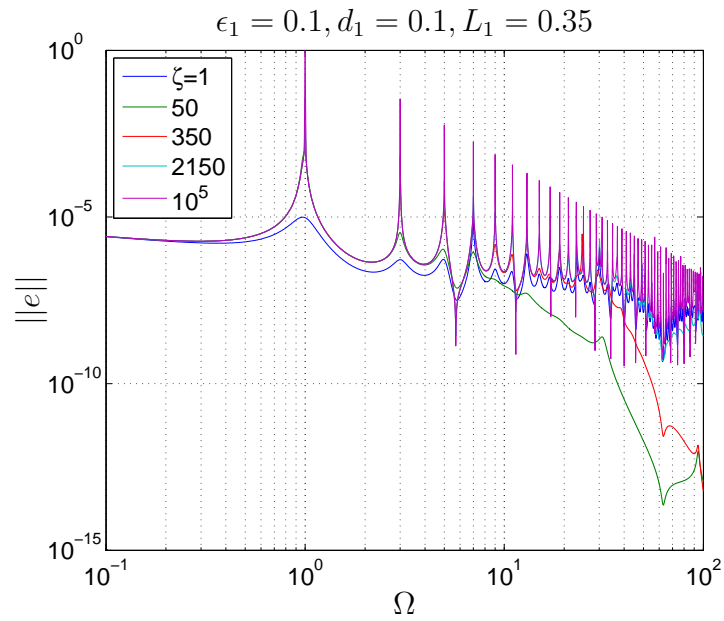


Figure 4.32: A frequency sweep of the viscoelastic fixed-free bar with  $\epsilon_1 = 0.1$  and  $d_1 = 0.1$  on a log-log plot.

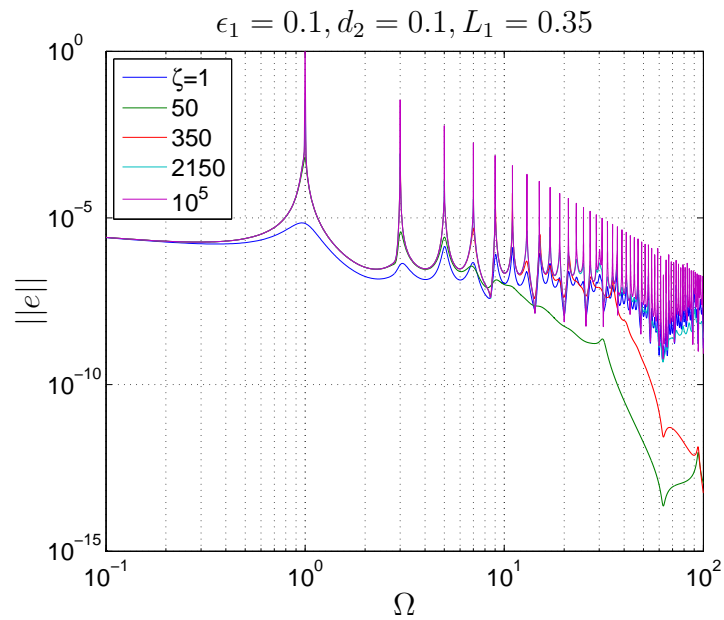


Figure 4.33: A frequency sweep of the viscoelastic fixed-free bar with  $\epsilon_1 = 0.1$  and  $d_2 = 0.1$  on a log-log plot.

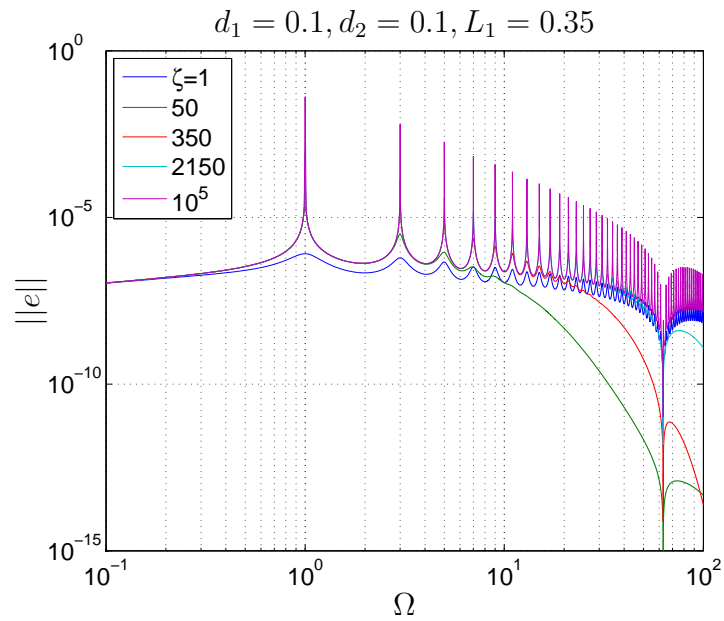


Figure 4.34: A frequency sweep of the viscoelastic fixed-free bar with  $d_1 = 0.1$  and  $d_2 = 0.1$  on a log-log plot.

### $\epsilon_1$ Domain

Next, the error in the  $\epsilon_1$  domain is analyzed to see how  $\epsilon_1$  affects the error. This is shown in Fig. 4.35 for multiple damping frequencies at  $\Omega = 74.1$ . Only one frequency was chosen because, as seen in the elastic case, the effect of frequency only moves the error peak around and gradually lowers the error for increasing frequency, thus the results would be similar for any applied frequency. As can be seen in Fig. 4.35, in every instance there is an error peak

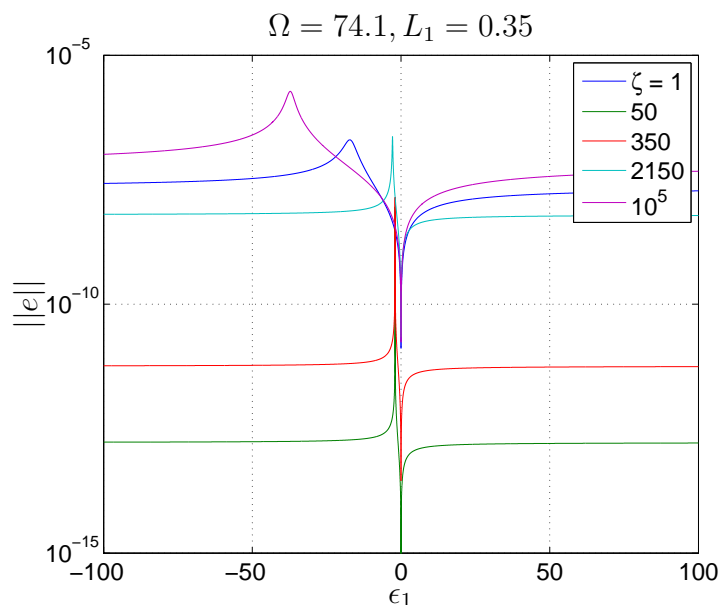


Figure 4.35: The error in the  $\epsilon_1$  domain of the viscoelastic fixed-free bar with  $\Omega = 74.1$  on a linear-log plot for multiple  $\zeta$  values.

in the  $\epsilon_1$  domain. However, when the applied frequency is far from the damping frequency, then the curve resembles that of the elastic case. Also, as the applied frequency nears the damping frequency, the error peak moves towards  $\epsilon_1 = -1$ . Thus, this implies that in the highly damped region, the only major changes in error are caused by  $\epsilon_1 = -1$ , or  $G_2 = 0$ , which means that there is no change in displacement on the  $\mathcal{C}$ -side of the gap, turning it into a fixed point. However, similar to the elastic case, as  $\epsilon_1$  grows in magnitude, the error in the system does not change very much, aside from the error peak and  $\epsilon_1 = 0$ . The  $\epsilon_2$  domain would produce similar results, thus are not shown in this report.

### $d_1$ Domain

Finally, the error in the  $d_1$  domain is studied for multiple damping frequencies, as shown in Fig. 4.36. For the same reasons described above, only one applied frequency was used for the  $d_1$  domain. The same frequency from the  $\epsilon_1$  domain is used for the  $d_1$  domain just for consistency. As can be seen in Fig. 4.36, in every instance the error drops when  $d_1$  equals the

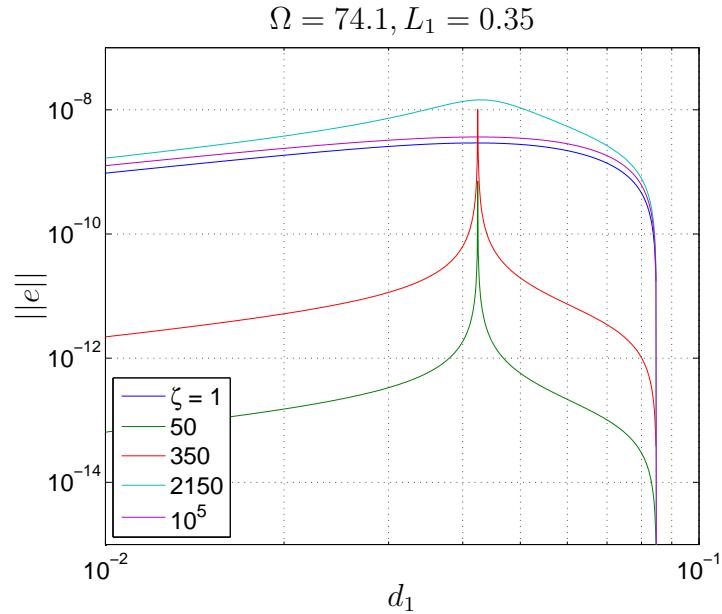


Figure 4.36: The error in the  $d_1$  domain of the viscoelastic fixed-free bar with  $\Omega = 74.1$  on a log-log plot for multiple  $\zeta$  values.

period of the specific applied frequency, just like in the elastic case. For damping frequencies far from the applied frequency, the curves resemble those of the elastic case. However, for damping frequencies closer to the applied frequency, the error drops down, but develops an error peak. This peak occurs when  $d_1$  equals half of the period. The general results for the  $d_1$  domain are repeated for the  $d_2$  domain, and thus are not shown in this report.

### 4.2.2 Viscoelastic Beam

First, the equations for the hybrid solution to the viscoelastic beam, (3.20) and (3.21), are compared with the equation for the solution to the reference viscoelastic beam, (3.18), when there is no error in the hybrid system. This comparison is shown in Fig. 4.37. As with all of the previous cases, only the real part of the equations will be considered for the following tests. For a list of material constants and dimensions of the beam used in this section, see Appendix C. As it can be seen, there is only round-off error between the hybrid and reference systems, which is desired for this instance. Secondly, the viscoelasticity is tested, which is also shown in Fig. 4.37. In this instance, the applied frequency chosen was  $\Omega = 4$ , which is a resonant frequency of the system, meaning that the displacement would become extremely large in the elastic case. However, in Fig. 4.37, the displacement is bounded to normal values for this system, meaning that viscoelasticity is working properly. Note that  $\zeta = 2$ , meaning the the damping peak is at a frequency of 2, which is close to the applied frequency. If  $\zeta$  was chosen to be much farther from the applied frequency, the effects of the damping would be less.

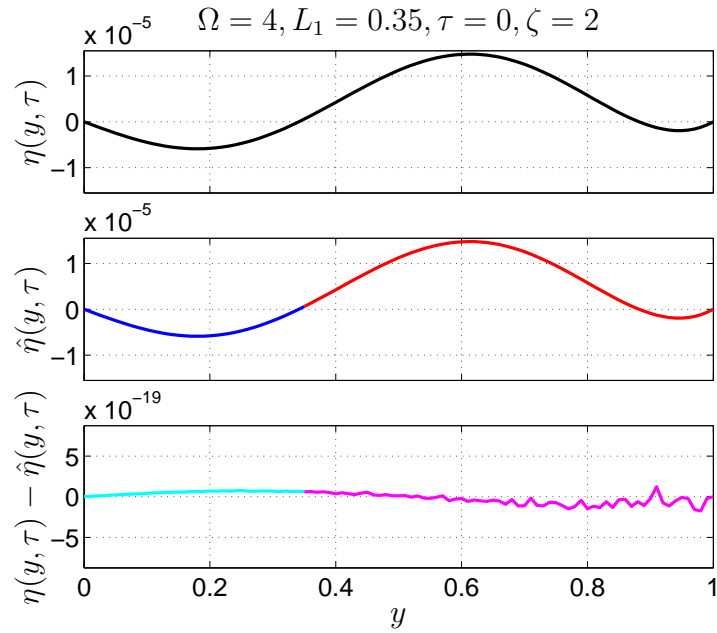


Figure 4.37: Comparison of the reference viscoelastic pinned-pinned beam to the hybrid viscoelastic pinned-pinned beam with no imposed error.

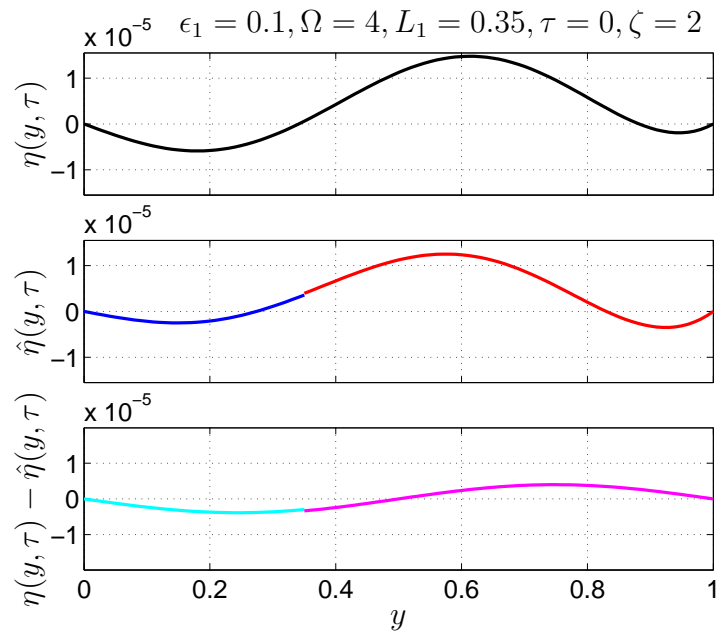


Figure 4.38: Comparison of the reference viscoelastic pinned-pinned beam to the hybrid viscoelastic pinned-pinned beam with  $\epsilon_1 = 0.1$ .

Now, the effects of the error parameters are tested to make sure that they are working properly in the viscoelastic beam case. Fig. 4.38 shows the comparison between the reference system and the hybrid system with  $\epsilon_1 = 0.1$  applied to the hybrid system. It can be seen that with the applied error, there is now a discontinuity at the gap and the error between the two systems is no longer round-off error, but rather hybrid system error, which is to be expected. Thus all of the equations are working properly for the viscoelastic beam case. In order to compute the error of the system, (4.3a), (4.3b), and (4.3c) are employed. Due to the complexity of these equations, an analytical solution is not determined, but rather a numerical solution is computed. For a justification of a computational solution, see Appendix B.

### Frequency Sweeps

In order to study the effects of the error parameters, a sweep of the frequency is performed from  $\Omega = 10^{-1}$  to  $\Omega = 10^2$ . In each instance, only one error parameter is applied at a time to see the effect of that parameter. However, it is noted that the effects of  $\epsilon_1$  and  $\epsilon_2$  are nearly identical, and thus only  $\epsilon_1$  will be considered. This is the same for  $d_1$  and  $d_2$ ,  $\epsilon_3$  and  $\epsilon_4$ , and  $d_3$  and  $d_4$ , thus only the parameters with  $k = 1, 3$  will be considered in this report. Figs. 4.39-4.42 show the frequency sweep for the individual error parameters. In all instances, there are drops in the error that occur at same location in the frequency domain, regardless of the  $\zeta$  value. These drops occur when  $\sin(\kappa L_1) = 0$  for error parameters with  $k = 1, 2$ , and when  $\cos(\kappa L_1) = 0$  for error parameters with  $k = 3, 4$ . Recall that  $\kappa = \pi\sqrt{\Omega}\exp(i\delta)$ . However, these drops in error are not the only drops in error for the curves with a  $d_k$  error. These extra error drops occur when  $d_k$  equals an integer multiple of the period. It can also be seen that when the applied frequency is near the damping frequency the error is reduced around the resonant frequencies and does not become large, as in the elastic case. Also, when the applied frequency is far from the damping frequency the error curves resemble those seen in the elastic beam case. In the Figs. 4.39 and 4.40 there are mini peaks around the resonant frequency peaks, similar to those described for the elastic beam case. These mini peaks oscillate around the resonant frequency peaks as  $L_1$  grows from zero to one. And the magnitude, in terms of distance from the resonant frequency peak, is a function of to the value of  $\epsilon_k$ . All of this indicates that both the error parameters and the gap location,  $L_1$ , are extremely important to the error in the hybrid system. Now, in order to see how the error parameters effect each other, two error parameters will be applied at a time, shown in Figs. 4.43-4.46. Figure 4.43 shows the error for  $\epsilon_1 = 0.1$  and  $\epsilon_3 = 0.1$ . In this instance, all of the error drops associated with the individual parameters are now gone. Also, the mini peaks described earlier have also vanished. Figure 4.44 has  $\epsilon_1 = 0.1$  and  $d_1 = 0.1$ , and in this instance, the error drops associated with  $\sin(\kappa L_1) = 0$  are still present because they are present in the two parameters individually. However, in the curves with  $\zeta = 50$  and  $\zeta = 350$  traces of the error drop due to  $d_1$  being an integer multiple of the period is noticeable. Since  $d_1 = 0.1$ , the error drop occurs when  $\Omega = 62.8$ , or  $\Omega = \frac{2\pi}{.1}$ , which is close to  $\zeta = 50$  and relatively close to  $\zeta = 350$ , but far from the other  $\zeta$  values. This indicates that when the

applied frequency is near the damping frequency, the effects of  $\epsilon_1$  are reduced and the effects of  $d_1$  take a larger role. In Fig. 4.45, again the error drops due to  $\sin(\kappa L_1) = 0$  are completely gone. However, remnants of the error drops due to  $\cos(\kappa L_1) = 0$  are still visible, indicating that  $d_3$  has a large effect on the error than  $\epsilon_1$  for equal values of the parameters. Also, in the curves with  $\zeta = 50$  and  $\zeta = 350$ , the error drop due to  $d_3 = \frac{2\pi}{\Omega}$  is noticeable, when it is not noticeable in the other curves. This confirms the result from Fig. 4.44 that when the applied frequency is close to the damping frequency, then the effects of  $\epsilon_k$  are diminished, and the effects of  $d_k$  take on a larger role. In Fig. 4.46, the error drops due to  $\sin(\kappa L_1) = 0$  and  $\cos(\kappa L_1) = 0$  are both gone, meaning that all  $d_k$  have an equal effect on the error and one can cancel out the error drop due to another. The error drop due to the time-delay being equal to a period of the system is still present, which is expected since it's present for each of the individual parameters. However, this is only true when  $d_1 = nd_3$  for  $n = 1, 2, 3, \dots$ , otherwise those error drops will not be present. As can be seen in Figs. 4.39-4.46, when the applied frequency is near the damping frequency, the effects of all error parameters are canceled out by the damping, except for the effect of  $d_k$  equaling an integer multiple of the period.

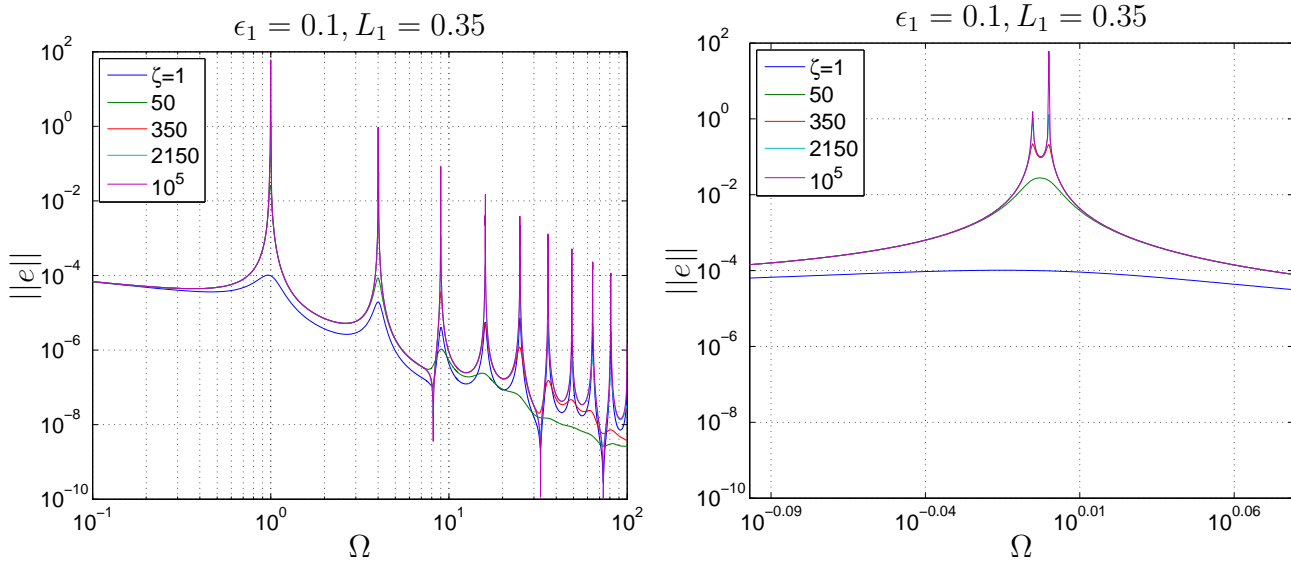


Figure 4.39: (a) A frequency sweep of the viscoelastic pinned-pinned beam with  $\epsilon_1 = 0.1$  on a log-log plot for multiple  $\zeta$  values. (b) A zoomed in plot showing the mini peak.

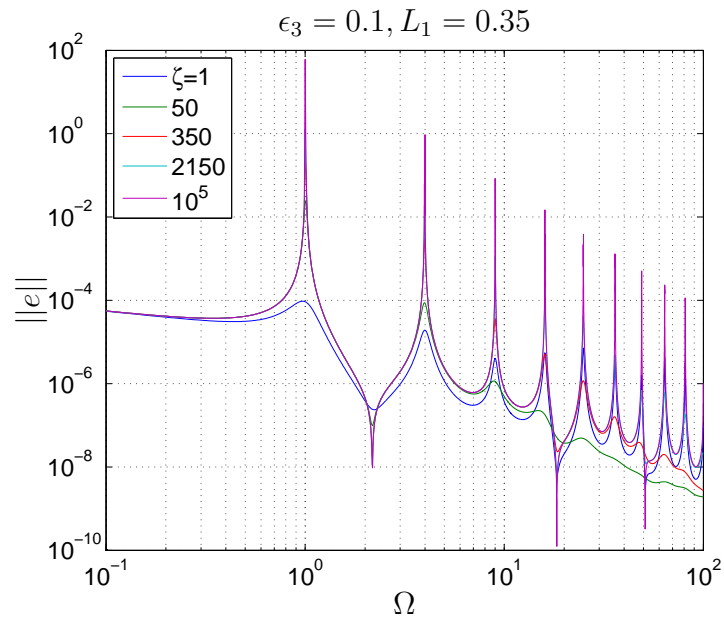


Figure 4.40: A frequency sweep of the viscoelastic pinned-pinned beam with  $\epsilon_3 = 0.1$  on a log-log plot for multiple  $\zeta$  values.

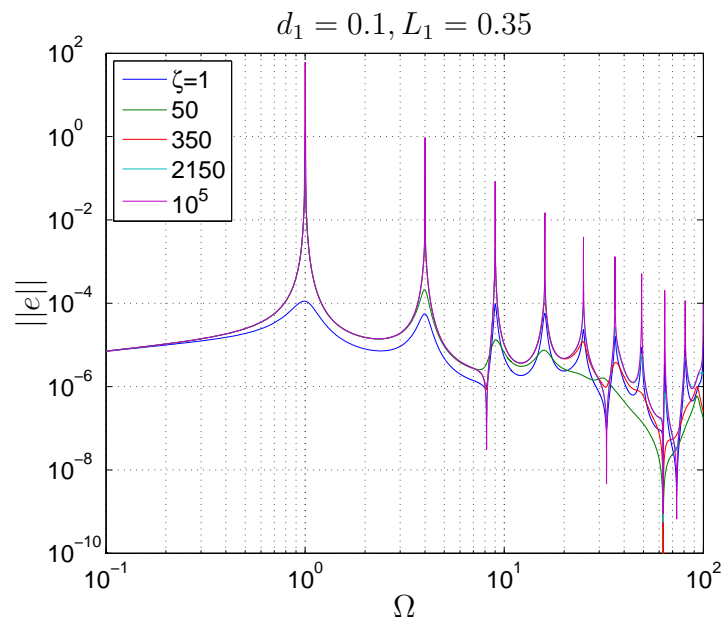


Figure 4.41: A frequency sweep of the viscoelastic pinned-pinned beam with  $d_1 = 0.1$  on a log-log plot for multiple  $\zeta$  values.

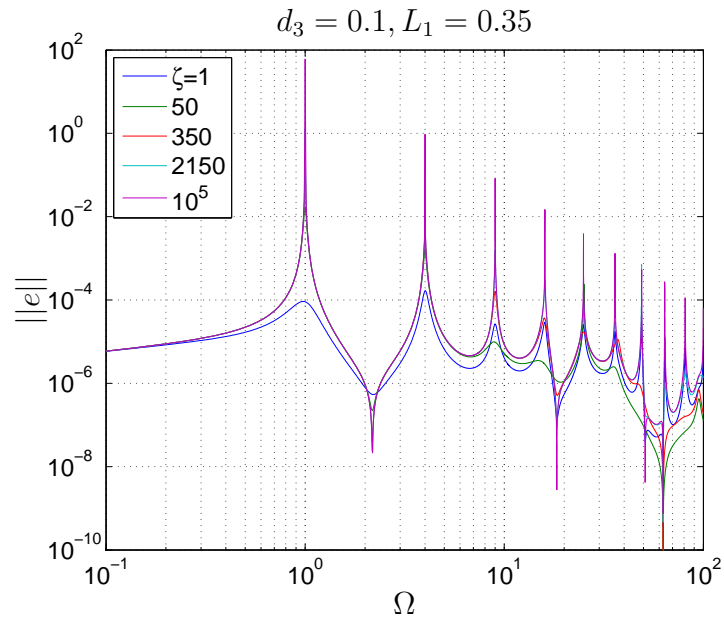


Figure 4.42: A frequency sweep of the viscoelastic pinned-pinned beam with  $d_3 = 0.1$  on a log-log plot for multiple  $\zeta$  values.

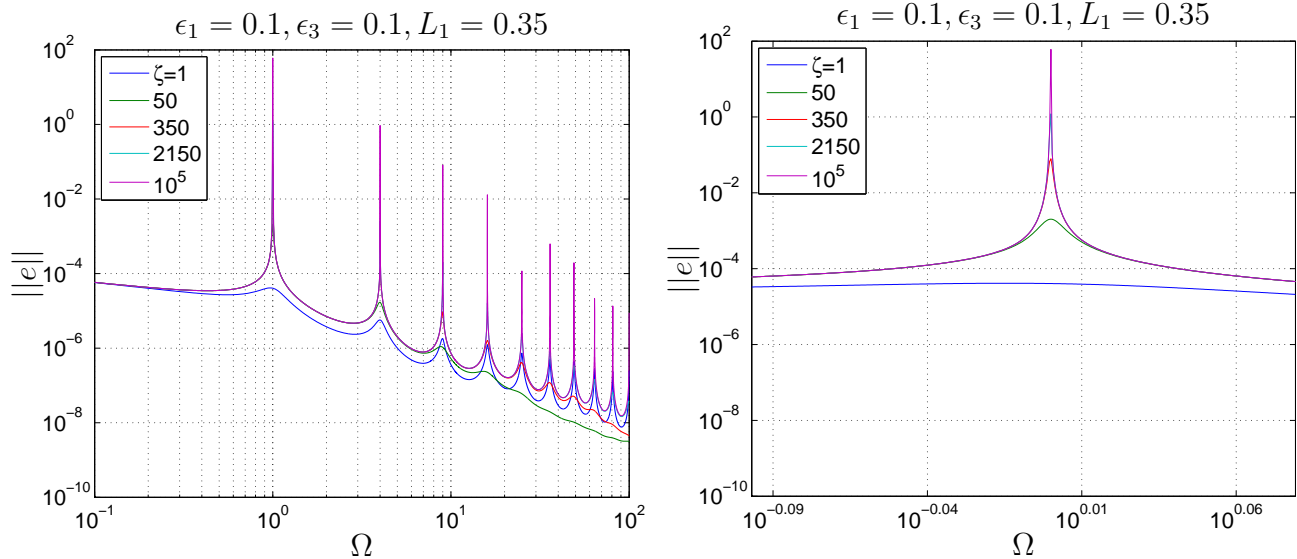


Figure 4.43: (a) A frequency sweep of the viscoelastic pinned-pinned beam with  $\epsilon_1 = 0.1$  and  $\epsilon_3 = 0.1$  on a log-log plot for multiple  $\zeta$  values. (b) A zoomed in plot showing the mini peak.

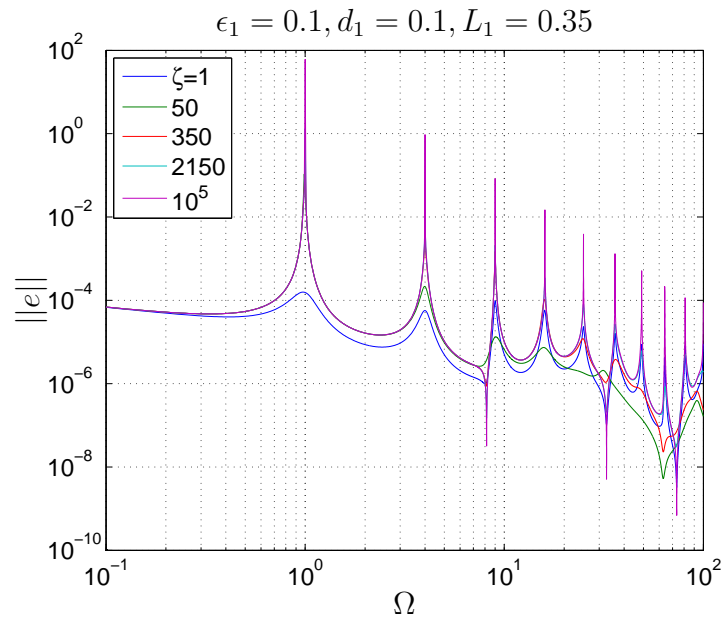


Figure 4.44: A frequency sweep of the viscoelastic pinned-pinned beam with  $\epsilon_1 = 0.1$  and  $d_1 = 0.1$  on a log-log plot for multiple  $\zeta$  values.

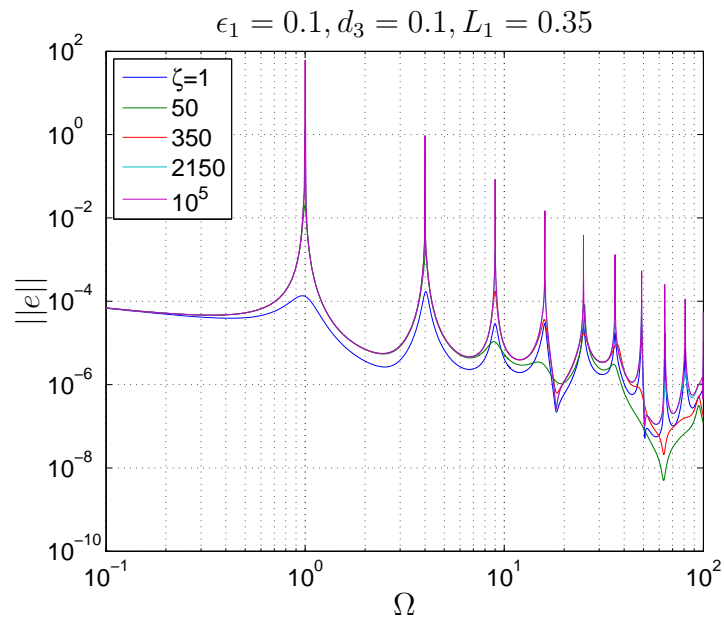


Figure 4.45: A frequency sweep of the viscoelastic pinned-pinned beam with  $\epsilon_1 = 0.1$  and  $d_3 = 0.1$  on a log-log plot for multiple  $\zeta$  values.

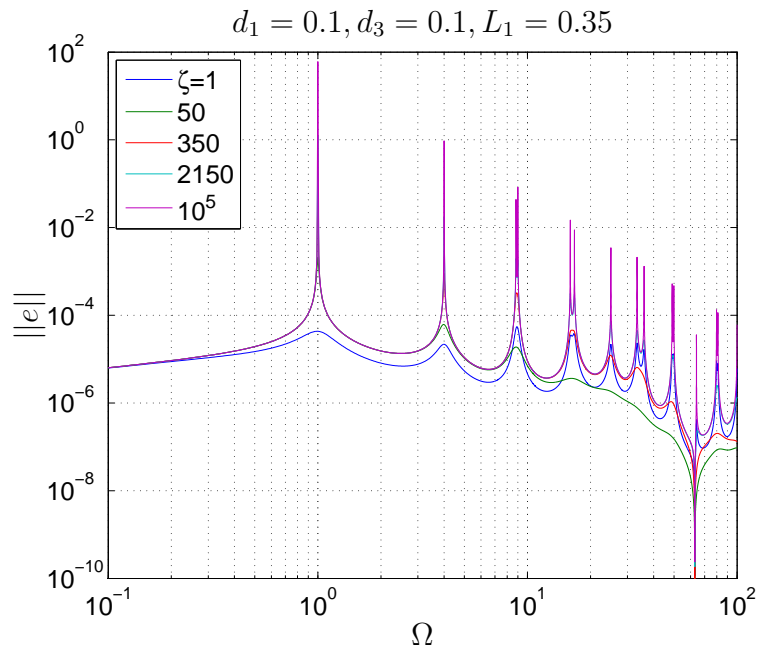


Figure 4.46: A frequency sweep of the viscoelastic pinned-pinned beam with  $d_1 = 0.1$  and  $d_3 = 0.1$  on a log-log plot for multiple  $\zeta$  values.

### $\epsilon_1$ Domain

Next, the error in the  $\epsilon_1$  domain is analyzed, shown in Fig. 4.47. In the  $\epsilon_1$  domain, the error is computed for one frequency choice,  $\Omega = 79.1$ , and multiple  $\zeta$  values. In each case, there are peaks in the error, however, these peaks move in the  $\epsilon_1$  domain when the  $\zeta$  value changes and, just like the viscoelastic fixed-free bar, as the damping frequency approaches the applied frequency, the peak approaches  $\epsilon_1 = -1$ . This has the same implications as those described for the viscoelastic fixed-free bar. Also, when the damping frequency is

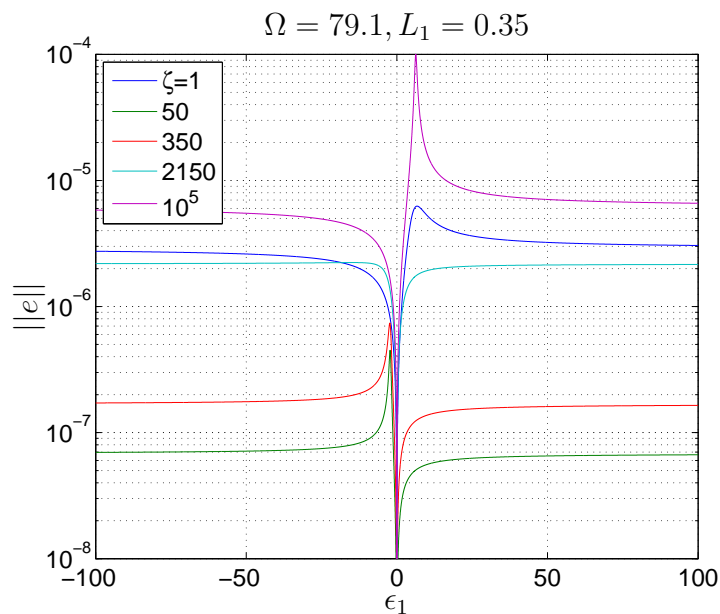


Figure 4.47: The error in the  $\epsilon_1$  domain of the viscoelastic pinned-pinned beam with  $\Omega = 79.1$  on a linear-log plot for multiple  $\zeta$  values.

closest to the applied frequency, on a log scale, the average error over the  $\epsilon_1$  domain drops considerably, but is much higher for farther damping frequencies. Also, as in the elastic case, as  $\epsilon_1$  becomes large in magnitude, the error levels off and seems to approach an asymptote. The general results seen for the  $\epsilon_1$  domain are repeated for the domains of  $\epsilon_2$ ,  $\epsilon_3$ , and  $\epsilon_4$ , and thus are not shown in this report.

### $d_1$ Domain

Finally, the error in the  $d_1$  domain is studied, as shown in Fig. 4.48. Since the effects of  $d_1$  are periodic with the frequency, only one period will be shown, with  $d_1$  going from 0 to  $\frac{2\pi}{\Omega}$ . In this instance  $\Omega = 79.1$ , which was chosen to match the frequency used for the  $\epsilon_1$  domain. As seen in Fig. 4.48, when the applied frequency is far from the damping frequency, on a log scale, the curves behave similar to that of the elastic case, see Fig. 4.24. However, when the damping frequency is close to the applied frequency, the error drops to a lower average value

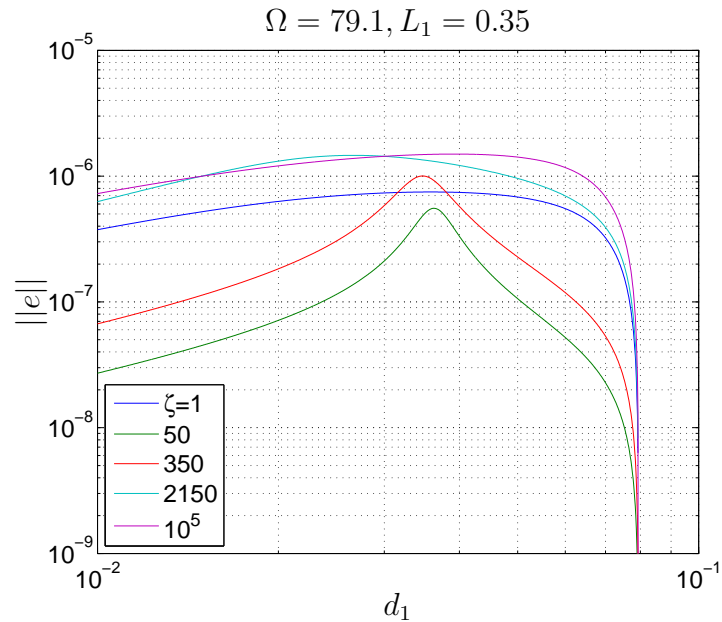


Figure 4.48: The error in the  $d_1$  domain of the viscoelastic pinned-pinned beam with  $\Omega = 79.1$  on a log-log plot for multiple  $\zeta$  values.

over the domain of  $d_1$ , except a specific value of  $d_1$  where the error grows to a value similar to the other curves. The general results from the  $d_1$  domain are repeated for  $d_2$ ,  $d_3$ , and  $d_4$  domains, thus they are not shown in this report. Note, that in all cases, there is a general decay in the error as the frequency increases, indicating that at very high frequencies, the error in the hybrid system will be small, except near the resonant frequencies and the mini peaks, just like the elastic case. However, when the applied frequency is near the damping frequency,  $\zeta$ , then the error will never grow without bound, even at the resonant frequencies, which differs from the elastic case. In all cases, when the applied frequency is far from the the damping frequency, then the error curves behave in the same manner as the elastic case. This is to be expected, because away from the damping frequency the viscoelastic equations approach the elastic equations.

# Chapter 5

## Conclusion

The analysis in Chapter 4 of the four cases studied in this report, the elastic fixed-free bar, the elastic pinned-pinned beam, the viscoelastic fixed-free bar, and the viscoelastic pinned-pinned beam, demonstrates the theoretical performance of those cases. Note, that in all of the above situations, it was assumed that a harmonic excitation was applied and only the steady-state solution was relevant. This ignores any transient response that may occur in experimental implementations of hybrid simulation.

### 5.1 Summary of Results

The results show, that even for the four different cases, the errors are extremely similar. The resonant frequencies have a large impact on the error of the system, in all cases, except when the resonant frequencies are near the damping frequency. Thus, in order for hybrid simulation to be effective as a simulation technique, one must be aware of the forcing frequency, as this could potentially lead to large errors. And typically, the forcing frequency is not just a single frequency, but rather distribution of frequencies, such as an earthquake. This makes it more likely that the resonant frequencies are going to be in that distribution of frequencies, meaning that special care must be taken when applying those distributions of frequencies. However, in all instances, there are error drops that occur, such as those due to  $\sin(\kappa L_1) = 0$  or  $\cos(\kappa L_1) = 0$  for the specific error parameters. This implies that one could possibly use these error drops to give more accurate results from hybrid simulation if the error drops were placed at frequencies that are more common in the forcing distribution. Also, if the main distribution of forcing frequencies is near the damping frequency,  $\zeta$ , then the error no longer has any spikes or drops. In the earlier analysis for the viscoelastic cases,  $\zeta$  was used as a parameter that could be controlled, however,  $\zeta$  is a material constant, and would not usually be controllable, other than switching materials. In all cases the error due to  $\epsilon_k$  seems to approach an asymptotic limit, as seen by the  $\epsilon_1$  domain figures. Also, the error reaches those limits quickly in the  $\epsilon_k$  domain, thus it would be impractical to try and reduce the  $\epsilon_k$  parameters to reduce the error in the system because unless one could make

the  $\epsilon_k$  value very small, the system error is not going to change much. However, this assumes that the value of  $\epsilon_k$  is not at one of the peaks that occur in the  $\epsilon_k$  domain. These results were corroborated with hybrid formulations of a classical elastic Kirchhoff-Love plate with dynamic bending by the work of Bakhaty [2]. This shows that there are universal errors that begin to occur for hybrid simulation, even for simple one-dimensional and two-dimensional problems. However, an understanding of the causes of these errors will allow for hybrid simulations to be conducted in a way that will reduce and prevent these errors.

## 5.2 Potential Future Research in the Field of Hybrid Simulation Theory

In this report it was assumed that  $\epsilon_k$  and  $d_k$  were constants. However, this is not always the case, they may in fact be functions of the frequency, such that at higher frequencies the time-delay or magnitude error may increase. Thus, to include this, one could use the following equation for the error parameters [2]:

$$d_k = \frac{d_0}{\left(1 + \exp(\Omega_0 - \Omega)\right)^2}. \quad (5.1)$$

Where  $d_0$  is the maximum time delay and  $\Omega_0$  is the frequency of maximum growth rate. A similar equation can be applied to  $\epsilon_k$ . This will provide a different look to the error curves of the frequency sweeps. However, this is just one possible function for the error parameters.

Also, this report assumed a single homogeneous linear material that could be modeled by (2.2) and (2.23). This is not always the case of an experimental setup of hybrid simulation. For example, many hybrid simulation setups are for many bars and beams at the same time, each interacting with the whole system [14]. Also, the specific material used for all examples was that of a generic steel, see Appendix C, just because steel is a good generic material that is used in multiple situations. However, hybrid simulation is not limited to steel, but can also be applied to other materials, such as polymers, that have completely different governing equations and would react differently to a hybrid simulation setup.

This report focused on the  $L_2$  norm of the displacement, but that only shows one part of error in the system. The error in the force, rotation, shear, and moment can also be studied with the use of seminorms on the spatial derivatives of the displacement [12]. Understanding the error in these quantities is just as important as understanding the error in the displacement because in some situations these quantities can be of more importance to the workings of a system than the displacement.

Hybrid simulation has a strong background in the experimental community, but is lacking in theoretical support. This report is designed to show both the theoretical flaws and benefits of hybrid simulation, allowing for a better understanding of hybrid simulation. Hopefully, this report strengthened the theoretical development of hybrid simulation, and leads to further theoretical tests of different and more complicated systems.

# Bibliography

- [1] M. Ahmadizadeh, G. Mosqueda, and A. M Reinhorn. “Compensation of actuator delay and dynamics for real time hybrid structural simulation”. In: *Earthquake Engineering and Structural Dynamics* 37 (2008), pp. 21–42.
- [2] A. A. R. Bakhaty. “Theoretical Development of Hybrid Simulation Applied to Plate Structures”. MA thesis. University of California, Berkeley, 2013.
- [3] O. S. Bursi et al. “Rosenbrock-based algorithms and subcycling strategies for real-time nonlinear substructure testing”. In: *Earthquake Engineering and Structural Dynamics* 40 (2011), pp. 1–19.
- [4] S. Change, K. Tsai, and K. Chen. “Improved time integration for psuedodynamic tests”. In: *Earthquake Engineering and Structural Dynamics* 27 (1998), pp. 711–730.
- [5] R. Courant and D. Hilbert. *Methods of Mathematical Physics, Volume 1*. New York: Interscience Publishers, Inc, 1953.
- [6] R. Courant and D. Hilbert. *Methods of Mathematical Physics, Volume 2*. New York: Interscience Publishers, Inc, 1962.
- [7] S. N. Dermitzakis and S. A. Mahin. *Development of substructuring techniques for on-line computer controlled seismic performance testing*. Tech. rep. Berkeley, CA: Earthquake Engineering Research Center, 1985.
- [8] N. E. Dowling. *Mechanical Behavior of Materials*. Upper Saddle River, NJ: Prentice Hall; 3rd Edition, 2007.
- [9] J. D. Ferry. *Viscoelastic Properties of Polymers*. New York: John Wiley & Sons, 1970.
- [10] J. Guyader. *Vibration in Continuous Media*. Great Britain: ISTE Ltd, 2006.
- [11] R. C. Hibbeler. *Statics and Mechanics of Materials*. Upper Saddle River, NJ: Prentice Hall; 2nd Edition, 2004.
- [12] C. Johnson. *Numerical Solution of Partial Differential Equations by the Finite Element Method*. Mineola, NY: Dover Publications, 2009.
- [13] *MATLAB*. Mathworks. 2013. URL: <http://www.mathworks.com>.

- [14] K. M. Mosalam et al. “EAGER: Next Generation Hybrid Simulation: Theory, Evaluation, and Development”. In: *Poster for the NSF Engineering Research and Innovation Conference and Mechanical and Manufacturing Innovation (CMMI) Grantee Conference*. Boston, MA, 2012.
- [15] G. Mosqueda. “Continuous hybrid simulation with geographically distributed substructures”. PhD thesis. University of California, Berkeley, 2003. 232 pp.
- [16] A. H. Schellenberg. “Advanced implementation of hybrid simulation”. PhD thesis. University of California, Berkeley, 2008. 348 pp.
- [17] P. S. B. Shing and S. A. Mahin. *Experimental error propagation in pseudodynamic testing*. Tech. rep. Berkeley, CA: Earthquake Engineering Research Center, 1983.
- [18] P. S. B. Shing and S. A. Mahin. *Pseudodynamic test method for seismic performance evaluation: theory and implementation*. Tech. rep. Berkeley, CA: Earthquake Engineering Research Center, 1984.
- [19] K. Takanashi and M. Nakashima. “Japanese activities on on-line testing”. In: *Journal of Engineering Mechanics* 113 (1987), pp. 1014–1032.
- [20] B. H. Tongue. *Principles of Vibration*. New York: Oxford University Press; 2nd Edition, 2002.
- [21] N. W. Tschoegl. *The Phenomenological Theory of Linear Viscoelastic Behavior*. Berlin: Springer-Verlag, 1989.

# Appendix A

## Analytical Bar Error Equation Derivation

The equations for bar are as follows:

$$\xi(y, \tau) = \frac{F}{\kappa \cos(\kappa)} \sin(\kappa y) \exp(i\Omega\tau), \quad (\text{A.1})$$

$$\hat{\xi}_p(y, \tau) = \frac{G_1}{\sin(\kappa L_1)} \sin(\kappa y) \exp(i\Omega\tau), \quad (\text{A.2})$$

$$\hat{\xi}_c(y, \tau) = \left( G_2 \cos(\kappa(y-1)) + \frac{F}{\kappa} \sin(\kappa(y-L_1)) \right) \frac{\exp(i\Omega\tau)}{\cos(\kappa L_2)}. \quad (\text{A.3})$$

With the following definitions for  $G_1$  and  $G_2$ :

$$G_1 = \frac{F}{\kappa \cos(\kappa L_2) G_d}, \quad (\text{A.4a})$$

$$G_2 = (1 + \epsilon_1) \exp(i\Omega d_1) G_1, \quad (\text{A.4b})$$

$$G_d = (1 + \epsilon_2) \exp(i\Omega d_2) \cot(\kappa L_1) - (1 + \epsilon_1) \exp(i\Omega d_1) \tan(\kappa L_2). \quad (\text{A.4c})$$

In order for the error to be determined (A.1), (A.2), and (A.3) must be applied to the following:

$$\|e_p\|^2 = \int_0^T \int_0^{L_1} \left( \text{Re}(\xi(y, \tau) - \hat{\xi}_p(y, \tau)) \right)^2 dy d\tau, \quad (\text{A.5a})$$

$$\|e_c\|^2 = \int_0^T \int_{L_1}^1 \left( \text{Re}(\xi(y, \tau) - \hat{\xi}_c(y, \tau)) \right)^2 dy d\tau, \quad (\text{A.5b})$$

$$\|e\| = \sqrt{\|e_p\|^2 + \|e_c\|^2}. \quad (\text{A.5c})$$

In order to get an analytical solution for  $\|e_p\|^2$  and  $\|e_c\|^2$ , the real parts of  $\xi$ ,  $\hat{\xi}_p$ , and  $\hat{\xi}_c$  must be found. The most straight forward way to do this is to get the complex part of each equation in the numerator, thus  $G_1$  and  $G_2$  are multiplied by  $G_d^*$ , where  $G_d^*$  is the complex conjugate of  $G_d$ . This gives

$$\begin{aligned} |G_d|^2 = G_d G_d^* = & (1 + \epsilon_2)^2 \cot^2(\kappa L_1) + (1 + \epsilon_1)^2 \tan^2(\kappa L_2) \\ & - 2(1 + \epsilon_2)(1 + \epsilon_1) \cot(\kappa L_1) \tan(\kappa L_2) \cos(\Omega(d_2 - d_1)). \end{aligned} \quad (\text{A.6})$$

Thus,  $G_1$  and  $G_2$  become

$$G_1 = \frac{F \left( (1 + \epsilon_2) \exp(-i\Omega d_2) \cot(\kappa L_1) - (1 + \epsilon_1) \exp(-i\Omega d_1) \tan(\kappa L_2) \right)}{\kappa \cos(\kappa L_2) |G_d|^2}, \quad (\text{A.7})$$

$$G_2 = \frac{F(1 + \epsilon_1) \left( (1 + \epsilon_2) \exp(i\Omega(d_1 - d_2)) \cot(\kappa L_1) - (1 + \epsilon_1) \tan(\kappa L_2) \right)}{\kappa \cos(\kappa L_2) |G_d|^2}. \quad (\text{A.8})$$

Note that

$$\exp(ix) = \cos(x) + i \sin(x), \quad (\text{A.9})$$

where  $x$  is a real value. Also note that

$$\text{Re}(z_1 + z_2) = \text{Re}(z_1) + \text{Re}(z_2), \quad (\text{A.10})$$

where  $z_1$  and  $z_2$  are complex values. Thus, now the real parts of  $\xi$ ,  $\hat{\xi}_p$ , and  $\hat{\xi}_c$  can all be easily found, as shown by

$$\text{Re}(\xi(y, \tau)) = \frac{F}{\kappa \cos(\kappa)} \sin(\kappa y) \cos(\Omega \tau), \quad (\text{A.11})$$

$$\text{Re}(\hat{\xi}_p(y, \tau)) = \frac{F \left( (1 + \epsilon_2) \cos(\Omega(\tau - d_2)) \cot(\kappa L_1) - (1 + \epsilon_1) \cos(\Omega(\tau - d_1)) \tan(\kappa L_2) \right)}{\kappa \sin(\kappa L_1) \cos(\kappa L_2) |G_d|^2} \sin(\kappa y), \quad (\text{A.12})$$

$$\begin{aligned} \text{Re}(\hat{\xi}_c(y, \tau)) = & \left( \frac{F(1 + \epsilon_1) \cos(\kappa(y - 1))}{\kappa \cos^2(\kappa L_2) |G_d|^2} \left( (1 + \epsilon_2) \cos(\Omega(\tau + d_1 - d_2)) \cot(\kappa L_1) \right. \right. \\ & \left. \left. - (1 + \epsilon_1) \cos(\Omega \tau) \tan(\kappa L_2) \right) + \frac{F \cos(\Omega \tau)}{\kappa \cos(\kappa L_2)} \sin(\kappa(y - L_1)) \right). \end{aligned} \quad (\text{A.13})$$

Now, these equations can be applied to (A.5a) and (A.5b). Both the time and space integrals are straight forward, requiring only patience. Thus, the following equations are derived:

$$\begin{aligned} \|e_p\| = & \frac{\pi}{\Omega} F^2 \left( \frac{L_1}{2} - \frac{\sin(2\kappa L_1)}{4\kappa} \right) \left( \frac{1}{(\kappa \cos(\kappa))^2} + \frac{1}{(\kappa \cos(\kappa L_2) \sin(\kappa L_1))^2 |G_d|^2} \right. \\ & \left. + \frac{2(1 + \epsilon_1) \tan(\kappa L_2) \cos(\Omega d_1) - 2(1 + \epsilon_2) \cot(\kappa L_1) \cos(\Omega d_2)}{(\kappa)^2 \cos(\kappa) \sin(\kappa L_1) \cos(\kappa L_2)} \right). \end{aligned} \quad (\text{A.14})$$

$$\begin{aligned}
\|e_c\| = & \frac{\pi}{\Omega} \left( M \left( \frac{L_2}{2} + \frac{\sin(2\kappa L_2) - \sin(2\kappa)}{4\kappa} \right) + N \left( \frac{L_2}{2} - \frac{\sin(2\kappa L_2)}{4\kappa} \right) \right. \\
& + Q \left( \frac{L_2}{2} - \frac{\sin(2\kappa L_2)}{4\kappa} \right) - 2P \left( \frac{\cos(\kappa(L_1 - L_2)) - \cos(\kappa) + 2L_2\kappa \sin(\kappa)}{4\kappa} \right) \\
& \left. + 2R \left( \frac{L_2 \sin(\kappa L_2)}{2} \right) - 2S \left( \frac{2L_2\kappa \cos(\kappa L_1) + \sin(\kappa L_1) - \sin(\kappa(1 + L_2))}{4\kappa} \right) \right). \tag{A.15}
\end{aligned}$$

Where  $M$ ,  $N$ ,  $P$ ,  $Q$ ,  $R$ , and  $S$  are defined by

$$M = \frac{F^2}{\kappa^2 \cos^2(\kappa)} \tag{A.16a}$$

$$N = \frac{F^2}{\kappa^2 \cos^2(\kappa L_2)} \tag{A.16b}$$

$$P = \frac{F^2(1 + \epsilon_1) \left( (1 + \epsilon_2) \cot(\kappa L_1) \cos(\Omega(d_2 - d_1)) - (1 + \epsilon_1) \tan(\kappa L_2) \right)}{\kappa^2 \cos^2(\kappa L_2) \cos(\kappa) |G_d|^2} \tag{A.16c}$$

$$Q = \frac{F^2(1 + \epsilon_1)^2}{(\kappa \cos^2(\kappa L_2))^2 |G_d|^2} \tag{A.16d}$$

$$R = \frac{F^2(1 + \epsilon_1) \left( (1 + \epsilon_2) \cot(\kappa L_1) \cos(\Omega(d_2 - d_1)) - (1 + \epsilon_1) \tan(\kappa L_2) \right)}{\kappa^2 \cos^3(\kappa L_2) |G_d|^2} \tag{A.16e}$$

$$S = \frac{F^2}{\kappa^2 \cos(\kappa) \cos(\kappa L_2)} \tag{A.16f}$$

Now that  $\|e_p\|$  and  $\|e_c\|$  have been defined, (A.5c) can be used to get the error for the hybrid elastic fixed-free bar.

## Appendix B

# Analytical Solutions vs. Computational Solutions

In Appendix A, an analytical solution was derived for the error to the elastic fixed-free bar. However, for the other three cases, the equations are too complicated to derive an analytical solution in a reasonable amount of time. This leads to the use of the MATLAB<sup>®</sup> function *quadgk*, which uses adaptive Gauss-Kronrod quadrature to evaluate the integrals for the error [13]. The problem with using a numerical method for evaluating an integral is determining whether or not the numerical solution is accurate. In order to fully justify the use of *quadgk*, the solution from the analytical equations of Appendix A are directly compared against those coming from *quadgk*. Figs. B.1-B.3 show both the analytical and numerical solution for the elastic fixed-free bar with three different sets of error parameters. As it can be seen in all three cases, the two curves are directly on top on each other, which indicates that the solutions are the same. However, to be thorough, the absolute value of the difference is also examined. Figs. B.4-B.6 shows the absolute value of the difference between the analytical and numerical solutions from Figs. B.1-B.3. As it can be seen, in all three cases, the absolute value of the difference is less than machine precision, except at the resonant frequencies. This rise in error at the resonant frequencies comes from the unboundedness of the displacement at those frequencies. This is not a cause of concern since the resonant frequencies are locations in the frequency domain that need to be avoided for a proper hybrid system simulation. Also, note that there is a trend of increasing error with increasing frequency. Again, this is not a cause for concern because in all cases, the frequency,  $\Omega$ , never goes above  $10^2$ , which is still within the domain of acceptable difference between the two solutions. Since the other three cases only involve the integration of squared trigonometric functions, it can be concluded that the results from the use of *quadgk* will nearly be identical to those obtained from an analytical solution, thus allowing for a correct analysis of the system.

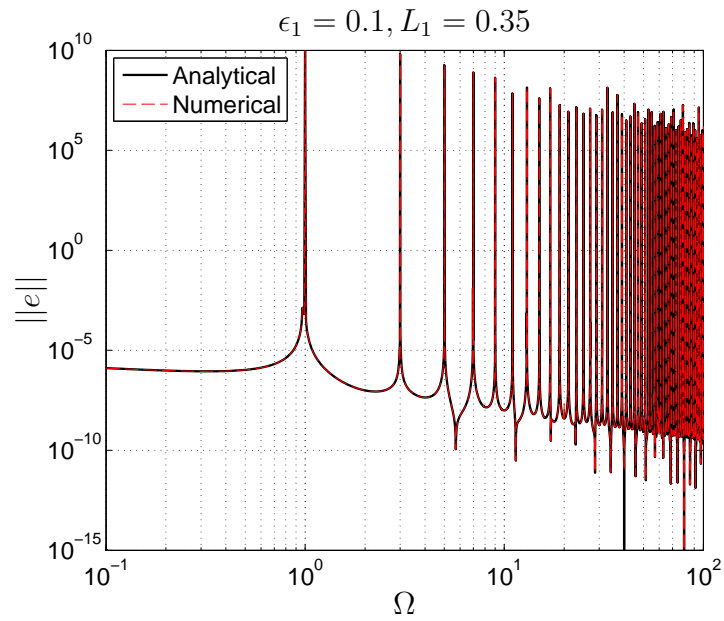


Figure B.1: A comparison of the analytical and numerical solutions to the elastic fixed-free bar with  $\epsilon_1 = 0.1$  on a log-log plot.

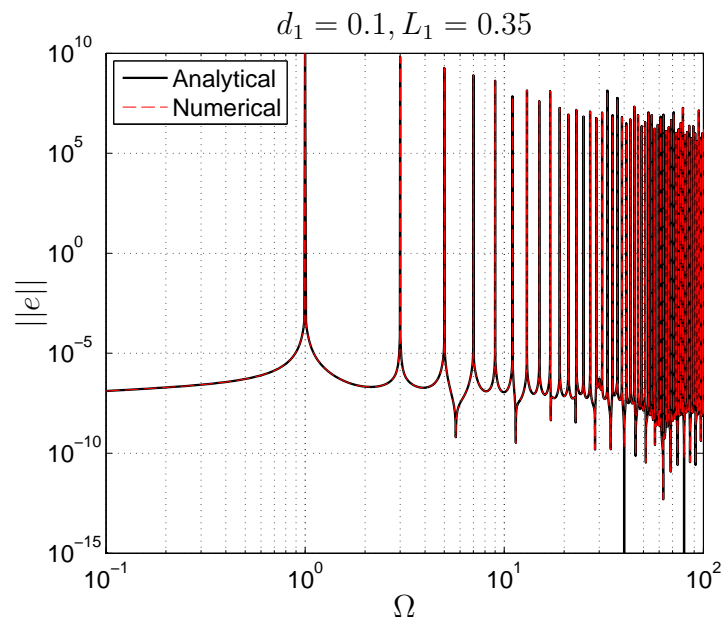


Figure B.2: A comparison of the analytical and numerical solutions to the elastic fixed-free bar with  $d_1 = 0.1$  on a log-log plot.

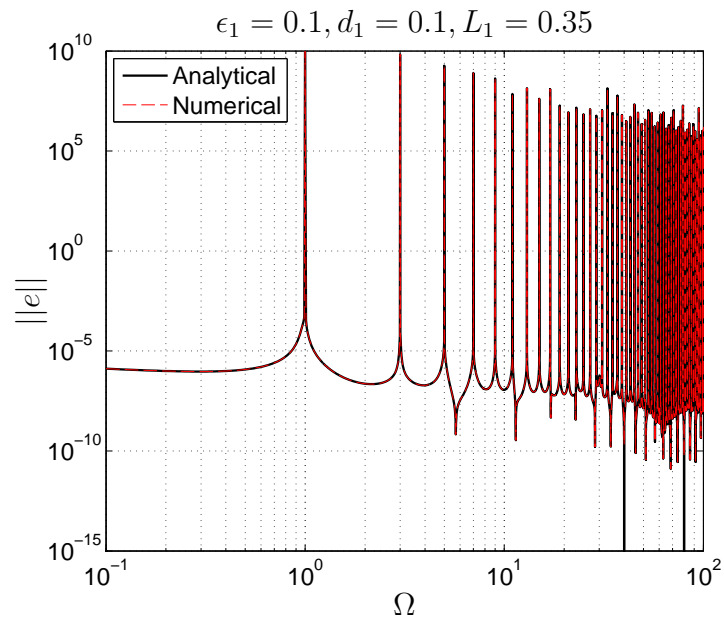


Figure B.3: A comparison of the analytical and numerical solutions to the elastic fixed-free bar with  $\epsilon_1 = 0.1$  and  $d_1 = 0.1$  on a log-log plot.

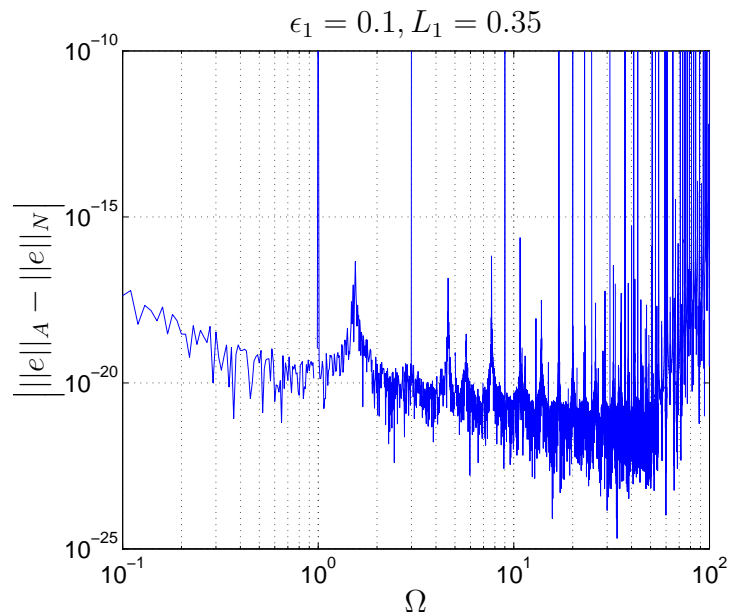


Figure B.4: The absolute value of the difference between the analytical and numerical solutions to the elastic fixed-free bar with  $\epsilon_1 = 0.1$  on a log-log plot.

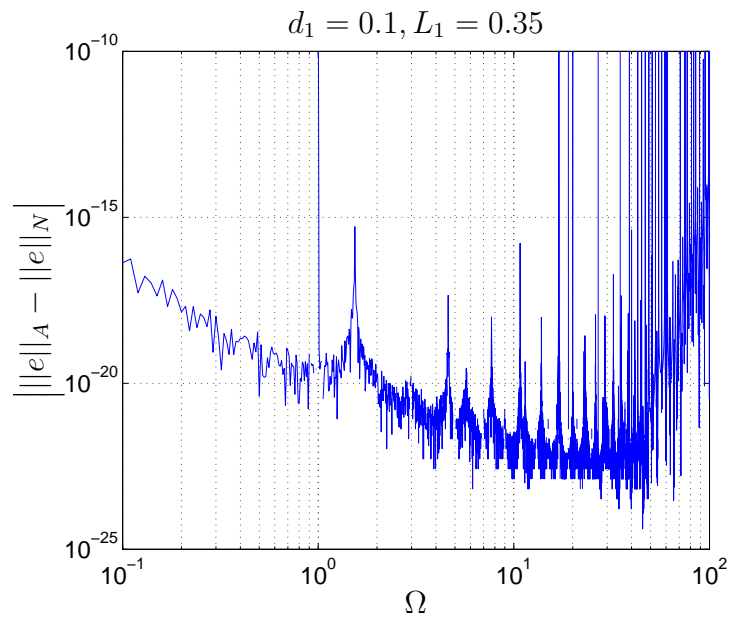


Figure B.5: The absolute value of the difference between the analytical and numerical solutions to the elastic fixed-free bar with  $d_1 = 0.1$  on a log-log plot.

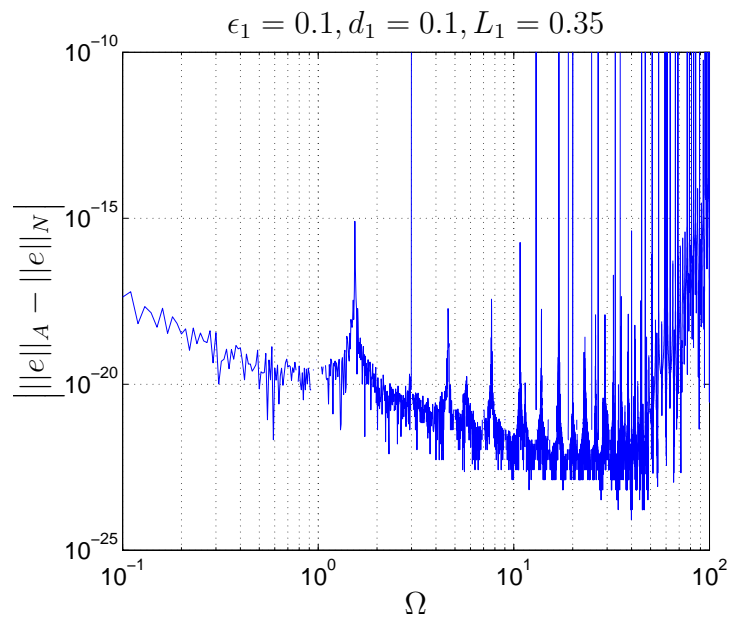


Figure B.6: The absolute value of the difference between the analytical and numerical solutions to the elastic fixed-free bar with  $\epsilon_1 = 0.1$  and  $d_1 = 0.1$  on a log-log plot.

# Appendix C

## Material Constants

### C.1 Fixed-Free Bar

For analysis of the fixed-free bar in Chapter 4, the bar is assumed to be a square steel bar with material constants and dimensions listed in Table C.1 [8].

### C.2 Pinned-Pinned Beam

For analysis of the pinned-pinned beam in Chapter 4, the beam is assumed to be a square steel beam with material constants and dimensions listed in Table C.2 [8].

$E$	$E_0$	$E_\infty$	$A$	$l$	$\rho$	$\bar{f}$
$2 \times 10^{11} \frac{\text{N}}{\text{m}^2}$	$2 \times 10^{11} \frac{\text{N}}{\text{m}^2}$	$10^{11} \frac{\text{N}}{\text{m}^2}$	$0.0625 \text{ m}^2$	1 m	$7800 \times A \frac{\text{kg}}{\text{m}}$	$10^5 \text{ N}$

Table C.1: Material constants and dimensions used for fixed-free bar systems

$E$	$E_0$	$E_\infty$	$A$	$I$	$l$	$\rho$	$\bar{M}$
$2 \times 10^{11} \frac{\text{N}}{\text{m}^2}$	$2 \times 10^{11} \frac{\text{N}}{\text{m}^2}$	$10^{11} \frac{\text{N}}{\text{m}^2}$	$0.04 \text{ m}^2$	$\frac{A^2}{12} \text{ m}^4$	10 m	$7800 \times A \frac{\text{kg}}{\text{m}}$	$10^4 \frac{\text{N}}{\text{m}^2}$

Table C.2: Material constants and dimensions used for fixed-free bar systems